Characterization of the ALPIDE Detector with Proton Beams for the Development of a Prototype Proton Computed Tomography Machine at the University of Bergen

Master Thesis in Nuclear Physics
by
Viljar Nilsen Eikeland

Department of Physics and Technology
University of Bergen
Norway

June 01, 2018

Abstract

In conventional radio therapy, photons is used in the treatment. Treatment with protons, however, greatly reduce the energy which is deposited in healthy tissue surrounding the tumor. The aim for the pCT group at the University in Bergen is to develop an imaging modality using protons. The motivation for this is to accurately locate the Bragg-peak, which is the region where the protons deposit the maximum of their energy. At the moment conventional CT scans are used to map the inner structures of a patient. The relation between photon attenuation and stopping power is not one-to-one. Thus this leads to uncertainties in the location of the Bragg-peak for protons. The design proposed by the pCT group at UIB is one that aims to have one detector to both track the particles and measure the energy deposition of the traversing protons. The detector which was chosen for this purpose, was the ALPIDE detector developed for the ITS upgrade at CERN. It has a high granularity and is thus able to track the protons efficiently.

This thesis will look into how the ALPIDE detector efficiently measures the energy deposition of non MIP. It focuses on how the signal from the traversing particles behaves under variation of different parameters, before looking into the behavior of the ALPIDE when exposed to a high LET proton beam. Previous characterizations of the ALPIDE have focused on MIP, while this is some of the earlier work with heavier particles.

The ALPIDE was able to distinguish the energy deposited with varying LET, especially in the region where the LET is constant among the particles traversing the ALPIDE, the cluster size of individual particles can be a good indication on energy deposited. It has thus shown promising signs that it will be able to perform well in the proposed setup of the prototype pCT designed by the pCT group at the University of Bergen.

Acknowledgments

Contents

List of Figures

Chapter 1

Introduction

The most common way of radiation therapy is utilizing photon beams. This has its drawbacks as photons deliver dose to surrounding healthy tissue. In recent years, the focus has been shifted to treatment with charged particles. This is a method which benefits the patient, due to confinement in the delivery of dose to malignant tissue. This way it is safer for the patient to get treatment to tumors which is in the close vicinity of organs at risk, such as the heart, rectum etc. It also reduces the dose delivered to surrounding tissue, which in turn reduces the risk of radiation induced cancer. This is critical in radiation treatment of children. In Norway, this form of treatment got the spotlight in 2013, when the government funded a new report targeting the possibility for radiation therapy centers with charged particles [1]. In the autumn of 2017 it was decided that two of these centers are to be built in Norway, one in Oslo and one in Bergen. These are expected to be up and running by 2023 and 2025 respectively [2].

The current technique for imaging of the patient, prior to treatment, uses X-ray photons. The planning of dose delivery also uses this technique, and this introduces uncertainties which can be reduced by a proton computed tomography machine. The University of Bergen has been granted funding for the development of a prototype proton computed tomography scanner.

1.1 About the thesis

The main goal of this thesis is to characterize the ALPIDE detector which will be used in the prototype pCT being developed at the University of Bergen. The pCT will have a multitude of ALPIDEs stacked in several layers, with multiple ALPIDEs per layer. The ALPIDE will be responsible for both tracking and energy loss of the individual particles. The ALPIDE is a particle detector chip developed for the ALICE experiment and mainly for detecting minimum ionizing particles. If the ALPIDE is to be used in a pCT, its tracking capability and measurement of energy loss of the traversing particles must also work for heavy charged particles. This thesis will mainly focus on how the ALPIDE behaves when exposed to these kind of particles.

This work builds on the work previously done by the pCT group at the University of Bergen, and the work done by the ITS upgrade team at CERN. Time was spent at collecting data during a beam test in Oslo, as well as general testing of the ALPIDE at the University of Bergen. Both the general behavior of the ALPIDE by changing its parameters and exposing the ALPIDE to radioactive sources were done in Bergen. The tests

were done by the software provided by the ALICE ITS upgrade team. There were little documentation of the software provided, so time was spent at studying the code and to get a general understanding of the individual test softwares. By doing these tests, a understanding of how the chip behaves under certain conditions was achieved.

A significant effort was put into software development for analysis, as this was not developed at the time. The software for analysis was written in c++ and the ROOT analysis tool was used for analysis. Some time was used in GATE to simulate the beam parameters during the beam test in Oslo.

1.2   Thesis outline

Chapter 2: Radiation therapy and Proton CT aims to give an introduction into the theory of particle interactions and how this is applicable to radiation therapy and proton CT.

Chapter 3: Semiconductors and Silicon Pixel Detectors explains the physics behind semiconductors and how this technique can be applied in detectors used in the prototype proton CT.

Chapter 4: ALPIDE Chip gives a short summary of how the detector is to be used in the ITS upgrade at ALICE. An overview of how to operate and manipulate the ALPIDE chip in order to use it in a proton CT is given.

Chapter 5: Characterization of the ALPIDE reviews how the ALPIDE produces hit information which can be used in tracking and energy deposition of the traversing particle. Two necessities for the proton CT.

Chapter 6: OCL - Oslo Cyclotron Lab reviews the performance of the ALPIDE as a telescope in the new design of the proton CT.

Discussion and Conclusion summarizes the work of the thesis, and discusses further development of the prototype proton CT.

1.3   Citation principles

Citations are listed after a paragraph. They may refer to multiple statements in that paragraph and they always refer to the previous section.

Chapter 2

Radiation Therapy and Proton CT

Radiation may be characterized in various ways, direct or indirect ionization, or non-ionizing radiation, depending on the particle in question. For charged particles such as αs, βs and heavier nuclei such as C^{12}, the interaction is direct since the particles can interfere directly with the atoms in the medium it is traversing. It is ionizing in the way it kicks out electrons from the medium it is traversing by transferring energy to the medium. Other forms of ionizing radiation include particles such as the photon and neutrons. These have an indirect effect, where they transfer energy to the electrons or to the nucleus. This creates by-products that can interact with the atoms [3].

2.1 Interaction of charged particles with matter

When a charged particle traverses a medium, it will lose energy by interacting with the medium it is penetrating. The energy loss of the particle is governed by different types of interactions:

- Inelastic scattering with valence electrons

- Elastic collision with the atomic shell

- Elastic collision with nuclei

- Inelastic collision with nuclei

- Bremsstrahlung radiation

- Cerenkov radiation

- Transition radiation

The main interaction of these particles is by inelastic collisions with the valance electrons in the medium. The particles may also interact with the medium by elastic collisions, both with the electrons and with the nucleus. There are also other interactions such as energy loss by Bremsstrahlung radiation, Cerenkov radiation and Transition radiation, but these are minimal compared to the inelastic scattering of valence electrons [4].

2.1.1 Energy loss by ionization for heavy particles

When a charged particle goes through a medium, it will interact with every Coulomb field present in the medium along its trajectory, and thus lose energy in the process. This

energy loss is governed by the Bethe-Bloch formula. This states that the average energy loss of a heavy charged particle per unit length, also known as stopping power, is given by the following formula [4]:

$$-\frac{dE}{dx} = K\rho\frac{Z}{A}\frac{z^2}{\beta^2}[ln(\frac{2m_ec^2\beta^2\gamma^2W_{max}}{I^2}) - 2\beta^2 - \delta - 2\frac{C}{Z}] \qquad (2.1)$$

where

$$K = 2\pi N_A r_e{}^2 m_e c^2 \approx 0.307 MeV\,mol^{-1}cm^2$$

Table 2.1.1: Parameters involved in the Bethe-Bloch formula	
N_A	Avogadro's number = 6.022 x $10^{23}mol^{-1}$
r_e	Classical electron radius = 2.818 x $10^{-15}m$
m_e	Electron rest mass = $0.511MeV/c^2$
c	Speed of light in vacuum = $299792458m/s$
z	Charge of incident particle in units of e
ρ	Density of absorber material
Z	Atomic number of absorber
A	Atomic weight of absorber in units of g/m
β	$\bar{v}/c$ of the incident particle
γ	Lorentz factor $1/\sqrt{1-\beta^2}$
W_{max}	Maximum energy transfer in a single collision
I	Mean excitation potential eV
δ	Density correction
C	Shell correction

From this formula it can be observed that the energy loss is mainly dependent on two different things. The charge of the incident particle z^2, which states that a particle carrying a higher charge is more effective at ionizing the medium. And the velocity of the incident particle.
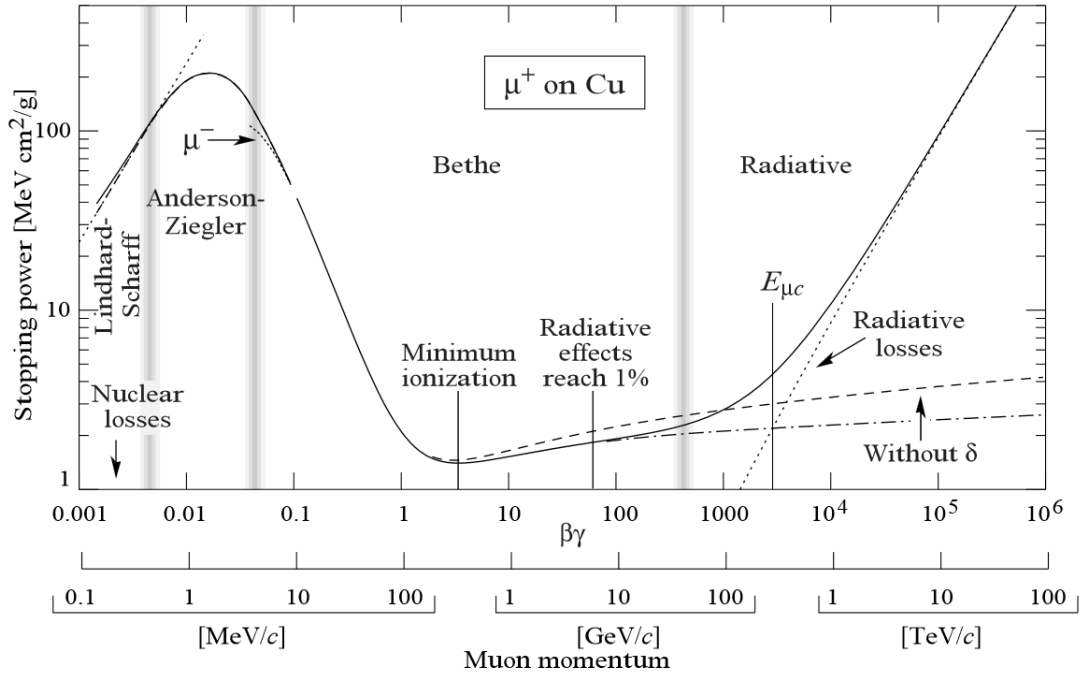
Figure 2.1: Bethe-Bloch [5].

4

As can be seen from Fig 2.1, the energy loss by ionization and excitation can be sorted into three different regions. In the third region the energy loss increases due to relativistic effects before it saturates due to the density effects of the medium it is traversing. As the velocity decreases, the particle enters the region where it becomes a MIP. This is when the velocity of the particle is 0.97c [4]. As the velocity decreases, the particle enters the first region where the energy loss, to first order, is governed by $1/\beta^2$. As the particle's velocity drops, the exposure time the particle has to interact with its surrounding Coulomb fields increases. This leads to a high energy loss. This property is very useful as it states that the particle will lose a lot of energy in a confined area which leads to the Bragg peak. This will be explained in detail later [4].

2.1.2 Energy loss of electrons and positrons

When the electron or positron traverses a medium, it feels the strength of the electric field of the nuclei. Because of their light weight they will be bent around the nuclei with a curvature which is dependent on the strength of the electric field of the nuclei[4]. Based on the curvature of the trajectory, the electrons and positrons will radiate energy by releasing photons. This is known as Bremsstrahlung radiation. Electrons and positrons may also ionize the medium when they pass through it. Thus the energy loss of lightly charged particles differ from heavy charged particles, and the difference can be summarized [6]:

- Relativistic effects become important at relatively low kinetic energies.

- Collisions with orbital electrons may result in a large energy transfer. Up to 50 % for electrons, and 100 % for positrons.

- Collisions with nuclei may result in bremsstrahlung production, and depending on the lightly charged particle's incident energy, this may exceed collision loss.

Because of the low mass of the particles and the fact that, for electrons the collision is between identical particles, and they are thus indistinguishable, this leads to an alteration of the Bethe-Bloch formula [4].

$$-\frac{dE}{dX} = 2\pi N_a r^2{}_e m_e c^2 \rho \frac{Z}{A} \frac{1}{\beta^2} [ln(\frac{\tau^2(\tau+2)}{2(I/m_e c^2)^2}) + F(\tau) - \delta - 2\frac{C}{Z}] \qquad (2.2)$$

where τ is the kinetic energy of the particle in units of $m_e c^2$,

$$F(\tau) = 1 - \beta^2 + \frac{\frac{\tau^2}{8} - (2r+1)ln2}{(\tau+1)^2}$$

for e^-

$$F(\tau) = 2ln2 - \frac{\beta^2}{12}(23 + \frac{14}{\tau+2} + \frac{10}{(\tau+2)^2} + \frac{4}{(\tau+2)^3})$$

for e^+

The rest of the factors are explained previously in table 2.1.1.
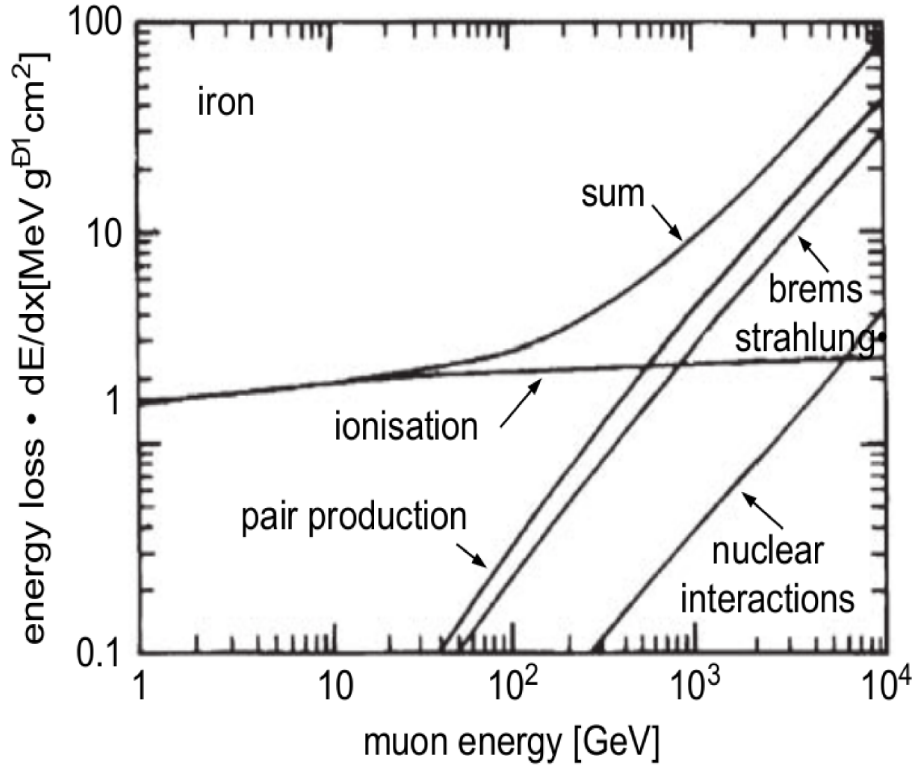
Figure 2.2: Energy loss from ionization and Bremsstrahlung. Critical energy is the energy in which the contribution from energy loss by ionization and energy loss from Bremsstrahlung are equal [7].

Since we have the added effect of Bremsstrahlung at a few MeVs, the total energy loss for electrons and positrons is then composed of two factors [4]:

$$(\frac{dE}{dX})_{tot} = (\frac{dE}{dX})_{coll} + (\frac{dE}{dX})_{rad} \tag{2.3}$$

2.1.3 Range

The range of a particle can be defined as the length it traverses before it stops. Given that the beam has mono-energetic particles, not all of the particles will have the same range in a material. Heavy charged particles may undergo several types of interactions. These interactions are statistical in nature, which means that the accumulative effect of these interactions are that the individual particles will have a different path length, which will fluctuate with a few percent depending on the absorber material. This variation is known as *straggeling*. This variation will follow a Gaussian distribution to first approximation, and the straggling parameters are dependent on [8]:

- the atomic number of the absorber

- the ionization energy of the absorber

- the charge of the incident particle

- the velocity of the incident particle

On a general note, the range of a particle can be estimated by integrating over the stopping power:

$$R = \int_0^R dx = \int_0^E (-\frac{dE}{dx}^{-1})dE \qquad (2.4)$$

The energy loss of charged particles is a complicated function of the energy, thus approximations of eq. 2.4 is on a general basis used. Since the stopping power to first order varies with $1/\beta^2$ and β^2 with E, one would expect according to eq.2.4 that the range follows E^2. For most cases this exponent is smaller than 2, so $R \propto aE^{1.75}$, where a is a constant. This will vary slightly with the energy and absorber material. A semi-empirical approximation of a simplified expression of the Bethe-Bloch equation is at times used [9]:

$$R \approx \frac{\pi\epsilon_0{}^2 m_e E^2}{n_A Z_A Z^2 e^4 M} \qquad (2.5)$$

- ϵ_0 is the permeability of free space.
- $n_A Z_A$ represents the average density.
- M is the mass of the incident particle.

The range of protons in water as a function of energy can be seen in Fig 2.3.
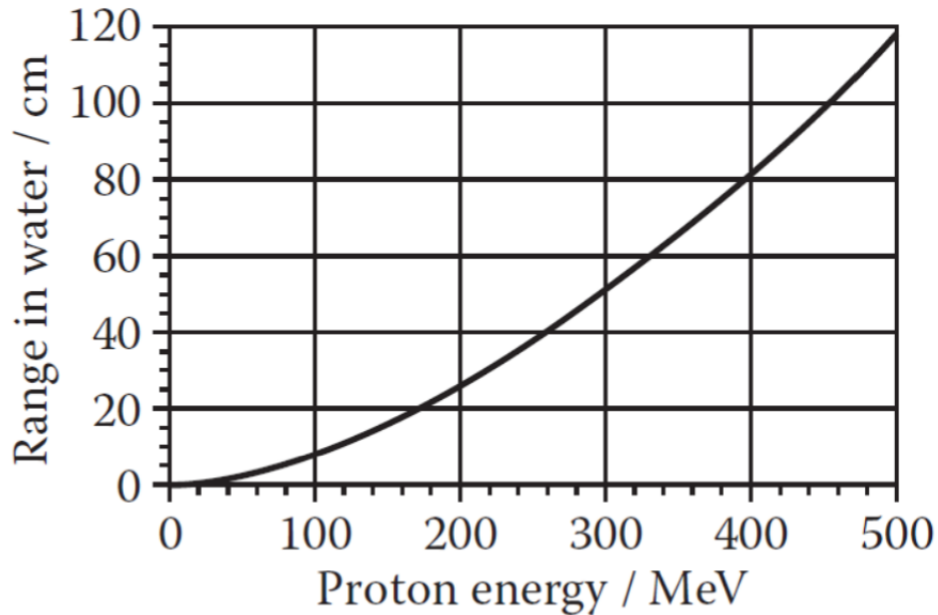
Figure 2.3: Proton range vs energy in water [10].

2.1.4 Multiple Coulomb scattering

When a charged particle is traversing a medium, it is subjected to a lot of small-angle scatters of atomic nuclei. This is referred to as multiple Coulomb scattering. Each of the individual collisions is governed by the Rutherford formula [4];

$$\frac{d\sigma}{d\Omega} = z^2{}_2 z^2{}_1 r^2{}_e \frac{mc/\beta p}{4sin^4(\theta/2)} \tag{2.6}$$

Most of these result in a small angular deflection because of the $1/sin^4(\theta/2)$ dependence. With the assumption that the target nuclei is a lot heavier than the incident particle, one can assume that the energy transfer is small. Thus the incident particle will have a random zigzag path through the medium. The sum of all these small deflection leads to a deflection from the original path of the incident particle.

At large angles the angular distribution acts like Rutherford scattering, while for smaller deflection angles it has a Gaussian shape [11].

2.1.5 Bragg peak

When a charged particle is traversing a medium, it will deposit small fractions of its energy to the medium. This energy deposition is mainly governed by Coulomb interactions with the valence electrons in the medium. As the particle deposits energy, it also decreases its velocity. As the velocity decreases, the number of interactions per unit track length increases. This leads to a maximum energy deposition at a certain depth of the medium it is traversing. The region where this maximum energy deposition occurs is known as the Bragg-peak. This region will be located around the same area as the particle range in the medium. The energy-deposition is dependent on the velocity of the particle, which can be observed in Fig 2.1. After the Bragg-peak, the energy deposition falls quickly. Depending on, whether there is one particle in question or a beam of particles with a monochromatic energy, the shape of the Bragg curve changes. For a single particle the Bragg curve will have a very sharp peak, before it falls down to zero. For a beam however, the Bragg curve is made up of all the energy deposition for the different particles in the beam. Since the interaction of the particles is statistical, this will affect the range of the particles in the beam. Depending on the velocity of each individual particle, it will have an individual energy deposition at the end of its path. This leads to the peak being smeared out compared to the peak of a individual particle. For particles heavier than the proton, such as C^{12}, nuclear fragmentations also have to be accounted for. This will in general lead to a tail of the curve after the peak [12].
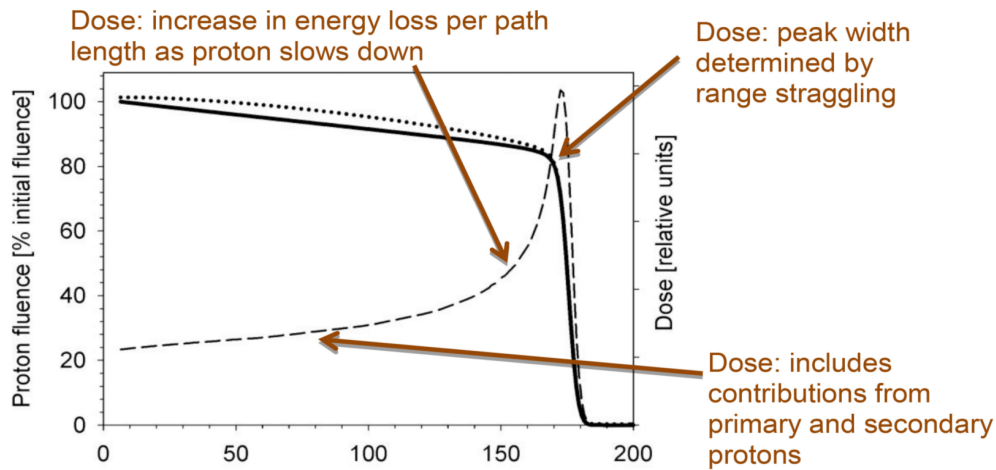
Figure 2.4: Dashed line and right axis: Bragg curve for a 160 MeV proton beam. Left axis: total (dotted line) and primary (solid line) proton fluence as a function of depth [10].

Spread-Out Bragg Peak (SOBP)

In particle therapy, the spread-out Bragg peak is an important feature in the deliverance of the treatment to the area of the tumor. By adjusting the energy and intensity of the beam being delivered, the range and maximum dose of the beam are altered. If the total dose deposition is calculated, this will lead to an effect where the dose is smeared out over a larger area. This adjustment of the beam can be done in different ways. If the beam is delivered by a synchrotron, then the energy may be adjusted during treatment. The other alternative is to have a cyclotron. The cyclotron is only capable of delivering one energy at the time. Thus different tools have been developed. These tools include the range modulator wheel and a Ridge filter etc. [13].
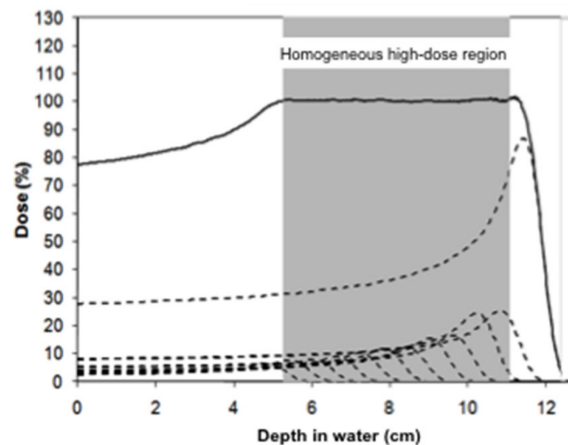
Figure 2.5: Spread-out Bragg peak as a combination of multiple Bragg curves as a function of depth [10].

2.2 Interaction of photons with matter

Photons interact with matter in a different way than charged particles. Since photons do not carry any charge, they have a smaller cross section for interaction with the medium they are traversing, compared to heavy charged particles. However this is dependent on the energy of the different beams and what particle the photon is compared to. This means that an incoming photon beam with an energy E will exit a medium with approximately the same energy as it entered with. However, the intensity of the incoming photon beam will be reduced. The reason for this is that a photon is more likely to vanish if it interacts with the medium. The photon can lose energy by scattering in the medium, this will lower the energy of the photon, which on a general level means that the cross section for interaction increases. Thus the photon is likely to be absorbed by the medium and vanish. The reduction of intensity is given by:

$$I(x) = I_0 e^{-\mu x} \tag{2.7}$$

where I_0 is the intensity of the photon beam as it enters the medium, x is the distance traveled in the medium and μ is the absorption coefficient of the medium, which is dependent on the cross sections of the photon interactions and the density of the medium. The total cross section for a photon interaction is:

$$\sigma_{tot} \approx \sigma_{pe} + \sigma_{comp} + \sigma_{pp} \tag{2.8}$$

where $\sigma_{pe}, \sigma_{comp}$ and σ_{pp} are the cross sections of the photoelectric effect, Compton scattering and pair production respectively. These cross sections will be elaborated on in their respective sections.
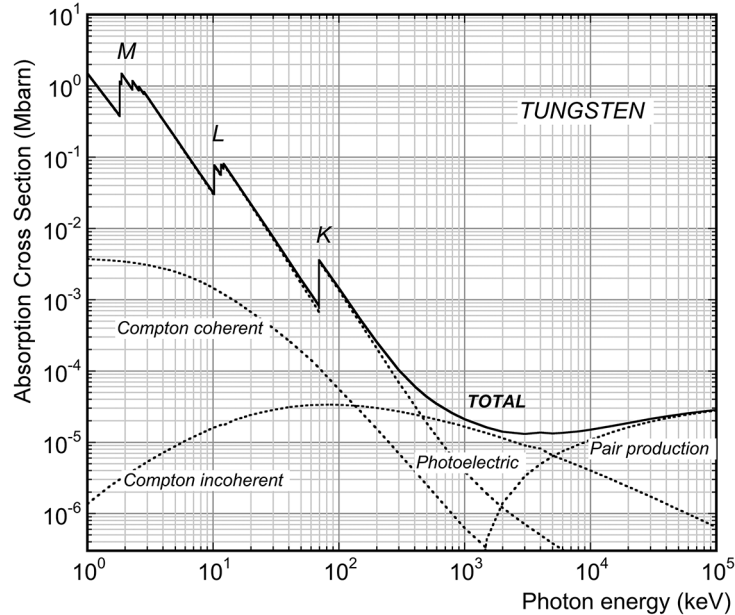
Figure 2.6: Total cross section for photon interactions [14]

The photon may also undergo different processes such as Rayleigh scattering and photonuclear interactions, but these interactions will not be discussed in detail in this thesis. The relation between the absorption coefficient and cross section of the photoelectric effect is:

$$\mu = \frac{(N_A \rho)}{A} \tag{2.9}$$

10

Hence, the absorption coefficient is energy dependent.

The three main interaction methods for the photon, photoelectric effect, Compton scattering and pair production, will be discussed in the following sections [4].

2.2.1 Photoelectric effect

The photoelectric effect is when a photon is absorbed by one of the valance electrons of an atom. This process can occur if the incoming photon has a higher energy E_γ than the binding energy B of the electron. This will free the electron from its bound state and create a photo electron with the kinetic energy [6]:

$$E_{kin} = E_\gamma - B \qquad (2.10)$$

The cross section for the photoelectric effect is dependent on which shell the valance electron is in. Thus a photon energy which resonates with these will have a higher cross section, as can be seen in Fig 2.7. The cross section for the photoelectric effect is approximately;

$$\sigma_{pe} \approx \frac{Z^n}{E^{7/2}} \qquad (2.11)$$

where n varies between 4 and 5. One can observe that the cross section increases with the Z value of the absorber and decreases with increasing photon energy. This can be observed in Fig 2.7. At higher energies the photon energy becomes the dominant part of the equation and the cross section goes to zero [4] [6].
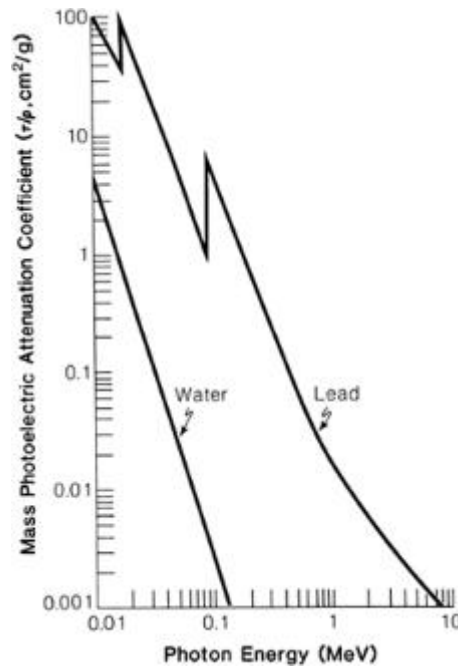
Figure 2.7: Cross section for photoelectric effect[3]

2.2.2   Compton scattering

Compton scattering occurs when an incoming photon, with an energy E_γ, scatters inelastically of electrons (see Fig 2.8). During this collision the photon will transfer some of its energy to the electron. The electrons are considered to be free, since their binding energy is negligible compared to the energy transfer. This energy transfer is given by:

$$E'_\gamma = hv' = \frac{hv}{1 + \epsilon(1 - cos(\theta))} \tag{2.12}$$

where θ is the scattering angle of the photon and $\epsilon = \frac{hv}{m_e c^2}$. After the first collision the photon may undergo several collisions afterwards until it eventually is absorbed by the medium. While the electron, which was struck, now is considered to be free, since the transfered kinetic energy exceeded its binding energy. The electron may then roam around and cause further excitation and ionization of the medium along its pathway.
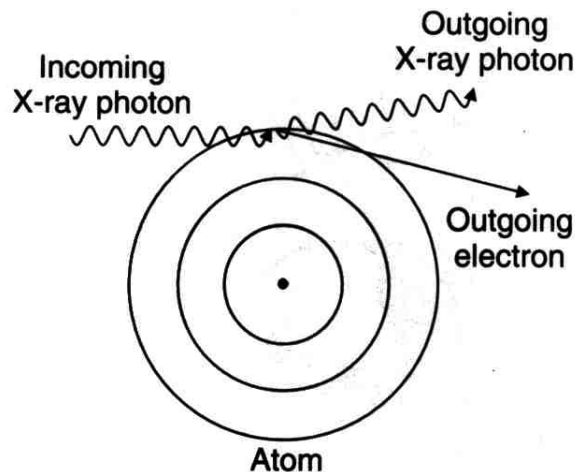
Figure 2.8: Compton scattering

If the incoming photon has a direct hit on the electron, it will have a scattering angle $\theta = 180^o$. At this angle, the photon will transfer the maximum amount of energy, which will be:

$$E'_{\gamma,max} = hv \frac{\epsilon}{1 + 2\epsilon} \tag{2.13}$$

While the electron will have a trajectory going in the forward direction at $\phi = 0^o$. This is the point where the Compton edge occurs.
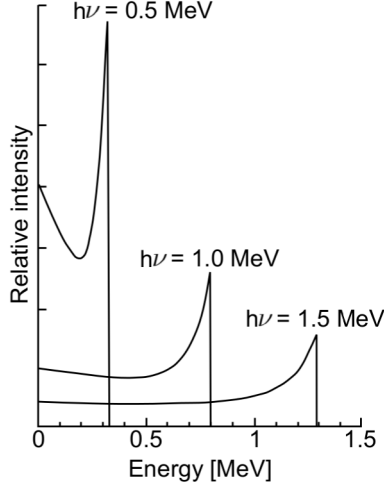
Figure 2.9: Energy distribution of Compton recoil electrons. The sharp drop at the maximum recoil energy is known as the Compton edge [4].

The cross section for Compton scattering is given by the Klein-Nishina formula:

$$\sigma_{comp} = 2\pi r_e{}^2 \left(\frac{1+\gamma}{\gamma^2} \left[\frac{2(1+\gamma)}{1+2\gamma} - \frac{1}{\gamma} ln(1+2\gamma) \right] + \frac{1}{2\gamma} ln(1+2\gamma) - \frac{1+3\gamma}{(1+2\gamma)^2} \right) \qquad (2.14)$$

Clearly, the cross section for Compton scattering bears little dependence on the Z of the absorber material, but it is heavily reliant on the electron density in the medium [4] [6].

2.2.3 Pair production

Pair production is when a photon undergoes a transformation into an electron and a positron. The criteria for this event to occur, is that the photon must travel in the close vicinity of a nucleus, as well as it must have a certain energy, to be able to create a positron and an electron. Given the rest mass of the electron and positron, the energy of the incoming photon must then be:

$$E_\gamma > 1.022 MeV \qquad (2.15)$$

Depending on whether the nucleus is screened or not and the energy of the incident photon, the cross section for pair production differs.

for $1 << \epsilon << \frac{1}{\alpha Z^{1/3}}$ and no screening

$$\sigma_{pp} = 4Z^2 \alpha r_e{}^2 \left[\frac{7}{9} ln(2\epsilon) - \frac{109}{54} \right] \qquad (2.16)$$

for $\epsilon >> \frac{1}{\alpha Z^{1/3}}$ and complete screening

$$\sigma_{pp} = 4Z^2 \alpha r_e{}^2 \left[\frac{7}{9} ln\left[\frac{183}{Z^{1/3}} \right] - \frac{1}{54} \right] \qquad (2.17)$$

where

α is the fine structure constant ($\alpha = 1/137$)

r_e is the classical electron radius

13

Z is the atomic number of the absorber.

Clearly the cross sections for photoelectric effect and pair production are dependent on Z, while the cross section for Compton scattering is not [4] [6] [7].
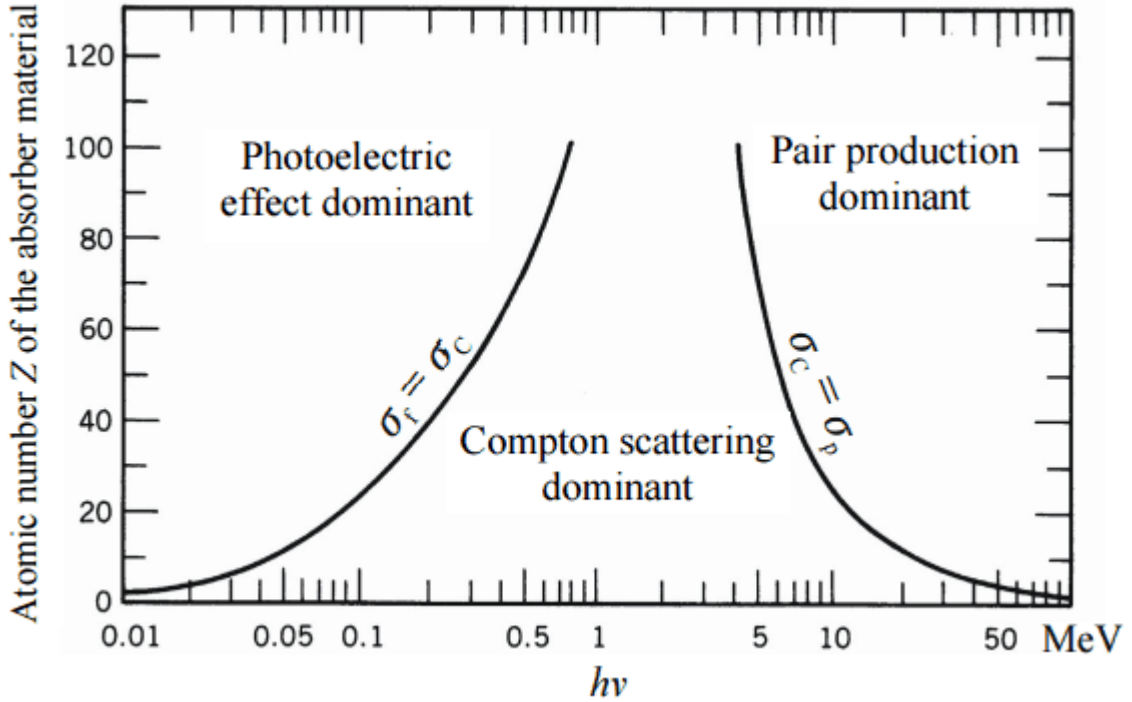
Figure 2.10: Cross section dependence on Z for the absorbing material

2.3 Biological effects

The aim of radiation therapy is to destroy malignant tumors by disabling the ability for the cells to reproduce. This is done by delivering a dose to the area where the tumor is present, while avoiding radiation damage to healthy tissue. Thus there is a compromise that must be made. The biological effect that is delivered during treatment is dependent on multiple factors, including the uniformity of radiation to the organ, the type of radiation and the rate of energy deposition. To destroy the ability of the cell to reproduce, the DNA needs to be damaged sufficiently. This is done by delivering a high enough energy to the tumor. The damage inflicted on the tumor depends on the density of the ionization or the rate of energy loss along the tracks, depending on which form of radiation is delivered to the tumor. This quantity is known as the LET and is defined as the amount of energy transferred to the absorbing material per unit track length of the particle. The linear energy transfer (LET), for charged particles of a given type and energy is [15]:

$$LET_\Delta = \frac{dE_\Delta}{dl} \tag{2.18}$$

This quantity is usually expressed as $keV\,\mu m^{-1}$. Only collisions with an energy transfer inside a certain range Δ are considered. Collisions which have a greater energy transfer produces delta electrons, which are able to further ionize the medium. LET and dose are linked through [16]:

$$D = \frac{\phi * LET}{\rho} \tag{2.19}$$

14

Were D is the dose, ρ the volumetric mass of the material and ϕ the particle fluence.

Heavy charged particles, including protons, neutrons etc., have a higher LET then photons, thus these particles have a higher ability to destroy DNA efficiently. A result of this, is that these particles have more severe biological effect per unit of absorbed dose. Using a low LET particle such as photons, means that the number of ionization tracks has to be increased to deliver the same damage to the malignant tissue. High LET particles, having a LET higher than 100 $keV/\mu m$, have a much higher density in the ionization and may at times deliver a higher dose then necessary to kill a cell [17].

Relative Biological Effectiveness (RBE) is a quantity which is closely related to the LET. RBE allows the quantification of the impact that different types of radiation have on biological material. The RBE depends on several parameters, such as the energy of the traversing particle, depth of the tissue being irradiated, and the dose per fraction. The RBE is defined as:

$$RBE = \frac{D_X}{D_R} \tag{2.20}$$

where D_X is the dose from a reference beam, and D_R is the dose delivered from a beam that inflicts the same damage to the cell.

The motivation for looking at RBE is to compare the clinical outcome of a proton beam with treatment with a photon beam among other things. RBE can in general be used to compare two different types of radiation. The RBE is dependent on the tissue end point, LET and the dose level. To first order the radiation can be said to be more effective if the LET is higher. When the proton slows down, the LET increases, but proton therapy is currently delivered assuming a constant proton RBE with a value of 1.1. Thus patients have a physical dose which is 10% less than that for photons [10].

The RBE may vary between 1.0 and 1.5 in the region of the Bragg peak. These potential uncertainties in the RBE is important because of the relation between the RBE and LET. Thus the potential dose may increase at the edge of tumors if a spread out Bragg peak is delivered in the treatment. This uncertainty may then result in healthy tissue being irradiated.

2.3.1 Absorbed dose

Absorbed dose D is the energy ΔE that is deposited per unit mass Δm in the absorbing medium:

$$D = \frac{\Delta E}{\Delta m} \tag{2.21}$$

This has the unit Gy, where $1Gy = 1\frac{J}{kg}$. This definition gives the impression that the dose will be uniformly distributed throughout the region of interest. This, however, is not the case for heavily charged particles, which may produce secondary particles along its trajectory, which will then go on and ionize the medium as well as the mother particle. Given that the probability of dealing damage to the tissue is strongly dependent on the way the dose is distributed, this means that absorbed dose is not a good measure of damage dealt to the medium. Thus equivalent and effective dose is introduced to better describe the overall damage dealt out by the radiation. These descriptions take into account the different types of irradiating particles and the organs that are irradiated [9] [17].

2.3.2 Equivalent dose

For a specific tissue, T, the equivalent dose can be calculated as a product of the average absorbed dose by the tissue and the weighting factor w_R, depending on what type of radiation that was delivered [4] [9].

$$H_T = \sum_R w_R \times D_{T,R} \tag{2.22}$$

The weighting factor w_R varies with the energy and the type of particle that is used, values for this are listed in table 2.3.2.

Table 2.3.2	Weighting factors for different types of radiation [9]	
Type of radiation	Energy[MeV]	Weighting factor, w_R
Photons	All energies	1
Electrons, muons	All energies	1
Neutrons	< 0.01	5
	0.01-01	10
	$> 0.1 - 2$	20
	$> 2 - 20$	10
	> 20	5
Protons	> 2	5
α particles		20
and heavier nuclei		

The unit used for equivalent dose is Sievert (Sv).

2.3.3 Effective dose

Different tissue respond differently to radiation. This introduces a new parameter to accurately describe the damage that is delivered to the tissue. Effective dose includes this and is the measure of stochastic risk to the entire body for a uniform irradiation.

$$E = \sum_T w_T \times H_T \tag{2.23}$$

w_T is the normalized tissue weighting factor, H_T is the equivalent dose, and E is the effective dose. The unit for effective dose is Sievert (Sv).

2.4 Radiation therapy

2.4.1 Imaging modalities

To ensure the delivery of the dose to a target volume, knowledge of the position and form of the tumor is a necessity. Thus imaging modalities which has a high resolution and low noise is essential in radio-therapy. After imaging of the patient, the pictures are imported into treatment planning software, where oncologists set up the target area for a desired treatment. It is important to deliver a sufficient dose to the target volume, while avoiding the healthy tissue as much as possible. Different imaging modalities have been developed to locate the tumor and surrounding tissue. These imaging modalities include ultrasound, MRI (Magnetic Resonance Imaging), CT, and PET. The two latter will be discussed in this section. PET and CT are often combined into a PET-CT scanner to take advantage of both imaging modalities simultaneously [18]. A setup of a CT scanner can be seen in Fig 2.11.
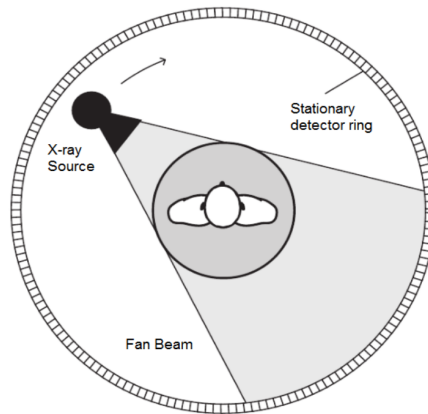
Figure 2.11: Setup of a CT scanner. A X-ray tube is rotated around the patient while producing photons, these are detected on the opposite side of the patient and may be reconstructed into images [19].

PET-Positron Emission Tomography

PET takes advantage of radioactive nuclei that are emitting positrons when they decay. This includes nuclei such as F^{18} [6].

Depending on what type of tumor that is the aim of the PET scan, different radio-nuclei are chosen based on their half-life. Tumors have a high metabolism, so high concentrations of sugar tend to be accumulated in the tumor. By attaching the radio-nuclei to a sugar molecule, one ensures that these are located in the tumor. The sugar molecule is injected into the patient. When the radio-nuclei decays, it sends out a characteristic positron. When this positron falls to rest, it will annihilate with an electron in its vicinity. Because of the conservation of momentum, two 511 keV photons will be ejected back-to-back. With detectors surrounding the patient, it is possible to locate the area where two entangled photons were produced. This is done by collimation and the time-of-flight for the photons. With a high enough statistic it is possible to locate the tumor [17].
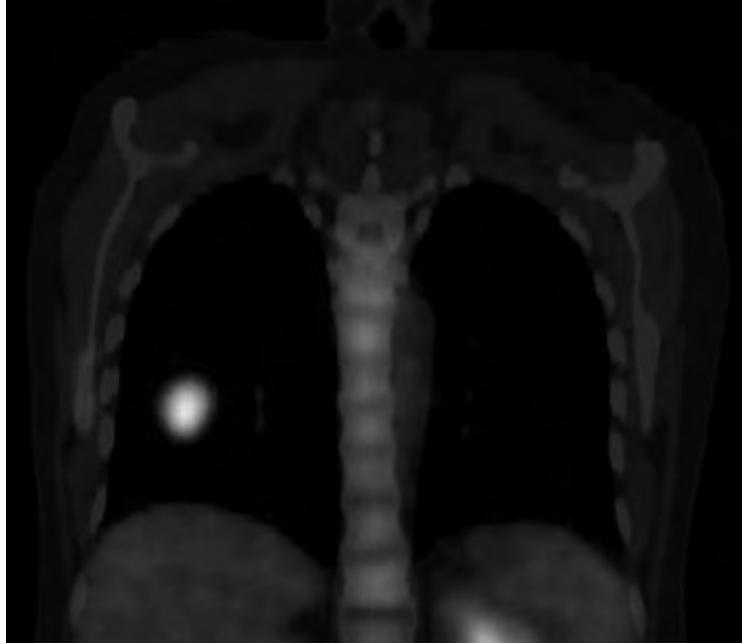
Figure 2.12: PET-image, the position of the tumor can be located to be in the lungs, this is where the photons have been produced, due to the accumulation of radio nuclei [17].

CT-Computed Tomography

Computed tomography takes advantage of the attenuation of photons traversing a medium. An accelerator produces electrons of a certain energy, typically tens to hundreds keVs, which is bombarded on to a tungsten target to produce x-rays [6]. A collimator is used to direct the photons towards the patient, and a detector is placed on the opposite side. The attenuation coefficient differs inside the body, so the photons will be detected with different energies when they hit the detector. The attenuation is measured in Houndsfield units:

$$HU = 1000 \times \frac{\mu_{tissue} - \mu_{water}}{\mu_{water}} \tag{2.24}$$

Houndsfield units is in the range between -1000 for air to +1000 for bone in the human body. Based on the values produced, a image can be produced by a technique known as filtered back projection. This gives a 3D image of the patient if the detector and gantry is rotated around the patient during the imaging production. Otherwise it is a standard 2D Roentgen picture.

Figure 2.13: CT image of the head, displaying one slice. The cranium is the part that lights up as white, this is due to the photons being attenuated a lot in this area, while the soft tissue of the brain has a gray color [17].

2.4.2 Radiotherapy with photons

Over the last decades there has been significant improvement in the delivery of treatment with photons. Previously it was only possible to have a beam delivery of rectangular shaped fields. After the introduction of multi-leaf collimator, it is now possible to shape the beam after the tumor. This will maximize the dose delivered to the tumor and reduce the dose delivered to healthy tissue. The multi-leaf collimator consists of up to 80 pairs of independently moving leaves. This form of treatment is known as conformal radiotherapy (CFRT). A more advanced form of treatment is intensity modulated radiotherapy (IMRT), which varies the intensity of the beam as well as the shape. This is to counteract the effect cavities and surface irregularities have on the delivery of dose to the tumor and healthy tissue [20]. During treatment with photons, most of the dose is deposited at the entry point of the beam, before the intensity falls off due to attenuation of the photons. Thus a lot of dose is delivered to healthy tissue. To counteract this the gantry is rotated, and different fields are used. Thus the accumulated dose of the entire treatment will have a maximum in the region of interest. To ensure that the dose is delivered to the ROI, several actions are in place to keep the patient at bay. This may involve the patient wearing a mask or other equipment to minimize mobility. The internal structure of the patient may also change during a treatment plan, so updated images of the patient are necessary if the treatment extends over several weeks.

Linear accelerator

The most common accelerator used in radiotherapy with photons is the linear accelerator. The medical linacs, accelerates electrons up to a few MeV, before having them collide with a tungsten plate. The electrons will radiate photons as they undergo bremsstrahlung. The spectrum for the photon energies will depend on the incident energy of the electrons. Thus the beam energy used in treatment is often expressed in units of mega volt, MV. The

maximum energy of the photons being used in treatment will correspond to the maximum energy of the incident electrons. I.e. a 1 MV beam will have photons with a maximum energy of 1 MeV [6].

2.5 Proton Computed Tomography and treatment with protons

Robert R. Wilson was, in 1946, the first person who brought attention to the fact that heavy charged particles may be used in cancer therapy. Today there are over 50 proton centers dedicated to cancer therapy, with over 137 000 patients having been treated so far [21].

Proton Computed Tomography (pCT) is a technology which is similar to regular CT, but differs in terms of what particle is used in the treatment. Where CT uses photons, which has a high deposit of energy in early phase of its track, before it is attenuated, pCT uses protons. Protons has the advantage of having a high deposit of energy at a certain depth, which according to eq.2.1 is dependent on the energy of the protons. This allows for an accurate delivery of a high dose to the tumor in proton therapy. For imaging of the patient, the peak of energy deposition can be set outside the patient by increasing the energy of the proton beam. Thus minimizing the dose delivered during imaging. The difference between the dose deposition of these two techniques can be seen in Fig 2.14.
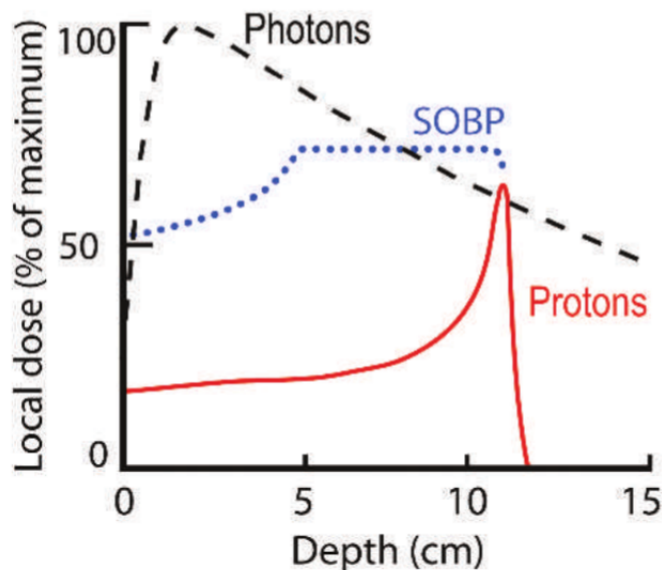
Figure 2.14: Energy deposition vs depth of Protons and Photons [22].

This accuracy in deliverance of dose is very useful in the treatment of tumors that are close to an organ at risk. This could be in the treatment of tumors such as adenocarcinoma of the prostate and invasive bladder cancer, among others [22]. Proton treatment is also favorable when it comes to treatment of children. Since the accuracy of delivery of dose is higher for proton therapy compared to radiotherapy, the ratio of healthy tissue that are radiated is lower. Thus the chance for radiation induced cancer is reduced [23].

For pCT, this difference in the deposition of energy, means that one needs a high energy

proton beam, typically 300 MeV, to be able to penetrate through the patient without having a high deposit of dose inside the patient. The energy loss of the protons must be measured in order to construct an image.
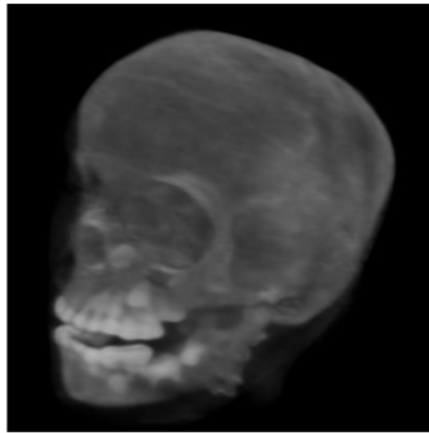
Figure 2.15: 3D rendereing of pCT-reconstructed relative stopping power map. Fig 14.[23]

One early design concept of a pCT, is to measure the energy deposited inside the patient by the individual protons. This would be done by having tracking detectors before and after the object that is to be traversed.
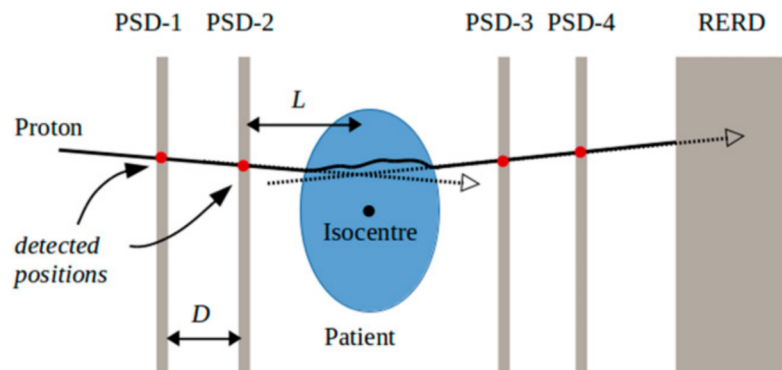
Figure 2.16: Example of a pCT setup with two tracking detectors in front of the object and two behind, followed by a calorimeter. Fig.5 [24]

Behind the tracking detector there is an energy detector (calorimeter) to determine the energy loss of the particle along its trajectory. From each of the measurements, the reciprocal stopping power for each proton can be obtained from numerical integration and comparing it to the water equivalent path length. By doing this for a multitude of protons, one would be able to reconstruct a 3D image of the object. However, this has a limited spacial resolution and is also dependent on the tracking accuracy and the method to obtain an estimate of the proton path [25].

2.5.1   pCT in Bergen

For the pCT prototype, being developed at the Department of Physics and Technology at the University of Bergen, the aim is to have an accurate and quick reconstruction of the protons that traverse through the patient. This is to be done by using a high-granularity semiconductor calorimeter. This is obtained by structuring a large amount of ALPIDE detectors, consisting of 512×1024 pixels, which are able to record a deposition of energy over a given threshold. By stacking up a number of these chips, one gets a Digital Tracking Calorimeter. It will then be possible to reconstruct the path of a single proton, as well as being able to measure the energy deposition using one device, the DTC. By using only one device to obtain the track and angle of the proton as well as the energy, one will be able to reduce the cost of the pCT and simplify the process. Given the fact that the ALPIDE detector has a high number of pixels, one can allow for the DTC to measure multiple protons per time frame. This increases the proton rate capability and greatly reduces the time needed to produce a high-resolution image.

Chapter 3

Semiconductors and Silicon Pixel Detectors

3.1 Semiconductors

The semiconductors have a crystalline structure which can provide a high-resolution energy measurement, it may also be used as a high-resolution particle tracking device. This possible duality makes the semiconductor a very interesting prospect for pCT.

Semiconductors operate in a similar fashion as the gaseous detector, but differ due to the fact that ionizing radiation creates electron-hole pairs rather than electron-ion pair. Since the semiconductor is a solid state detector, the energy needed to create an electron hole pair is about one magnitude lower than that of a gaseous detector. So the energy requirement for ionization in a gaseous detector is about ten times as high as that for a semiconductor. This property increases the resolution compared to a gaseous detector. They also have a higher density, which in turn, increases the stopping power of the detector. Because of the compactness of the detector, it also provides a fast response time compared to the gaseous detector [4][7].

3.2 Energy band structure

The Pauli exclusion principle states that two electrons may not operate in the same quantum state [26]. This leads to the outer atomic shell energy levels to split up to create energy levels which are slightly separated. For some of the energy levels operating at a low energy level this means that they are fully filled with electrons, while the high energy levels are nearly empty. The lowest of these high energy levels are known as the conduction band, while the highest of the low energy levels are known as the valence band. The region in between is the forbidden level which has a width of $E_g = V_c - V_v$.
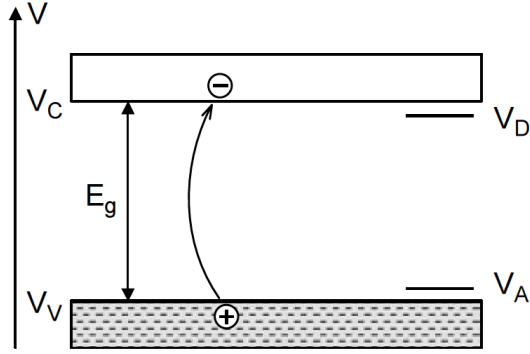
Figure 3.1: Band structure of a solid-state material. V_V and V_C are the top of the valence band and the bottom of the conduction band respectively. E_g is the width of the forbidden region [7].

The conduction and valence band are in reality regions where the energy levels are so close that they appear to operate in a way which allows these regions of energy levels to be considered continuous. In the forbidden region, however, there are no available energy regions. This structure arises in the crystalline structure because of the periodic arrangement of the atoms in the crystal, and it causes an overlap in the wave functions of the electrons.

In the conduction band the electrons are considered to be free from their attachment to their parent atoms. The electrons in the valance band, however, are bound tightly. The width of the forbidden region is dependent on temperature and pressure, because of the spacing between the atoms. For a conductor this gap is non-existent, while for an insulator this is large. When an electric field is applied, depending on if it is a conductor or an insulator, the electrons are moving easily or not at all, thus creating a current in the conductor or no current in the insulator. For a semiconductor the forbidden region has an intermediate size, allowing some electrons to flow, but not all. Depending on the temperature of the semiconductor it is possible to adjust the flow of electrons. For a lower temperature T the electrons will fall into the valance band, and the conductivity will decrease [4][7].

3.3 Charge carriers

If the temperature is 0K in the lowest energy state of the semiconductor, then all of the electrons in the valance band will participate in binding the lattice atoms. When the temperature increases to normal temperatures, some of the valance electrons will be excited into the conduction band, because of the thermal energy. When this happens, the excited electron will leave a hole in the lattice. This leads to an equilibrium in the number of holes in the valance band and electrons in the conduction band.

$$n_i = p_i \tag{3.1}$$

When the electron is excited into the valance band, a neighboring electron may slip into its hole and thus leave a hole in its original position. In this manner it will be as the hole appears as a positive charge that is moving. Thus in a semiconductor, the electric current has its origin in both the movement of free electrons in the conduction band, and the movement of holes in the valance band.

Electron-hole pairs are constantly being generated in a semiconductor if it has a temperature $T > 0$. If the conditions are stable, this will lead to an equilibrium concentration of electron-hole pairs. An approximation of this number is given by [4]:

$$n_i = \sqrt{N_c N_v} e^{-\frac{E_g}{2kT}} = A T^{3/2} e^{-\frac{E_g}{2kT}} \qquad (3.2)$$

- N_c is the number of states in the conduction band

- N_v is the number of states in the valance band

- E_g is the energy of the energy gap at temperature 0 K

- T is the temperature of the semiconductor

- k is the Boltzmann constant

- A is a material constant

For a silicon semiconductor with a temperature $T = 300K$ this would result in $n_i = 1.5\text{x}10^{10} cm^{-3}$. To put this into comparison, the order of atoms in silicon are 10^{22} atoms/cm^3. So only 1 in 10^{12} is ionized in silicon. Thus the concentration of electron-hole pairs are very low at room temperature.

After the formation of an electron-hole, both will start to drift randomly in the lattice. Thus the diffusion is away from their point of origin. This diffusion can be characterized by a Gaussian distribution. The cross section of this distribution will have a standard deviation which will give the probable distance that the charge carries have diffused away from the point of origin, after a time t, and the standard deviation is given by [27]:

$$\sigma = \sqrt{2Dt} \qquad (3.3)$$

Where D is the diffusion coefficient, and this can be estimated by the relationship:

$$D = \mu \frac{kT}{e} \qquad (3.4)$$

where μ is the mobility of the charge carriers, k is the Boltzmann constant, T is the absolute temperature and the electron charge is e.

If an electric field of low-to-moderate intensity is applied, then the charge carriers will start to drift parallel to the field. The drift velocity will be proportional to the applied field, thus the mobility μ for electrons and holes can be defined as:

$$v_h = \mu_h E \qquad (3.5)$$

$$v_e = \mu_e E \qquad (3.6)$$

In a semiconductor material the mobility of the electrons and holes are of the same magnitude. The charge carriers' velocity will vary linearly with the field strength up to 1000 V/cm. The maximum velocity is reached above the order of 10^4 V/cm, with velocities reaching 10^7 cm/s. The time required to collect these carriers over a typical dimensions of 0.1 cm or less, will be less then 10 ns. This is why semiconductors are among the fastest-responding detectors. At larger field strengths, the velocity saturates due to the collisions within the lattice. The charge carriers will also diffuse transversely with the field

lines. The effect of this is that there is some spread in the arrival position. This diffusion can be approximated by:

$$\sigma = \sqrt{\frac{2kTx}{\epsilon E}} \qquad (3.7)$$

where x represents the distance traveled by the charge carriers. This diffusion broadening somewhat reduces the resolution of semiconductor detectors [4][27].

3.4 Crystal impurities

What has been discussed so far is what is known as pure semiconductors or intrinsic semiconductors. These are fairly easy to describe in theory, but are in practice virtually impossible to achieve. This also applies for semiconductors of silicon and germanium, which are the materials which have the highest practical purities [27]. To achieve recombination of an electron-hole pair in an intrinsic semiconductor, the energy and momentum values have to be exactly right, thus this is a rare process. Theoretical calculations of the lifetime of electrons and holes show that they may live for as long as a second if recombination is the only process. However, experimental measurements show that the lifetime of carriers can range from nanoseconds to hundreds of microseconds, thus implying that there are other mechanisms involved [4].

The most common mechanisms is recombination as a result of impurities in the crystal. The alien atom in the lattice may add available energy states in the forbidden region, where electrons and holes may be captured. If an electron from the conduction band is captured in one of these states, there are two possible outcomes: (1) During the time the electron is captured, it may also capture a hole which will annihilate with the electron, or, (2) after a certain time, the electron is released and will go back in the conduction band. This may lead to a problem in the detectors. If the time the charge carries are trapped surpasses the collection time of the detector, then it will not be counted. This leads to a deterioration of the detector resolution. Another problem may be that some impurities are only capable to capture one type of charge carrier. These centers only hold the electron or hole for a given time before it is released. If this trapping time is in the same order as the charge collection, there will be an incomplete charge collection. If this time is less then the collection time, it will not be an issue.

Impurities are the main source of recombination and trapping, but structural defects in the lattice may also create similar states in the forbidden band. This can be displacement of an entire line of atoms or simple point defects, which are vacancies in the lattice or atoms which are occupying space between lattice points. This may rise from bombardment of radiation, and is thus an obvious problem for a detector [4].

3.5 Doping

At times it is desirable to create impurities in the crystal. This can be achieved by doping the crystal. This includes changing the equilibrium of electrons and holes in the conduction band. By introducing an atom which has one more or one less valance electron, these impurities may be achieved. Since silicon and germanium have four valance electrons, this means that the atom which is introduced either has an extra electron or has an open space in the outer shell.

In the case where there is one extra electron, this resides in the energy gap, but very close to the conduction band. This electron is easily excited into the conduction band and will enhance the conductivity. These doped semiconductors are called n-type semiconductors, and the main charge carriers are electrons.

If the impurity is created by having three valance electrons, there will not be enough electrons to fill the valance band. Thus there are an excess of holes. Now the additional energy state is created close to the valance band, and electrons are then easily excited into the valance band. This is called a p-type semiconductor, and the main charge carriers are the holes [4].

3.6   PN-junction

Semiconductor diodes can be formed by a simple configuration such as the pn-junction. If there is a surplus of electrons, one obtains an n-type semiconductor, and with a surplus of holes one obtains a p-type semiconductor. A clean crystal has an equal amount of holes and electrons, but if the Si atoms are doped with an atom which has five valence electrons, one gets an electron in spare. This leads to the crystal being negatively doped. This can be done in a similar fashion to create a positively doped crystal, but then one uses an atom with three valance electrons [9].
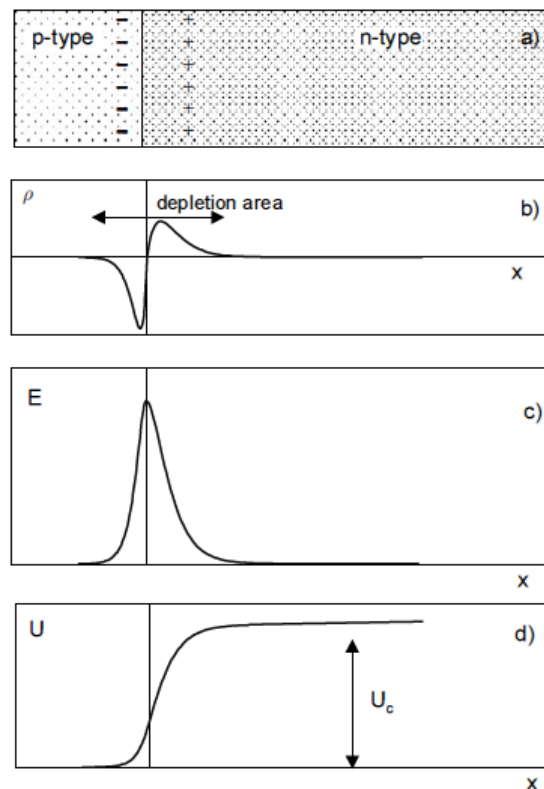
Figure 3.2: (a) Working principle of a pn junction; (b) space-charge distribution including all kinds of charge carriers: free electrons and holes; (c) electric field; (d) potential distribution. When no external voltage is applied, the maximum potential is equal to the contact voltage U_c [7].

To obtain the pn-junction, two extrinsic semiconductors are brought together with different doping, one positively doped and one negatively. When these are joined, electrons from

the n-doped side starts to diffuse into the p-doped, and holes will diffuse to the n-doped side. This leads to a surplus of electrons in the p-doped, and similarly a surplus of holes in the n-doped side. When this happens, an electric field occurs. This is to counteract the diffusion of electrons and holes, and as a consequence a depletion region or space charge region occurs. This has the property that it has no mobile charge carriers. Suddenly the pn-junction has the properties of a diode. All particles which enters this zone will create electron-hole pairs, which in turn will be swept out by the presence of the electric field. The depletion region created by the pn-junction alone will not necessarily create the best operating detector, and thus a bias voltage is often applied [4].

If a bias voltage is applied, the properties of this depletion region will change. If a reverse bias voltage is applied, holes will be drawn away from the junction. As a result the depletion region will increase in size. The effect of this is that the sensitive volume of the detector increases, the charge collection will also be more effective. The opposite will happen if a forward bias voltage is applied, in this case the depletion region will shrink as a result.

The collection time for electrons and holes is dependent on the location of the charge with respect to the electrodes. Thus the pulse shape from the semiconductor may vary in rise time and form. The electrical pulse on the electrodes comes from the induction caused by the movement of the charge, instead of the collection of the charge itself [27].

3.7   Pixel detectors

The pixel detector was developed when there was a need to detect short lived particles and to have the capability to cope with high interaction rates and energies. A pixel can be defined as the smallest discernible element in a given process or device. A pixel detector is thus a device which is able to detect an image, and the size of the pixel corresponds to the granularity of the image [28]. A pixel detector operates in a way that allows them to be excellent tracking detectors. When an ionizing particle traverses the sensor layer of the detector, it generates a charge. This charge will travel until it enters the depletion region, where it under the influence of an electric field will be collected. This will produce a signal, which is then amplified, selected, and stored in the electronics. The area of the sensitive part of the detector is dependent on the bias voltage which is applied and on the sensor parameters. A schematic of a pixel detector can be seen in fig 3.3.
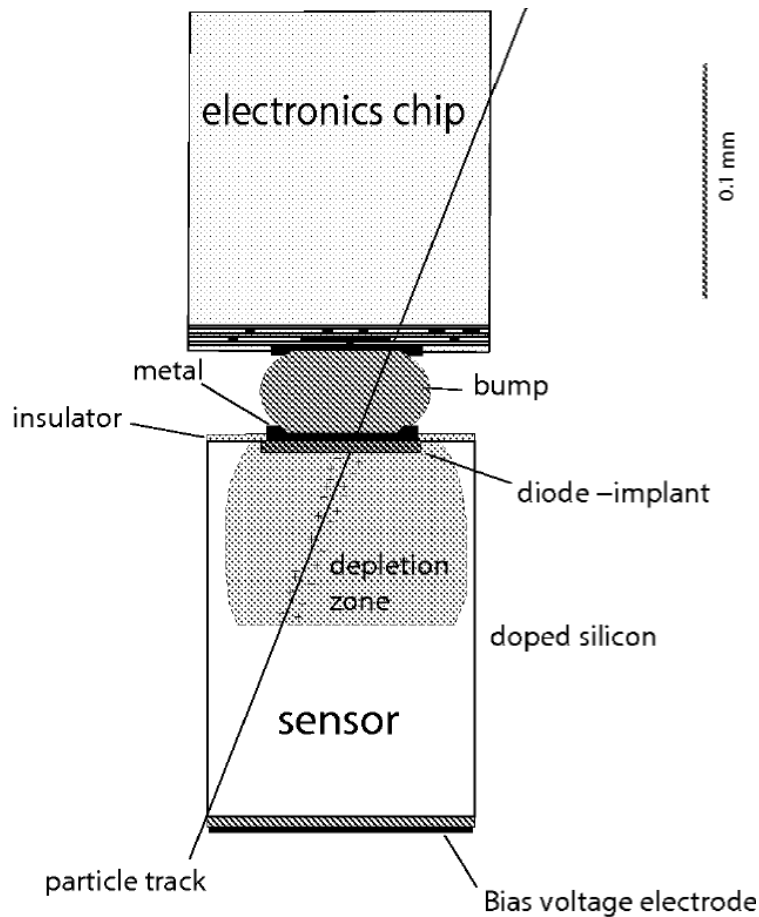
Figure 3.3: Schematic view of a hybrid pixel detector [28].

With the use of planar integration technology it is possible to stack up several thousands of these pixels in a matrix which can cover a few square centimeters. By adding a lot of these matrices it is possible to cover a large surface area.

3.7.1 Monolithic Active Pixel Sensors

The CMOS MAPS is a device which is position sensitive for high energy charged particle tracking. It typically has an epitaxial layer of a few to 15 μm. The term "active" arises from the fact that an amplifier is integrated into each pixel, this will buffer the signal charge. One of the advantages of a monolithic active pixel sensor is that it is possible to have the front-end read out electronics and the detector on the same wafer.
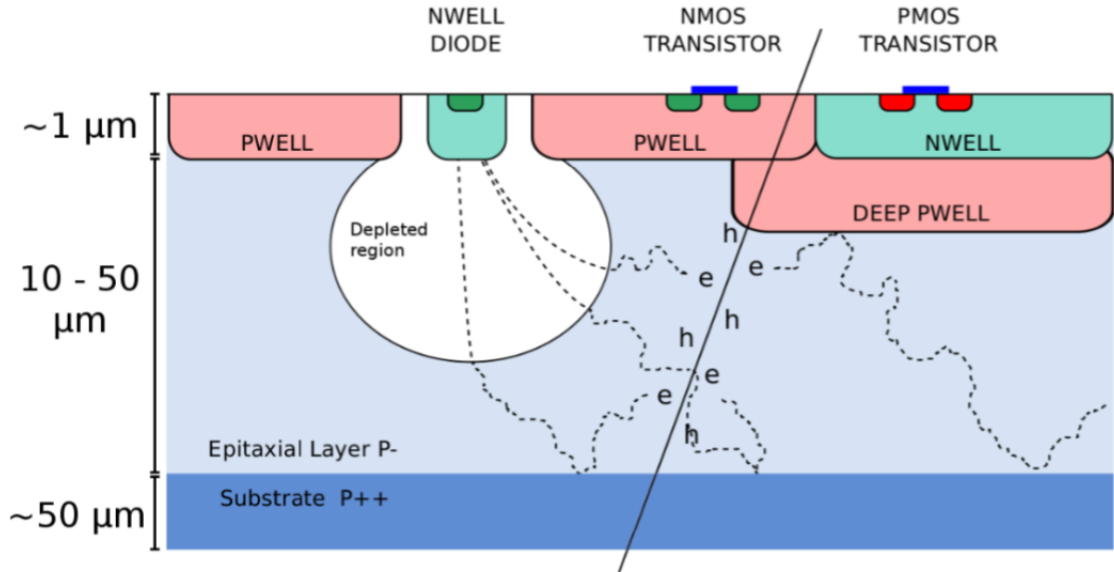
Figure 3.4: Illustration showing the collection of charge in MAPS (not to scale) [29].

The epitaxial layer operates as the active volume of the detector. It consists of a lightly doped p-type silicon which is mounted on a highly doped p++ substrate. The p-type and n-type wells are implanted on top of the epitaxial layer. The diode, which is established by a p-type/n-well epitaxial layer junction, has the responsibility of collecting the electrons which are liberated by the ionizing particle. Most of the epitaxial layer is free from the electric field, so the charge carriers reach the collection diodes by thermal diffusion [28]. Because of this a MAPS detector has a relatively long collection time in the region of 100 ns. Since there is fast recombination of electrons and holes, most of the charge which is liberated in the highly doped substrate will be lost. Some fraction of these charges can however diffuse from the substrate to the epitaxial layer and have a contribution to the total collected charge [30].

There is typically a difference between the doping levels of the lightly doped epitaxial layer and the p-well, and p++ substrate has a difference of three orders of magnitude. This creates a potential barrier at the boundaries, which in turn acts like a mirror to the excess electrons.

The MAPS detectors have demonstrated to be excellent tracking detectors for the following reasons:

Table 3.1	Properties of MAPS
i	High detection efficiency exceeding 99%
ii	Single point resolution below 2 μm for a detector equipped with pixels of 20 μm pitch.
iii	MAPS can be thinned down to 50 μm, this will minimize multiple scattering.
iv	Fast readout compared to CCD (Charged coupled device).
v	Less sensitive to radiation damage compared to CCD.
vi	Cheap to produce when equiped with CMOS technology.

Chapter 4

ALPIDE Detector

4.1 ALICE ITS upgrade

The ALICE experiment at CERN is one of the four large experiments that are stationed around the LHC, designed to focus on heavy-ion collisions and the strong interaction sector of the Standard Model [31]. The ITS part of ALICE is a multiple layer, silicon vertex detector stationed in the center of ALICE. An upgrade is scheduled to take place in 2019-2020, during the second LHC shutdown, and aims to place the first detection layer closer to the beam line. This upgrade will improve the maximum readout rate, granularity, and reduce the material budget [32].

Fig 4.1 illustrates how the ALPIDE chips will be arranged in the new ITS. There will be seven detector layers after the upgrade, where the outer two and the middle one will be operated in the Outer Barrel mode. This will reduce the output data rate of these chips compared to the remaining inner layers, which will be operated in Inner Barrel mode. These configurations will be explained in Section 4.1.2.
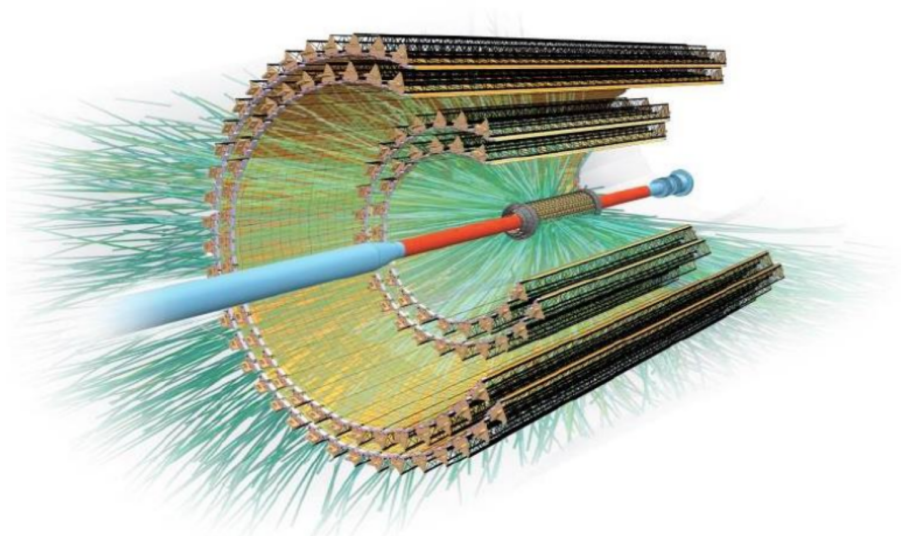
Figure 4.1: ALPICE ITS layout [33]

4.1.1 ALPIDE chip

The ALPIDE chip was developed for the ALICE ITS upgrade. It is based on MAPS and is implemented in 180nm CMOS technology.

Table 4.1: ALPIDE specifications

Total die size:	30mm x 15 mm
Pixel area:	29.4mm x 26.88 mm
Pixel arrangement:	512 x 1024
Thickness of epitaxial layer:	18 μm
Total thickness:	350 μm

Each of the pixels contain a sensing diode, a discriminator, a digital section, and a front-end amplifying and shaping stage. A schematic of this can be seen in Fig 4.2.

The front-end and the discriminator are always active. They feature a non-linear response, and their transistors are weakly biased. It is possible to operate the ALPIDE in triggered mode since the front-end and discriminator act like an analogue delay. If the latency of the incoming trigger is comparable to the peaking time of the front-end, which typically has a value of the order of 2 μs, then the pixel will record a hit.

A common threshold level can be applied, and will be set universally to all of the pixels. This threshold can be set by the user. A hit can be registered if a STROBE signal is applied to the cell in question, while the front-end output is above threshold. A STROBE signal is generated globally for the whole chip by an external trigger, and it can also be initiated internally. The width of the STROBE can be set by the user. When these conditions are met, the hit will be stored in one of the three in-pixel memory cells. The priority of the readout will differ if the STROBE is generated internally or externally. When the ALPIDE is run in external trigger mode, it will give priority to the memory readout over the registration of new hits. If the ALPIDE is operated in internal mode, it prioritizes new hits over the memory [33].
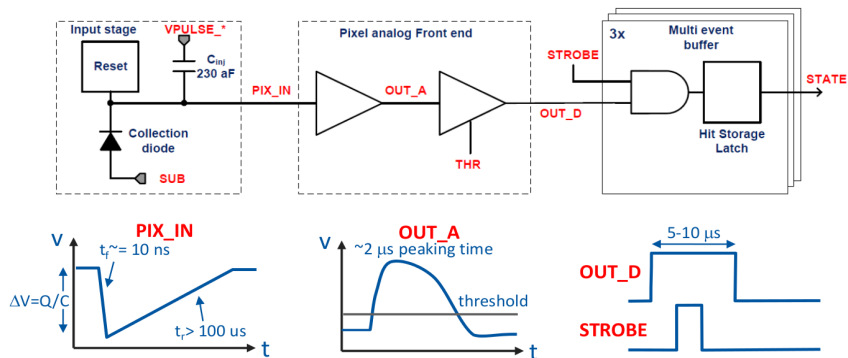
Figure 4.2: Block diagram of ALPIDE pixel cell [33]

The readout of the hit information in the pixel data from the matrix, is based on a circuit called Priority Encoder. For every two pixel columns there are these instances, making it a total of 512 double columns.
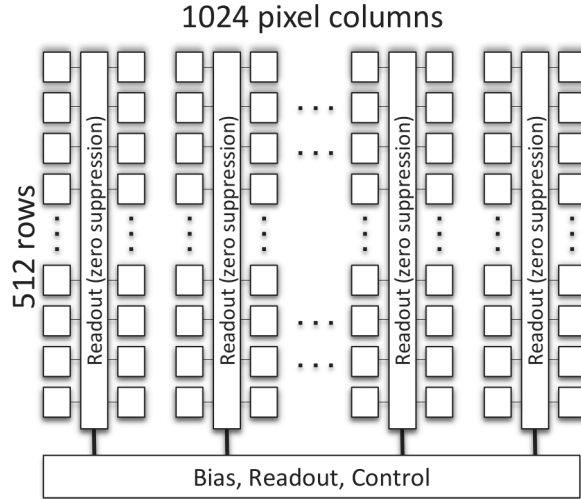
Figure 4.3: Architecture of the ALPIDE chip [33].

4.1.2   Modes of operation

The ALPIDE can be operated in the following modes: Inner Barrel Chip, Outer Barrel Master and Outer Barrel Slave. The ALPIDE has these modes to operate in different ways depending on where the ALPIDE is to be placed in the ALICE ITS detector. For the proton CT the particle rate will be high, this corresponds to the Inner Barrel Chip mode, which is developed to handle a high data transfer.

ALPIDE Configuration	Serial Link Utilized	Parallel Port Utilized	Description
Inner Barrel	Yes	No	Programmable Serial Link Speed. Default is 1200 MB/s, but can optionally use 400 Mb/s or 600 Mb/s
Outer Barrel Master	Yes	Yes	Samples the parallel port and forwards stream to Serial Link transmission. Serial Link transmission at 400 Mb/s
Outer Barrel Slave	No	Yes	Transmits data over parallel port. Data is then to be serialized and transmitted on Serial Link by Master

4.2 ALPIDE Control Interface

The control interface has two purposes. To provide write and read access to different registers and to distribute trigger commands. By manipulation of these registers the ALPIDE can operate in different modes.

- **Config 1:** Controls the Pixel MEB masking by changing one of the bits in the register, it is possible to mask one or several of the Memory Event Buffers in a pixel. This can be done to provoke a BUSY signal or to mask a pixel completely if it is noisy. Internal STROBE generation, can have either 0 or 1 depending on if it is activated. When the ALPIDE is run in continuous mode, one external trigger is used to activate the sequence, before the internal STROBE generator starts to produce triggers. The trigger rate can be set by the user. BUSY monitoring, can be enabled to make the ALPIDE ignore triggers, monitor if there was a BUSY signal sent or ignore the BUSY signal. Enable Test STROBE, will generate an internal TRIGGER pulse after it receives a PULSE command. Trigger delay, can increase the delay between the trigger command and the internally generated STROBE signal.

- **Config 2:** Controls the STROBE duration of the pulses that are sent out to the pixels. This is connected to the internal clock, so the step size for the STROBE duration is 25 ns.

- **Config 3:** If the internal sequencer is active, then the gap between STROBE pulses can be set. This has a step size of 25 ns.

- **Pulse 1:** Controls the delay between the PULSE signal arriving to the STROBE signal being generated. This is only used when the automatic generation of STROBE following PULSE is enabled. This has a step size of 25 ns.

- **Pulse 2:** Sets the length of the PULSE signal, it has a step size of 25 ns.

- **Status 1:** Gives the value of the FROMU (Framing And Management Unit) trigger counter.

- **Status 2:** Gives the value of the STROBE counter. Every time a global STROBE is issued to the pixel, this value increases.

- **Status 3:** Counter for the Matrix readout. Every time the RRU (Regional Readout Unit) has completed a readout of a matrix frame, this increases.

- **Status 4:** Gives the value of the Frame counter. This is increased when the FROMU sends a Chip Header message to the TRU(Top Readout Unit).

- **Status 5:** Gives information of the Bunch counter, number of events in the Multi Event Buffers and if the Frame is extended.

Once the registers have been set, they are distributed to the whole chip.

4.3 ALPIDE Operation

4.3.1 Front-end

Each sensor pixel in the ALPIDE matrix has a sensitive area. When a particle hits the pixel, it generates charge carriers in the epitaxial layer which is collected by the diode. The analog front-end circuit transforms the signal from the diode to a digital signal which is sent to the digital section of the pixel. If the corresponding strobe signal is asserted at the same time as the signal from the front end, then the hit state register of the pixel is set to 1. Each pixel has a Multi-Event-Buffer (MEB), capable to store a hit. This MEB consists of three state registers which all can store one hit. Thus the pixel are able to store a maximum of three hits at the same time. Depending on which readout mode is used (see Section 4.3.3.), the busy signal can be asserted depending on the number of filled MEB.
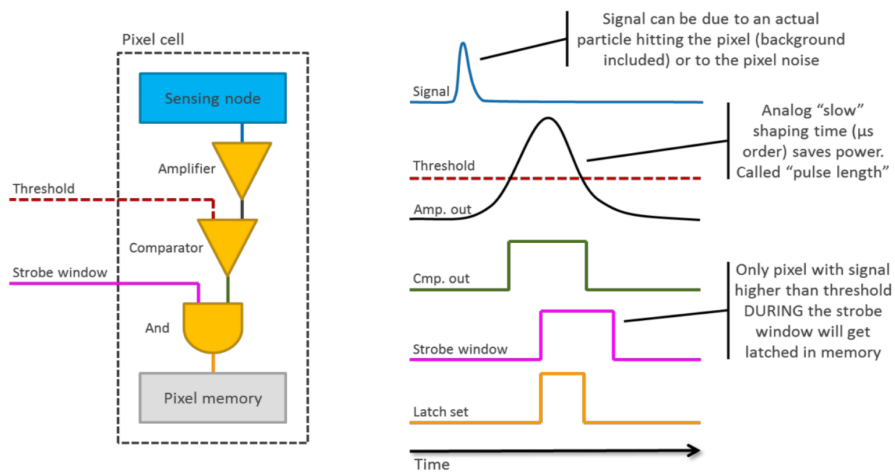
Figure 4.4: Pixel logic schematic and timing diagram [34].

Fig 4.4 shows a simplified schematic of the pixel logic, while a more detailed schematic can be seen in Fig 4.5. The signal from the front-end discriminator is typically in the order of μs, while the strobe duration can be set by the user. If the signal from the front-end is such that it covers two strobe windows in close vicinity, the signal may be latched onto both of the strobes. Thus the pixel will register a hit several times.
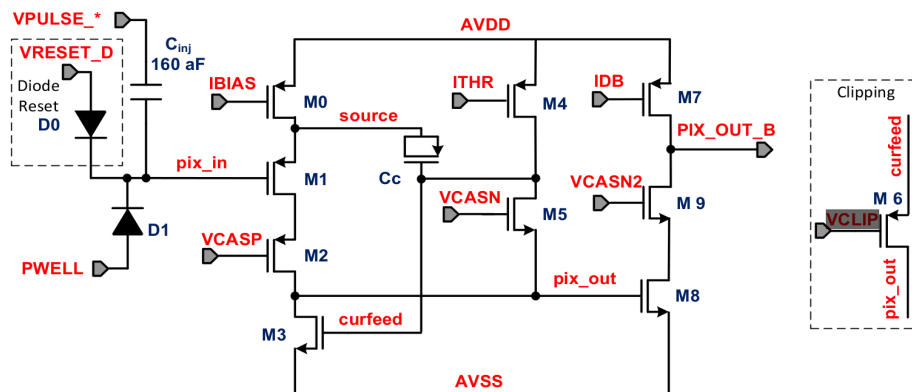
Figure 4.5: ALPIDE front-end scheme [33]

Clipping of front-end signal

In order to limit the pulse duration for very large charge collections, the clipping transistor (M6 in Fig 4.5) is implemented. If the signal produced by the incident particle is larger than 1.4 times the charge threshold for PIX_OUT and PIX_OUT_B, the clipping effect becomes noticeable [35]. When the clipping effect sets in, the signal from the front end starts to drop immediately. This results in larger charge collections to have a shorter time over threshold than lesser ones. This effect typically sets in for $Q_{inj} > 500e^-$ [36]. Thus for heavy charged particles such as protons and αs, the charge produced is so high that all signals collected are clipped.

4.3.2   Priority Encoders

The ALPIDE is separated into 32 regions (Fig 4.6), each containing 16 double columns (Fig 4.7).
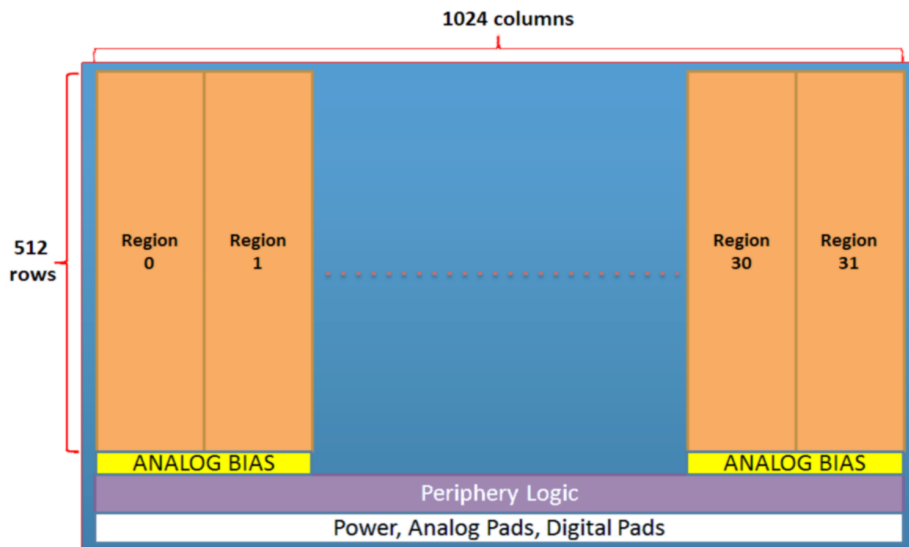
Figure 4.6: Region numbering [33].
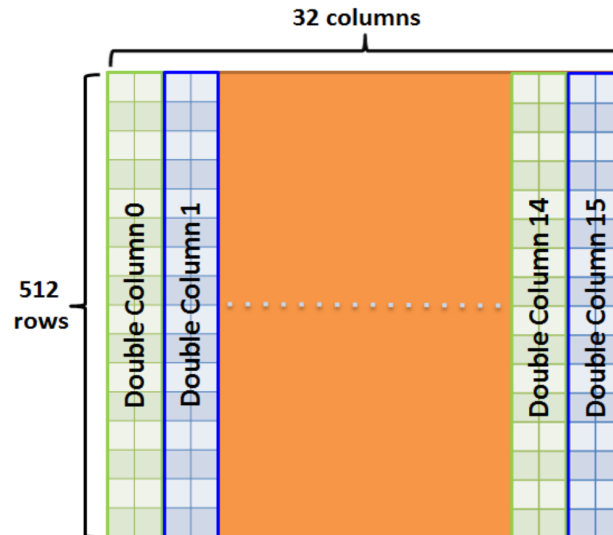
Figure 4.7: Double column numbering inside a region [33].

The read-out of the pixels are done by 512 Priority Encoder blocks, and these are set in the middle of each of the double columns. The Priority Encoder provides the address of the first pixel, which contains hit information in the double column, to the periphery. After the address has been generated and transmitted to the periphery, the in-pixel memory is reset. The cycle is then repeated for the next pixel which contains hit information in the double column, until all pixels that were hit are registered and have been reset. It starts the readout at 0 and goes up to 511.

4.3.3 ALPIDE Triggering and Framing

The main task of the ALPIDE is to store hit information from the front-end discriminators for every pixel, and transmit this information off the chip. The window in which this collection of pixel information is taking place is called a frame. A frame will be generated and sent off the chip after a trigger is issued. This will be described in detail further on in this section.

The readout of the chip takes 100 ms, and when this will occur can be controlled by the user. To avoid the loss of data, each pixel has three in-pixel data storage elements, which are known as buffers, all together they form a Multi event buffer (MEB). This is the responsible part of writing and reading the data, and this sequence is illustrated in Fig 4.8.
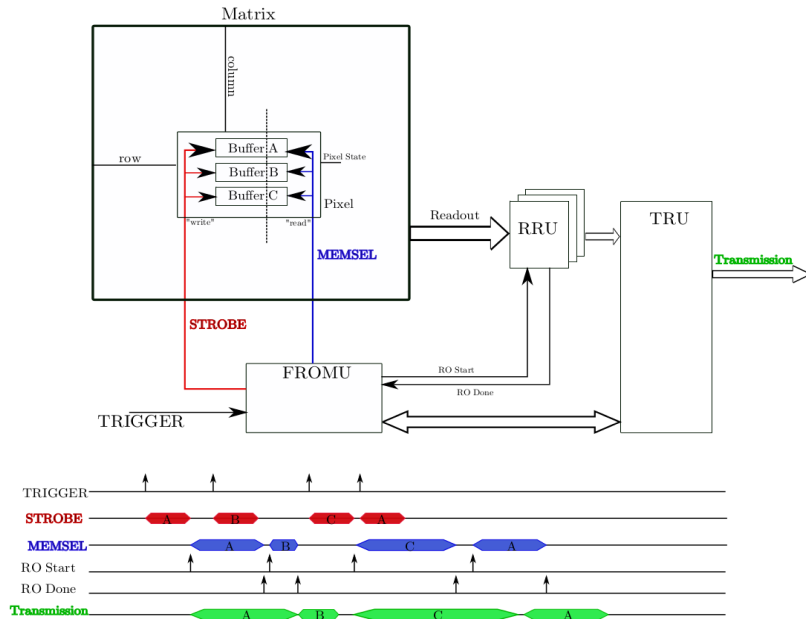
Figure 4.8: MEB management for a single pixel [33].

The recording of the signal from the front-end discriminator is controlled by three global signals, which are distributed to all of the pixels. A trigger can be issued either internally or externally via the control interface. This will initiate the STROBE signals. The STROBE which is issued is called the framing interval. The output of the pixels can be connected to the input coming from the Priority encoders. This is managed by three global signals known as the MEMSEL. Only one of the registers can be read out at the time. These act as write and read pointers to the matrix event buffers.

The readout starts at the end of the STROBE signal, where the 32 matrix regions of the ALPIDE are read out simultaneously, by specific region readout units (RRU). Each of these stores the data in local memories before the Top Readout Unit (TRU) gets all the information from each of the RRUs and the FROMU register and transmits the data of the chip [33].

Readout Modes

The ALPIDE may be operated in two different readout modes, triggered mode or continuously. These modes have been constructed for different usage.

The triggered mode is to be operated when the sampling is of a short time interval. The matching of the front-end discriminator signal and the duration of the STROBE signal, determines if the pixel hit are latched on or not. All pixels which are firing during the duration of the STROBE signal are latched on as a hit. Typically for this mode, the strobing interval is controlled by an external trigger source. The readout of the chip when it is operated in this mode, prioritizes events which are already stored in the matrix over new incoming triggers. If a new trigger is issued during the readout of a memory, then this trigger will be ignored until the readout is completed, and will thus not generate a new strobe signal. The triggers that were issued during the read out of a buffer, will appear as empty in the data.

The continuous mode is for providing readout of pixels sampled in periodically repeated strobing intervals. The framing intervals of the STROBE signal will typically be in the order of a few μs, and the gap between two consecutive STROBE signals will be kept as small as possible, typically in the order of a few hundred nanoseconds. When the ALPIDE is operated in this readout mode, it prioritizes newly received triggers over the data which is already stored. To accommodate this readout mechanism, the ALPIDE needs to ensure that there is always one available storage element in the matrix. This way it ensures that there will always be an available memory to store the newly received frames in. To do this the ALPIDE deletes the pixel hit data of the frame that it is reading out. When the ALPIDE receives a framing request to the last free matrix buffer, it will interrupt the ongoing readout in order to clear one of the MEB slices. The data packet which is associated to the readout that is interrupted will contain any information that was read out until the interruption.

Extension of the Strobe window

If a trigger is issued while a framing window is open (the STROBE signal is not closed), the window duration will be extended. This extension has the length of the ongoing STROBE window. So the total length of the framing window will be the time that has already passed in the first STROBE, before the new trigger was issued, plus the duration of the next STROBE [33].
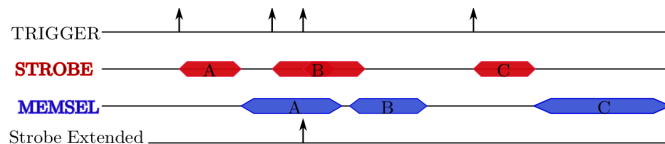
Figure 4.9: The extension of a strobe following the issuing of a second trigger[33].

Chapter 5

Characterization of ALPIDE

5.1   Experimental setup Bergen
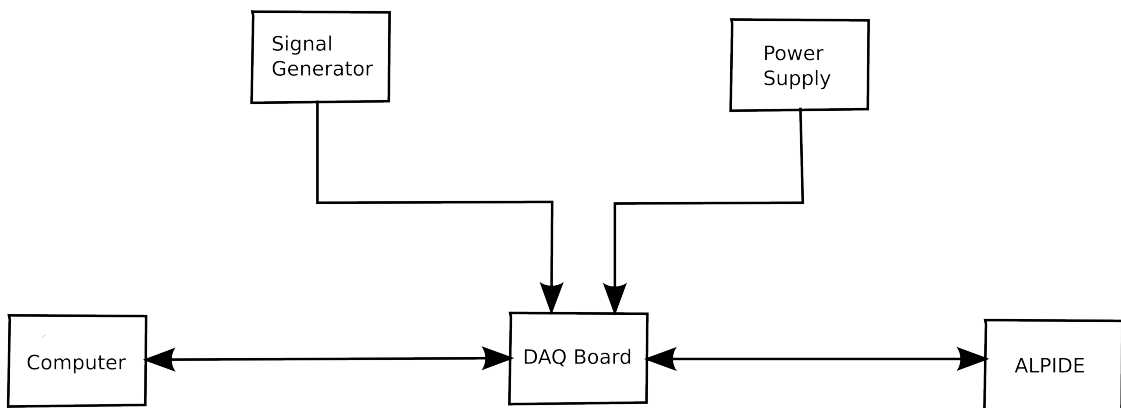
Figure 5.1: Experimental setup in Bergen

The power supply provides a 5 V voltage to run the DAQ board, and if wanted, a reverse bias voltage which can be distributed to the collection diodes. Communication with the ALPIDE is handled by a computer via the DAQ board, and the signal is communicated through a micro USB cable. The signal generator provides the trigger signal if the ALPIDE is run in external trigger mode, or to provide the first trigger signal to start the internal sequencer.

5.2   Charge threshold

The charge threshold can be measured by injecting a charge into each of the pixels multiple times and then look at the response from the ALPIDE. By doing this, one can deduce the probability of the pixel firing for a given charge. By increasing the charge it is possible to obtain the charge threshold for each individual pixel. To perform this test, the internal generation of a charge is used. The injected charge is generated on the DAQ board, before it is injected into the pixel. A multitude of signals with the same charge is injected, and

by looking at the response from the ALPIDE for the given charge, a firing probability can be estimated.

(a)   (b)
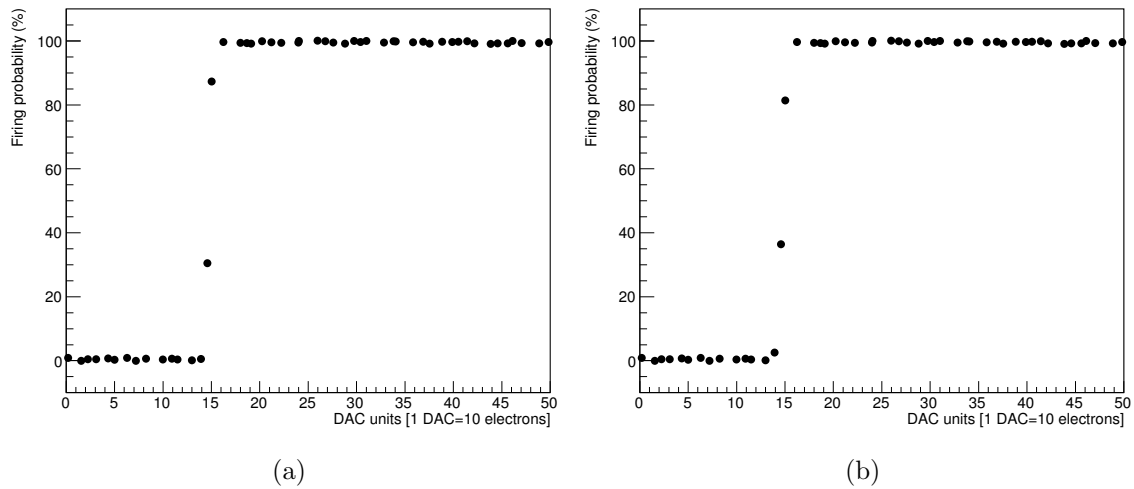
Figure 5.2: Firing probability as a function of injected charge. $V_{BB} = 0V$, $I_{thr} = 50DAC$. (a) and (b) represents two different pixels

From Fig 5.2 it can be seen that the pixel starts to fire when the injected charge is of a level of approximately 150 e⁻. At the start there is no response as the injected charge is low. Around 15 DAC units it starts to respond, and the threshold is defined where the firing probability reaches 50 %. Above a certain charge there is a full response from the pixel for all of the charges.

Figure 5.3: Firing probability as a function of injected charge for 32 different pixels

From Fig 5.3 it can be seen that the threshold varies for each individual pixel. This is due to in pixel variations as the global threshold was set to be the same for a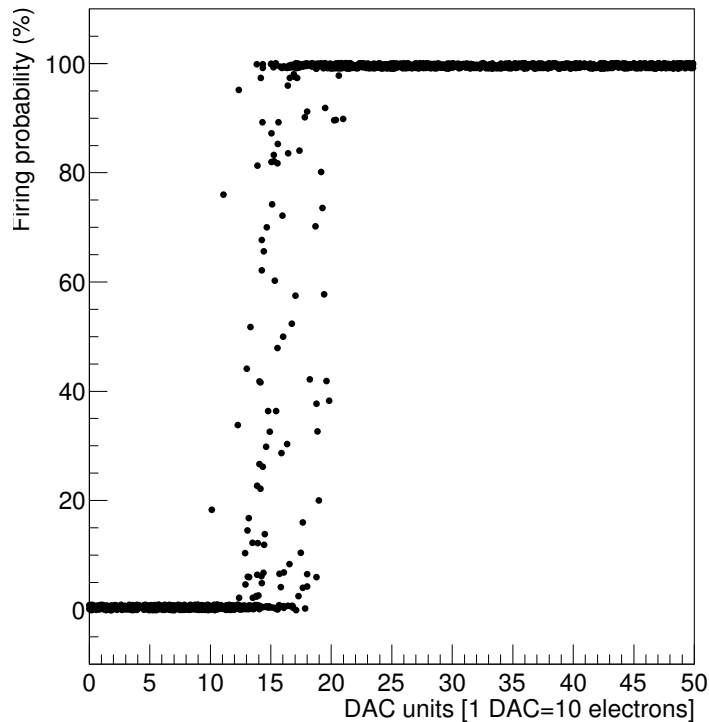ll measurements. The variation have a dependence from the pixels being exposed to different levels of radiation, as the ALPIDE in question has been exposed to radiation prior to these measurements. The variation also stems from the manufacturing process, and is in turn inevitable. These effects will affect the local threshold on each individual pixel. The threshold ranges from 10-20 DAC units for the different pixels, and this will effect the time-over-threshold for the front-end discriminator signal and could thus affect the cluster size and shape produced by an incoming particle.

5.3   Cluster size and shape

When an incoming particle penetrates the epitaxial layer, it will produce electron-hole pairs. These will start to drift and will be collected by the collection diodes attached to the individual pixels. This section will look into the different aspects of what influences the cluster sizes and shapes.

5.3.1   Reverse bias influence

The reverse bias which is applied to the system will affect how the charge spreads in the system. A cluster is defined as the formation of pixels that are firing because of the charge that is injected from one particle. When the reverse bias voltage is increased, the depletion region of the diode expands in volume, giving the charge carriers a limited area to drift in before they are collected [37]. The electrical field in the epitaxial layer will also increase, which in turn will affect the trajectory of the charge carriers. Thus the reverse bias will affect the cluster size and shape.

5.3.2   Trigger rate and strobe duration

The ALPIDE can be operated in triggered mode or continuous mode. Depending on which one is chosen, there are certain parameters that can be set by the user. When operated in triggered mode, the strobe duration must be set such that the strobe does not exceed the trigger period. This is to avoid the extension of a STROBE signal (see Section 4.3.3.). When the trigger period is smaller then the time-over threshold from the front-end discriminator, each pixel is registered multiple times. This gives the possibility of observing how a cluster evolves. Different parameters such as drift time of charge carries in the system and time over threshold for the front-end signal can be deduced from this.
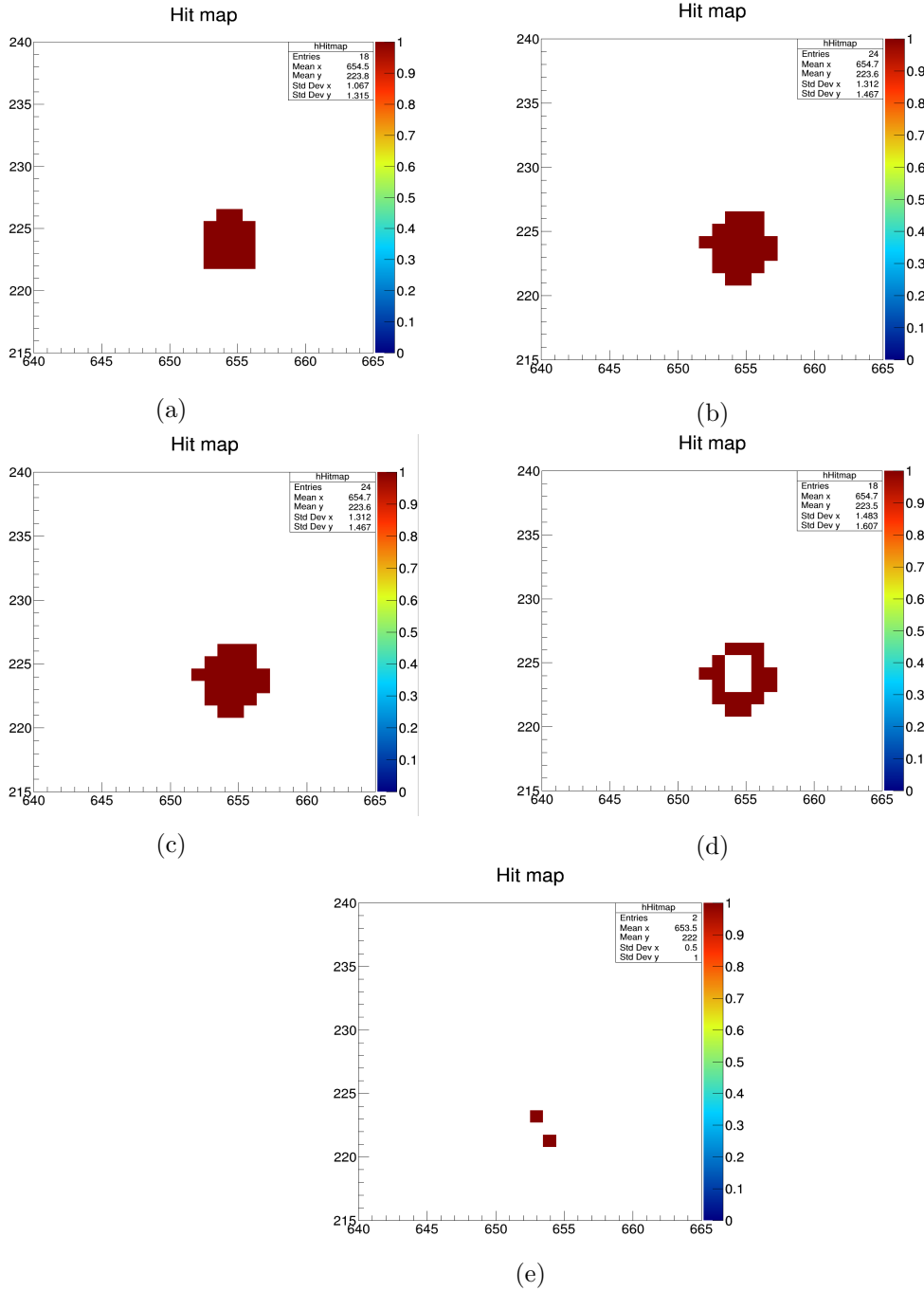
Figure 5.4: Evolvement of a cluster. $V_{BB} = 0V$, $I_{thr} = 50$ DAC, trigger rate of 1MHz and strobe duration of 750ns. Each image represent one individual frame, of a duration of 1 μs, listed in consecutive order, for a total duration of 5 μs.
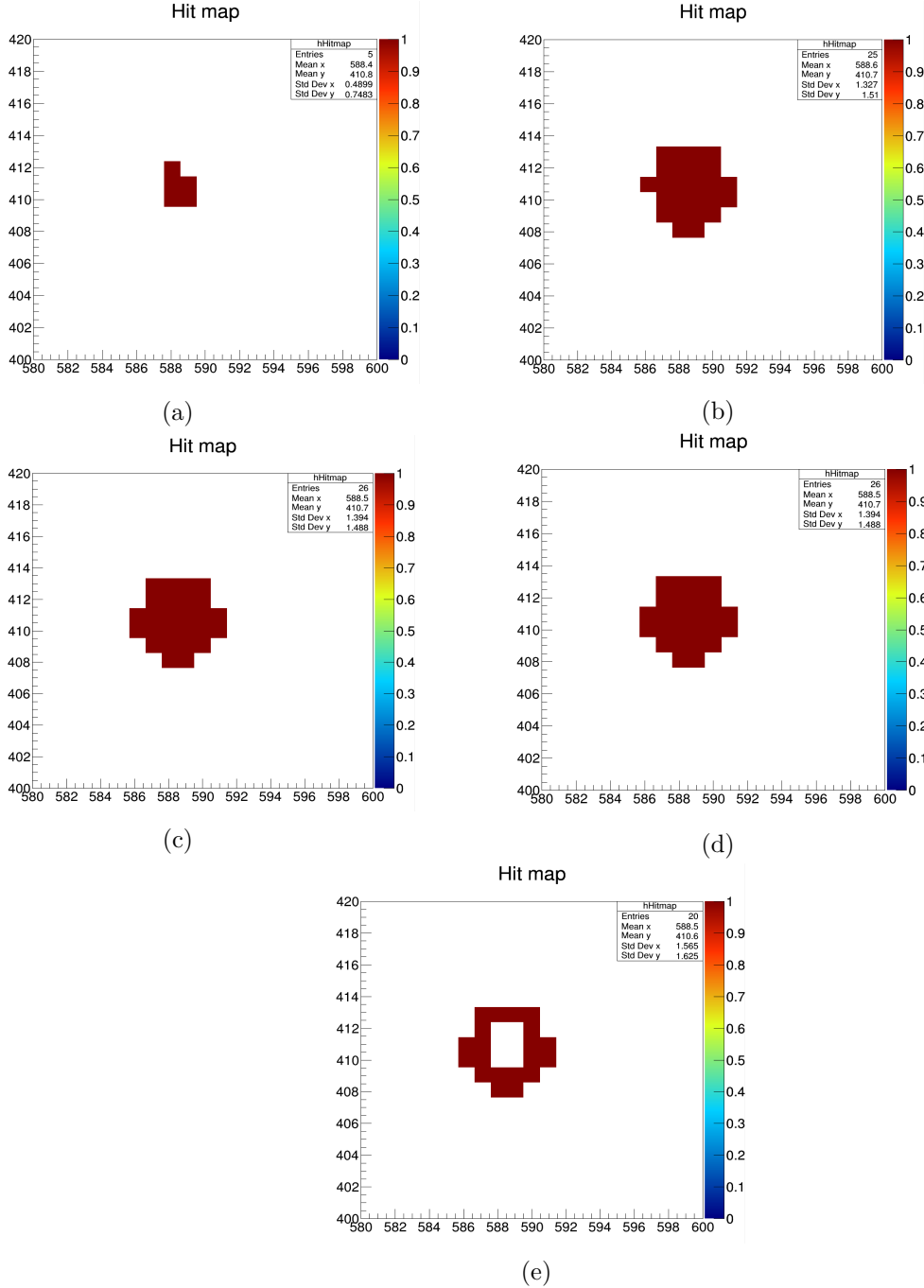
Figure 5.5: Evolvement of a cluster. $V_{BB} = 0V$, $I_{thr} = 50$ DAC, trigger rate of 1MHz with a strobe duration of 750 ns. Each image represent one individual frame, of a duration of 1 μs, listed in consecutive order, for a total duration of 5 μs.

How a cluster evolves can be observed in Fig 5.4 and Fig 5.5. The pixel starts to record a hit as soon as the charge in the front-end surpasses the threshold. With a small strobe duration it is possible to observe how the charge spreads in the epitaxial layer before being collected. In Fig 5.4 it can be observed that the time it takes before all of the pixels in the cluster start to fire and are registered by the priority encoder is between 1 μs and 1.25μs, as there is a gap in between two STROBE signals of 250 ns. It then proceeds to maintain this size into the next strobe, before the pixels in the center stop firing, giving them a time-over threshold of $\approx 3\mu$s. This short time-over threshold stems from the clipping mechanism discussed in Section 4.3.1. The edges of the cluster then disappears, leaving

44

two pixels firing for the last frame. These have a longer time over threshold than the other pixels on the edge, due to in pixel variations and an uncertainty in the arrival of the signal from the front-end. The total time-over threshold for the cluster can be observed to extend over five frames, giving the cluster a lifetime between 4-5 μs. In Fig 5.5 the first recording has a smaller size than in what was observed in Fig 5.4. This indicates that the signal from the front-end discriminator was received later for this particle in respect to the strobe window. The cluster then starts to spread out, but not all pixels are firing, indicating that there is a drift time for the charge carriers in the epitaxial layer before they are collected by the diodes. The main interaction for the charge carriers is Coulomb scattering, thus the path of the carriers are statistical in its nature. The cluster then maintains its shape for 1 μs before the center disappears. The growth and shrinkage of the clusters in terms of when the front-end signal is measured is illustrated in Fig 5.8 and Fig 5.9. The ALPIDE is developed for MIP particles which induce a smaller charge than the alpha particles used in this experiment. A MIP typically produces a charge of 700 electrons, which corresponds to 600 mV. An alpha particle, however, produced a charge which is several magnitudes higher. To handle this the ALPIDE has a clipping mechanism of the signal, thus the signals produced are clipped. This gives a shorter time-threshold in spite of the fact that alphas create a higher charge [33].

If the STROBE duration and trigger rate are set such that

$$STROBE > TOT$$

while avoiding the extension of the STROBE window, then the arrival of the signal from the front-end in respect to when the trigger was issued will determine if the hit was latched onto one or two different strobes. The time-over threshold for a cluster can be estimated from this. Knowing the size of the strobe window, the time-over threshold is given by the ratio of hits that occur consecutively if the particle rate is low compared to the trigger rate. These type of events can be seen in Fig 5.6 and Fig 5.7.
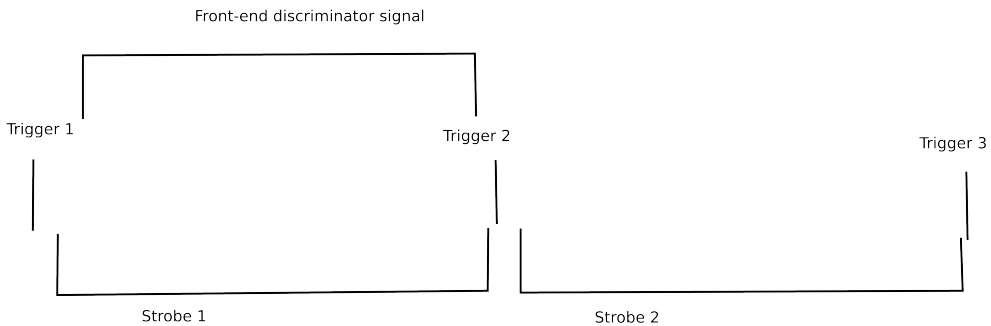
Figure 5.6: Signal from front-end being latched onto one strobe. Here the front-end discriminator length represents the total time-over threshold for all pixels firing.
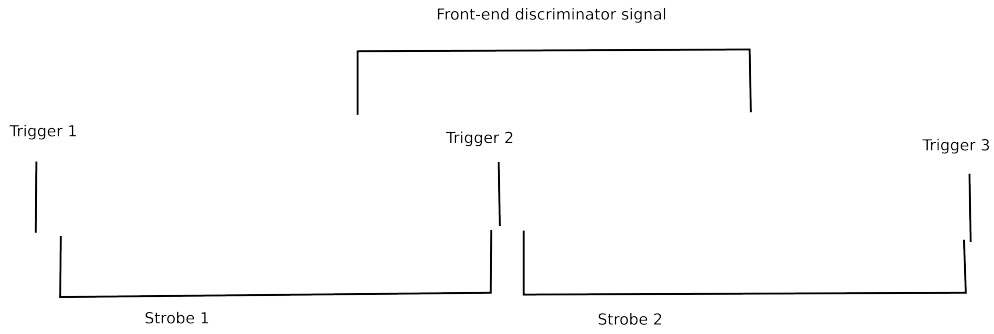
Figure 5.7: Signal from front-end being latched onto two different strobes. Here the front-end discriminator length represents the total time-over threshold for all pixels firing.
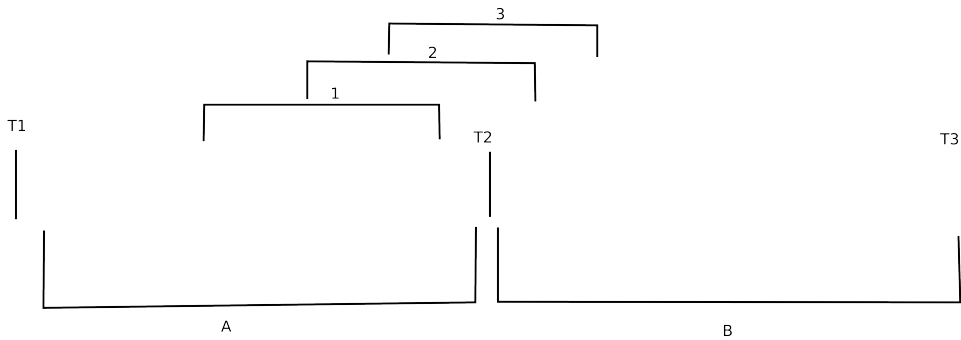
Figure 5.8: 1: Signal from front-end from pixel nr 1, 2: Signal from front-end from pixel nr 2, 3: Signal from front-end from pixel nr 3, T1: Trigger nr 1, T2: Trigger nr 2, T3: Trigger nr 3, A: Strobe nr 1, issued by T1, B: Strobe nr 2, issued by T2.
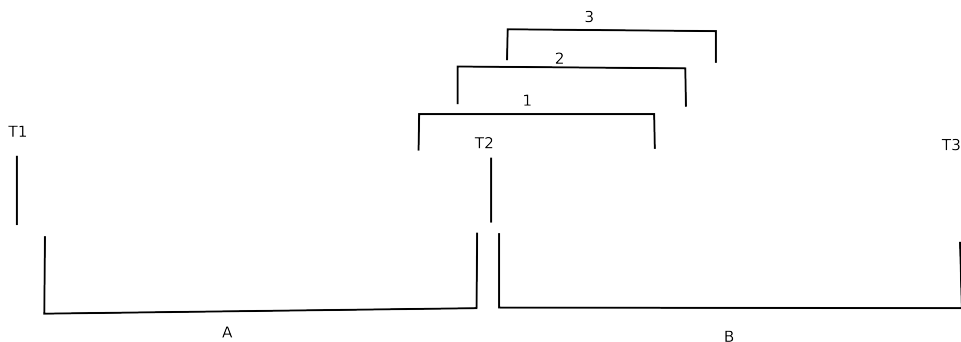
Figure 5.9: 1: Signal from front-end from pixel nr 1, 2: Signal from front-end from pixel nr 2, 3: Signal from front-end from pixel nr 3, T1: Trigger nr 1, T2: Trigger nr 2, T3: Trigger nr 3, A: Strobe nr 1, issued by T1, B: Strobe nr 2, issued by T2.

5.3.3 Dependence on pixel geometry

The ALPIDE has in previous characterizations with π shown a dependence on position, in terms of where the charge cloud is produced by the incoming particle. If the charge cloud is unable to diffuse, it will produce a small cluster. When the charge cloud is produced in the center of the pixel, then the depletion region produced by the diode will cover the complete area of the charge cloud, and small clusters are observed. When the incoming particle is hitting at the edge of a pixel, the charge will be shared between different pixels. When the front-end signal is over threshold for these pixels, they will register it as a hit, and the cluster will increase in size [36]. Ongoing work at the University of Bergen has also shown similar indications of position dependency for the cluster size.
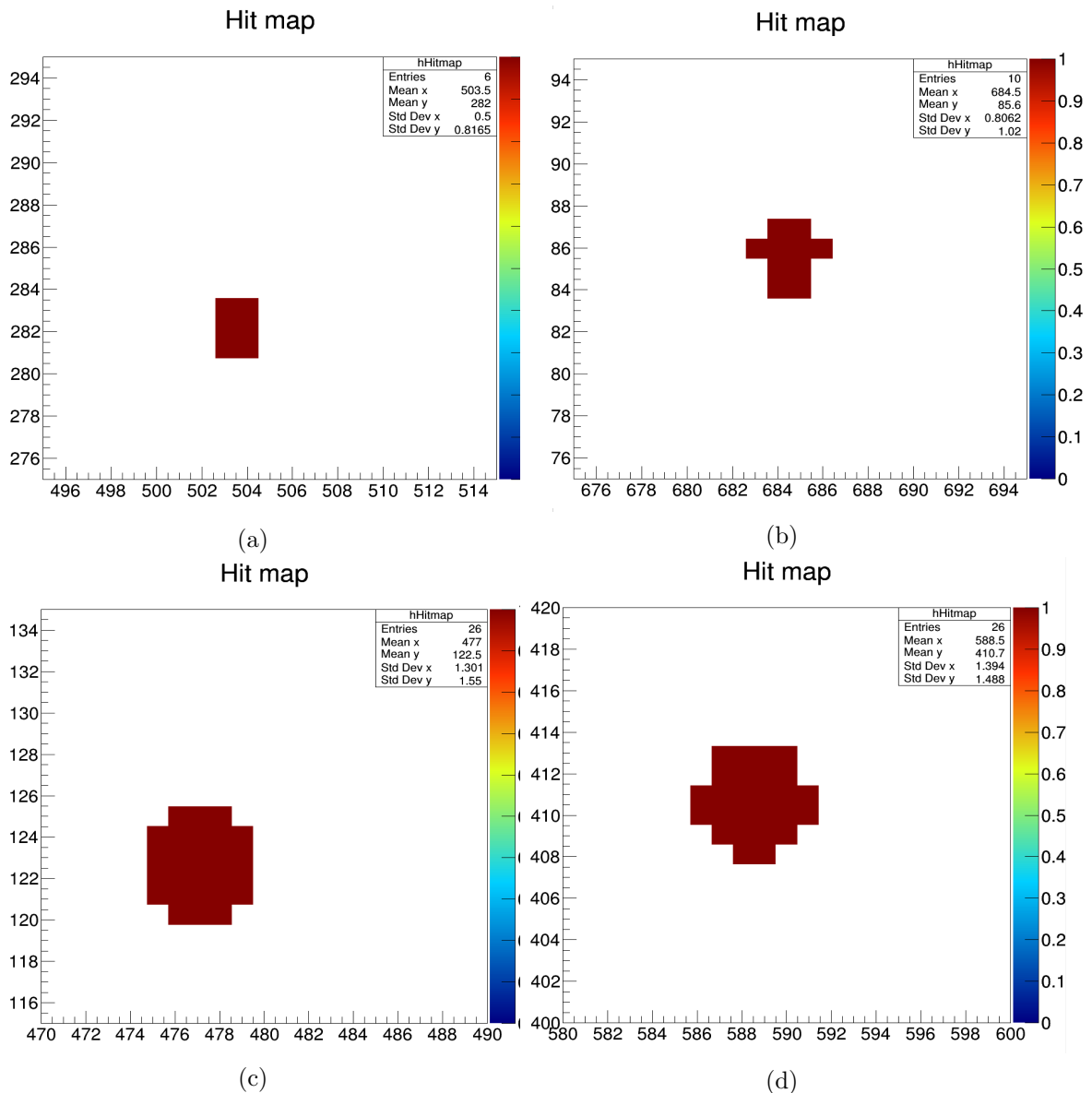
Figure 5.10: Cluster size at maximum of four different protons. $V_{BB} = 0V$, $I_{thr} = 50$ DAC.

In Fig 5.10 the cluster formation of four different particles can be observed. All parameters are the same during the measurements, and they were taken in the plateau before the Bragg peak, so the energy deposition should be equal for all particles. The charge cloud created

by the incoming alpha particle exceeds the depletion region of the diode, so the cluster size will always have an extension larger than one pixel for a reverse bias voltage of 0V. The position of impact, of the incoming particle with the ALPIDE, with respect to the position of the diodes, will determine how the cluster size and shape forms.

5.3.4 Time over threshold

The time-over threshold for the front-end discriminator pulse determines if the pixel registers a hit or not. The time over threshold can be measured by injecting a charge using the internal generation of a charge and looking at the response from the pixel. When this method is applied, the STROBE duration is set at a constant length, while the strobe delay is incremented in steps of 500 ns. For a STROBE duration which is kept constant at 500 ns, while the trigger rate is set at 100 kHz, the time over threshold is measured.

Figure 5.11: Hit ratio for induced charge as a function of strobe delay for four different pixels

48

Figure 5.12: Peak of 100% hit ratio as a function of strobe delay and induced charge of four different pixels

By changing the strobe delay it is possible to observe the threshold of the pixel. This is where you start to see the signal from the front-end, and also the duration of the signal can be observed. For each charge settings, 50 injections are sent to the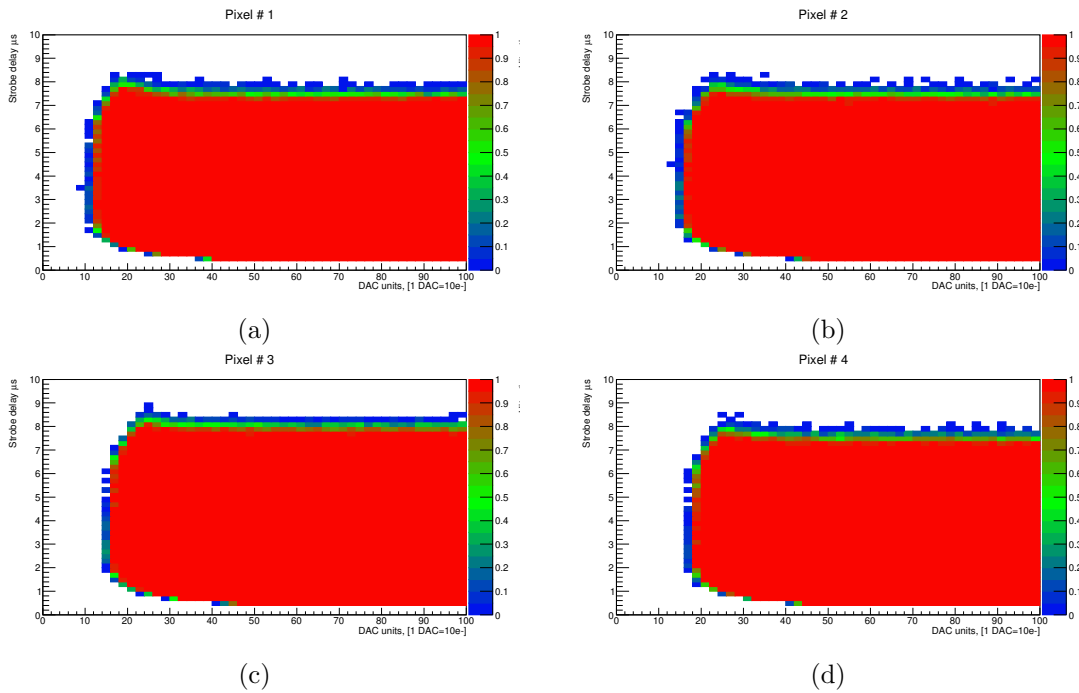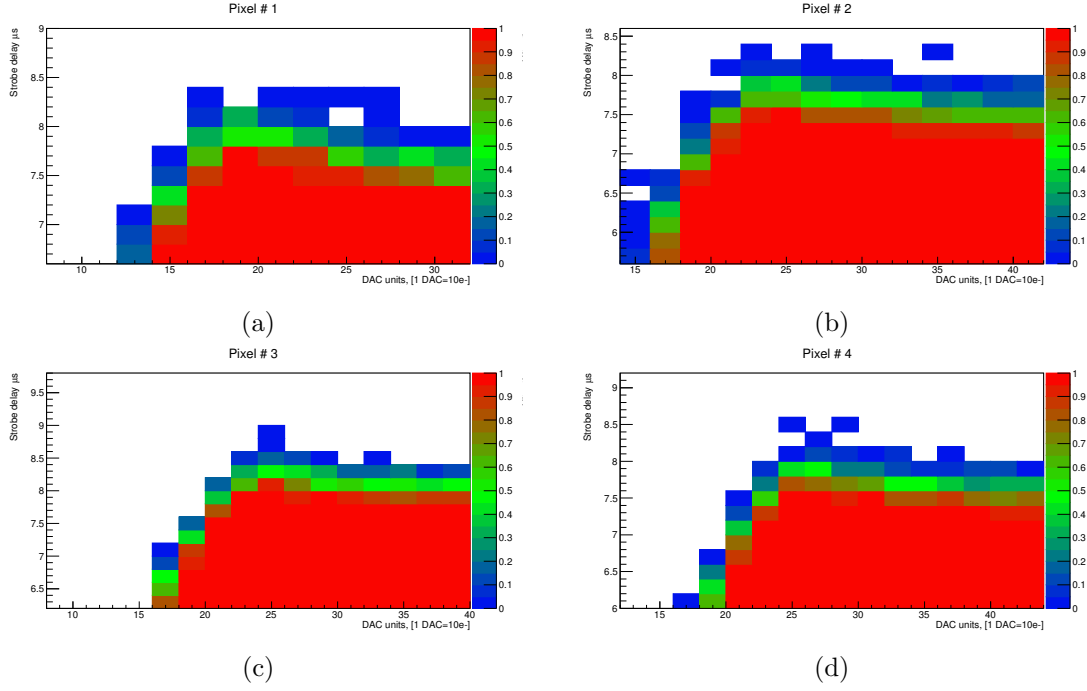 ALPIDE, and the ratio of these injections that are latched on to the STROBE signal gives the hit response of a pixel for a given charge. Given that there are variations in the threshold of chips, the starting point of charge collection and the peak position should vary. This is indeed what can be observed in Fig 5.11. The thresholds for the different pixels can be seen to vary from 10-20 DAC units. This change in threshold also shifts where the peak for the time-over threshold is. The time-over threshold can be read as the vertical distance for a given charge where there is a 100% response from the chip. The maximum time-over threshold can be seen to be ≈ 8 μs, before it reaches a saturation point. This indicates that there is a clipping mechanism of the front-end signal if the charge is high enough. The ALPIDE has a limit to the charge injection of 1.8V, this corresponds to $\approx$ three MIP particles. Since the ALPIDE was designed for MIP particles, it is expected that there are variations in the time-over threshold for charges which emulates these particles. For particles which produce a charge that surpasses this, the information provided by the time-over threshold can not be used to determine the charge which is produced by the traversing particle, due to the clipping of the signal. Thus all of these will have the same time over threshold.

The time over threshold for heavy charged particles is still useful as it can give an idea of how long a charge stays in the system. This will affect how many hits the ALPIDE sees in a frame for a given particle rate.

To perform studies of the time-over threshold for non MIP particles, another technique has to be deployed. For these measurements the technique were to increase the trigger rate to 1 MHz, while the strobe duration were set at 750 ns to avoid the extension of the strobe signal. The front-end signal will then extend over several STROBE windows, and the number of consecutive STROBE windows will determine the time over threshold. Fig 5.13 shows the time-over threshold measurements for an alpha particle produced from an ^{241}Am source, producing alphas with $E = 5.5$ MeV at a particle rate of 3 kHz.
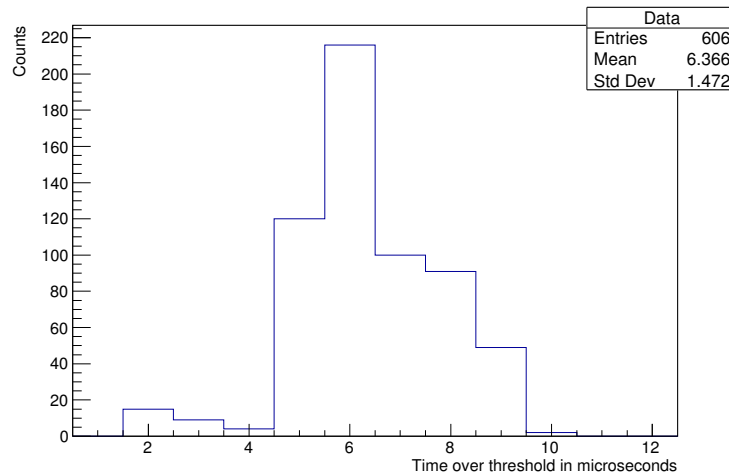
Figure 5.13: Time over threshold for alpha clusters. Trigger rate 1MHz, Strobe duration 750 ns, $V_{BB} = 0V$, $I_{thr} = 50$ DAC $V_{clip} = 0$ DAC.

The alphas produce charges which have a signal duration in the range of 5-10 μs, with a peak at 6μs. This is lower than the time-over threshold for a typical MIP particle with the same settings.

Clipping

The test were performed by inducing 50 charges into the pixels with a step size of 2 DAC units. The STROBE duration was set at 10 ns, while the delay of the STROBE signal was varied in steps of $n \times 200$ ns. The V_{clip} configuration of the ALPIDE was varied between the measurements to see the effect this has on the pulse shape. The clipping mechanism of the ALPIDE is controlled by the clipping transistor M6 (see section 4.5).
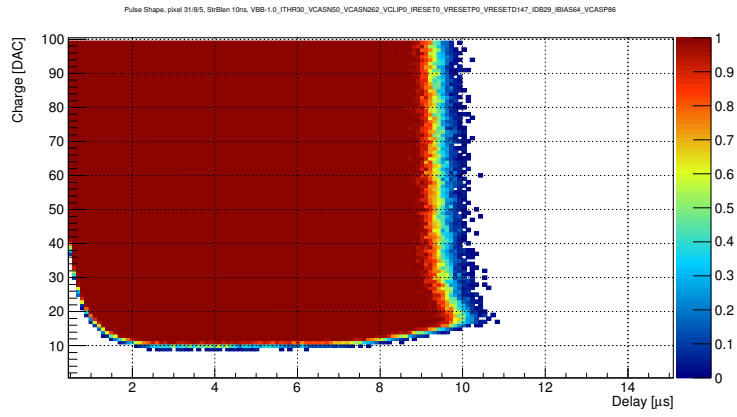
Figure 5.14: $V_{bb} = 0$V, $V_{clip} = 0$, $I_{thr} = 30$
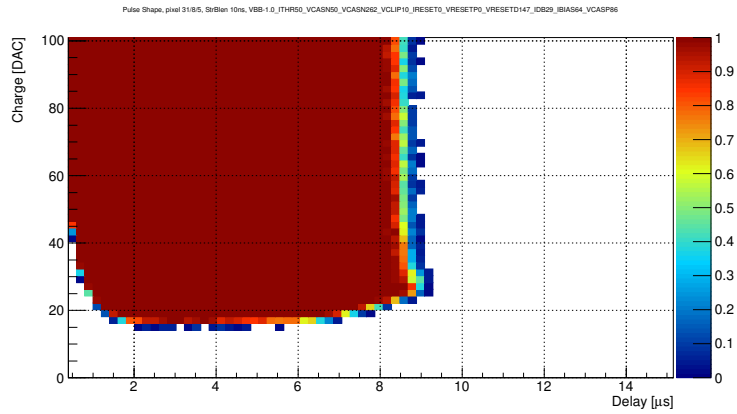
Figure 5.15: $V_{bb} = 0$V, $V_{clip} = 10$, $I_{thr} = 50$
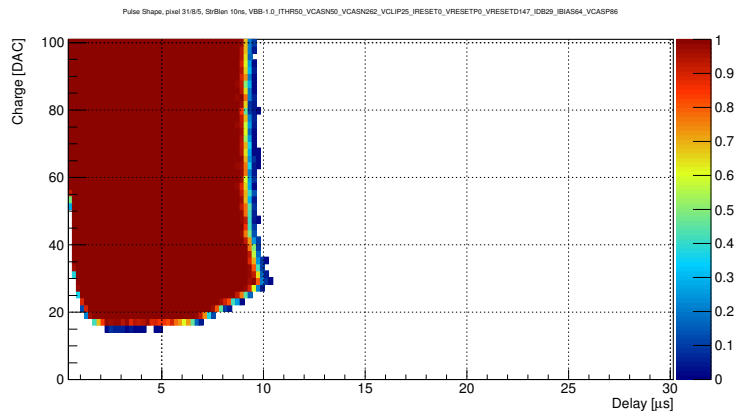
Figure 5.16: $V_{bb} = 0$V, $V_{clip} = 25$, $I_{thr} = 50$

51
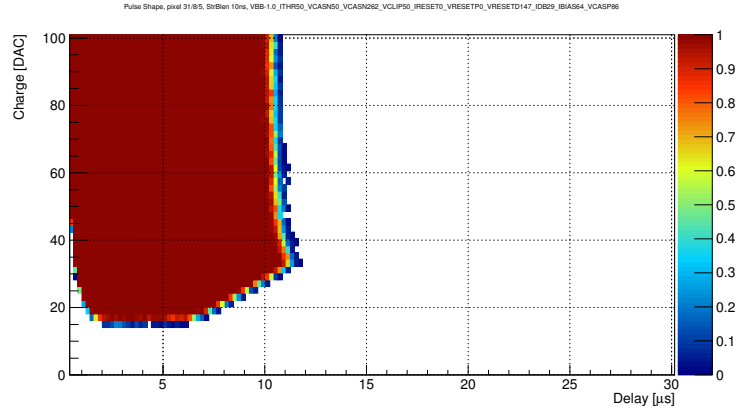
Figure 5.17: $V_{bb} = 0V$, $V_{clip} = 50$, $I_{thr} = 50$
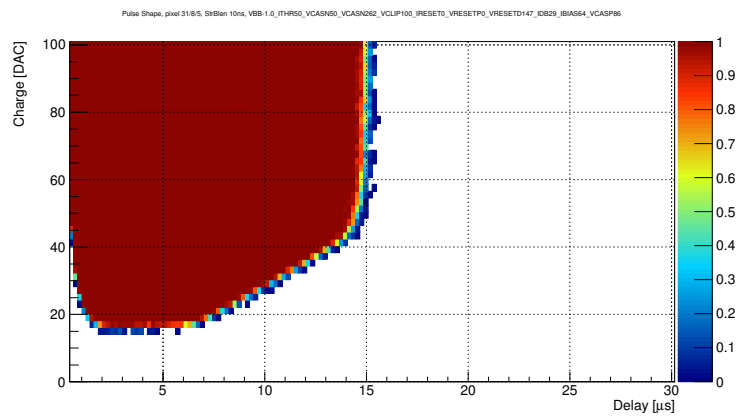
Figure 5.18: $V_{bb} = 0V$, $V_{clip} = 100$, $I_{thr} = 50$
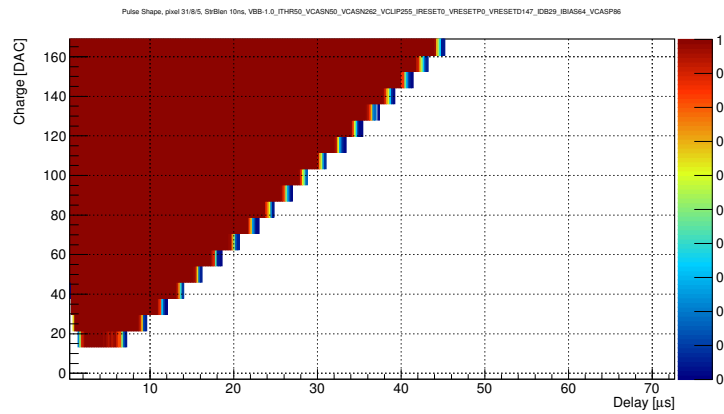
Figure 5.19: $V_{bb} = 0V$, $V_{clip} = 255$, $I_{thr} = 50$

Increasing the V_{clip} setting allows for a longer time-over threshold for a given charge. Where the clipping sets in can be manipulated by the user. The higher the V_{clip} setting is set, the longer the time over threshold for the signal. The maximum setting of the V_{clip} is at 255 DAC units, since there is a 8 bit ADC. The region where it is possible to distinguish two particles, with different energy deposition in the epitaxial layer, also increases. In Fig 5.15 this region is between 15 and 25 DAC units, while in Fig 5.18 this has increased to

include the values between 15 and 50 DAC units. For measurement Fig 5.19 the V_{clip} is set at the maximum value. Particles in the energy range 20-165 DAC are distinguishable. By optimizing this parameter to the particle in question, this could be a better way to track the energy deposition of a particle, rather then using the cluster size, as it may vary with position of impact. However, this would depend on the particle rate. If the particle rate is sufficiently high enough, multiple particles will trigger the same pixel several times, and no information can be taken from the time over threshold or cluster size of the particle.

Chapter 6

OCL-Oslo Cyclotron Lab

The experiment was carried out at the Oslo Cyclotron Lab (OCL) in November 2017. If the ALPIDE is to be used in a pCT, it is a necessity for it to be enabled as both a tracking detector and a calorimeter in the pCT being developed by the Department of Physics and Technology. The test was performed by keeping a constant beam energy and then varying the distance between the ALPIDE and the beam entry.

The purpose of the OCL beam test was to see if the ALPIDE would be able to measure $\frac{dE}{dx}$ effectively. This was done by looking at the energy deposition of the protons at different distances and how the detector performed with different reverse BIAS voltages.

6.1 Experimental setup

The experiment was conducted by running the ALPIDE in external trigger mode, with a trigger rate of 100 kHz. The proton beam energy was set to 16 MeV, with a measured beam current of 20 nA. The spot size was measured to be 1 cm by using a film. See Fig 6.3.

A tungsten scattering filter was applied onto the beam cap to spread the beam. This was done to reduce the number of hits per frame in order to avoid the issuing of a BUSY signal, while getting high enough statistics at larger angles. By moving out of the beam, the ratio of multiple hits per time frame significantly drop. The beam flux at 0° angle was in the range $10^6 - 10^7 \ protons/cm^2s$, and the beam current was measured to be 2 nA at the Faraday cup present on the rail. This was done to ensure a steady particle flux for the measurements. During the measurements the particle flux may vary slightly, but for measurements of cluster size and shape this fluctuation was negligible.

The ALPIDE was mounted to a T-structure next to a 3DMiMiC detector as two different experiments were carried out simultaneously. The schematic of the setup can be seen in Fig 6.1.
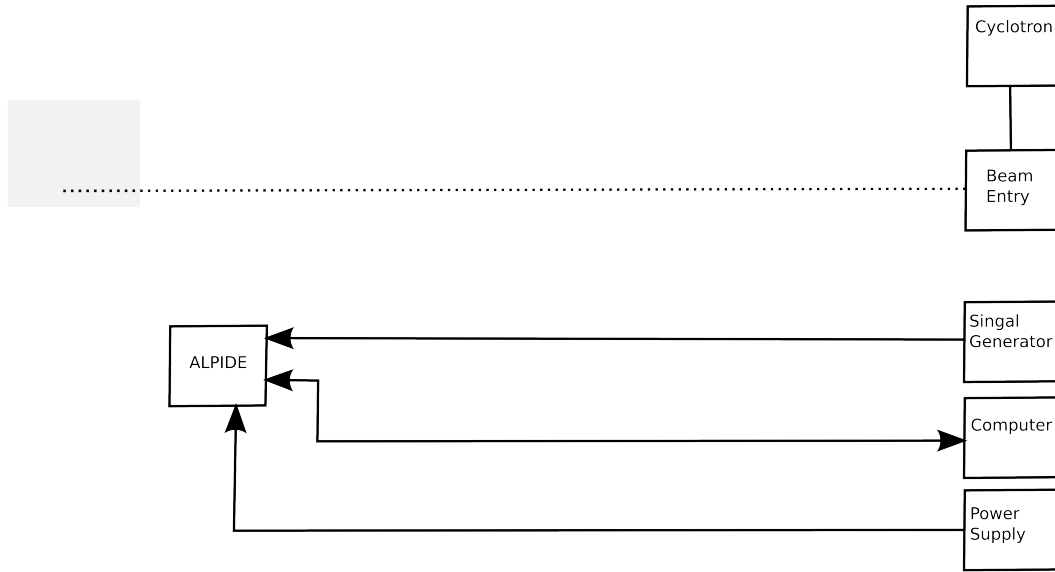
Figure 6.1: Experimental setup at OCL

Before going to Oslo, simulations had been done for a 11 MeV beam energy. Since this energy could not be provided, it was decided to start the measurements at a distance which would ensure us to be behind the Bragg-peak and then simulate the beam properties after the experiment. The 3DMiMiC detector was used to estimate the beam range on sight. The data was acquired over 3 days.
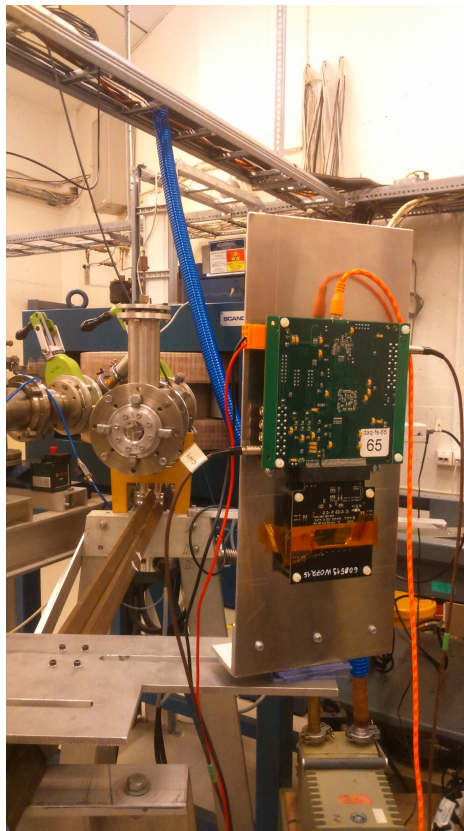
Figure 6.2: Experimental setup

Figure 6.3: Size of beam spot

6.2 Trigger system

The ALPIDE has two different triggering systems. One with an internal trigger and one with an external trigger. For the measurements taken at the OCL, the external trigger mode was used. A closer explanation of the trigger system can be found in section 4.3.3.

Using the external triggering allows a wider range of triggering possibilities, so that the trigger may be matched up with the time-over threshold (TOT) for the signal that is produced by the protons. With protons producing a TOT signal width of approximately 5-10μs a trigger rate of 100 kHz with a STROBE duration of 9.75 μs was chosen [33].

The triggers were bundled up in trains consisting of 1000 triggers per train. After each train there is a 100 ms window to allow the ALPIDE to read out and transmit the data. The number of trains in one measurement can be varied to acquire the sufficient statistics.

6.3 Cluster size and shape

When the proton traverses the ALPIDE, it generates a charge in the epitaxial layer. The shape and size of the cluster is determined by how the charge diffuses in the epitaxial layer. A cluster can be defined as the number of pixels that are firing as a result of one incident particle hitting the detector. A typical cluster can be seen in Fig 6.4.
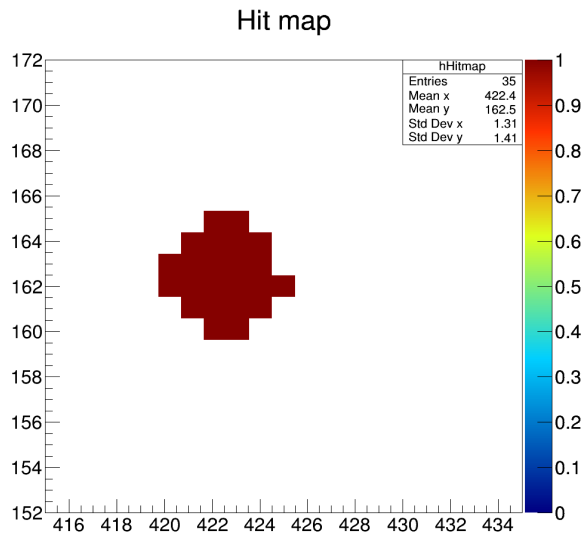
Figure 6.4: Typical cluster for $V_{bb} = 0$V

6.3.1 Influence of reverse BIAS voltage

As can be seen in section 5.3.1, the reverse BIAS voltage has an effect on how the cluster forms. The depletion region increases as the reverse BIAS voltage is applied to the ALPIDE. When the depletion region is large, the charge carriers in the epitaxial layer are quickly collected and have a smaller volume to drift in. An illustration of the depletion region on individual pixels can be seen in Fig 6.5.
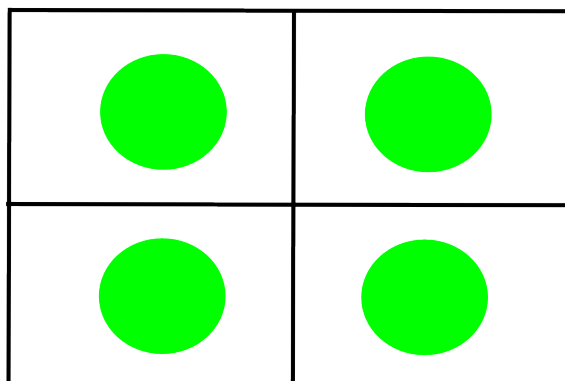
Figure 6.5: Depletion region of different pixels. The green area represents the area of the depletion region for a given reverse bias voltage, while the lines define the pixel area.

This leads to a dependence on the position of impact for the particles hitting the ALPIDE. When the particle traverses the epitaxial layer, it will produce electron-hole pairs. If the trajectory of the particle is outside of the depletion region, it will allow for the charge carriers to drift. If the reverse bias voltage is set at 0 V, then the only voltage present in the epitaxial layer is that which is created by the p-n junction. Thus if a particle has a trajectory which does not take it through the depletion region, it will create charge carriers which are able to drift to several pixels. The charge carriers will undergo mainly Coulomb scatterings, until they eventually drift into the depletion region of one of the pixels. This will increase the likelihood of the charge being spread between several pixels. If the trajectory of the incident particle is through the depletion region, then the charge carriers which are produced inside the depletion region will not be able to escape. As the particle moves out of the depletion region, the charge carriers which it produces are able to drift again. The effect of this is that the size of the cluster will be smaller compared to the particles which have a trajectory that do not take them through the depletion region. Since the volume of the depletion region is dependent on the reverse bias voltage, this will affect the cluster size and shape.
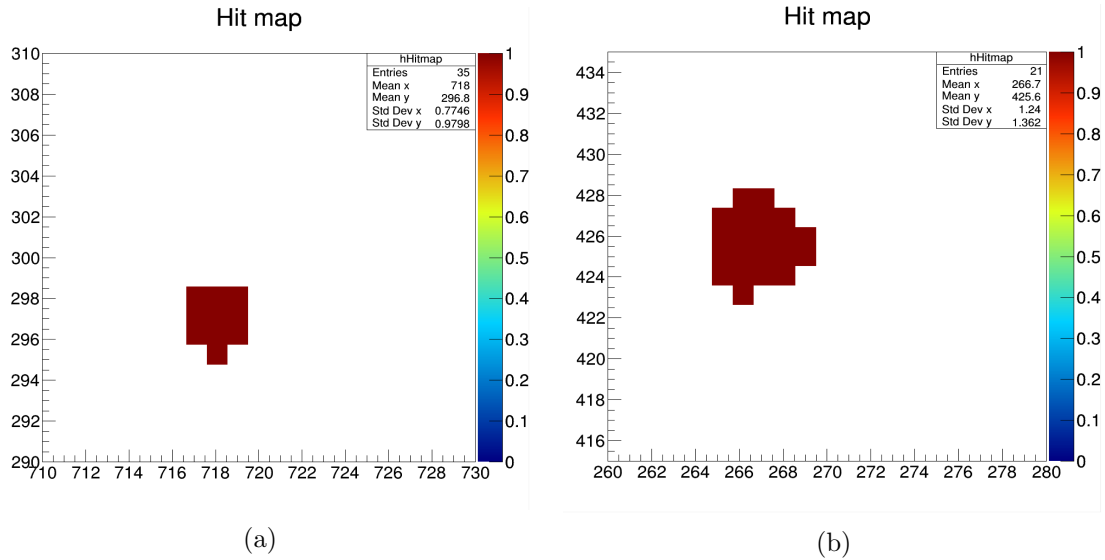
Figure 6.6: Two different cluster sizes with the parameters being equal. $V_{bb} = 0V$.
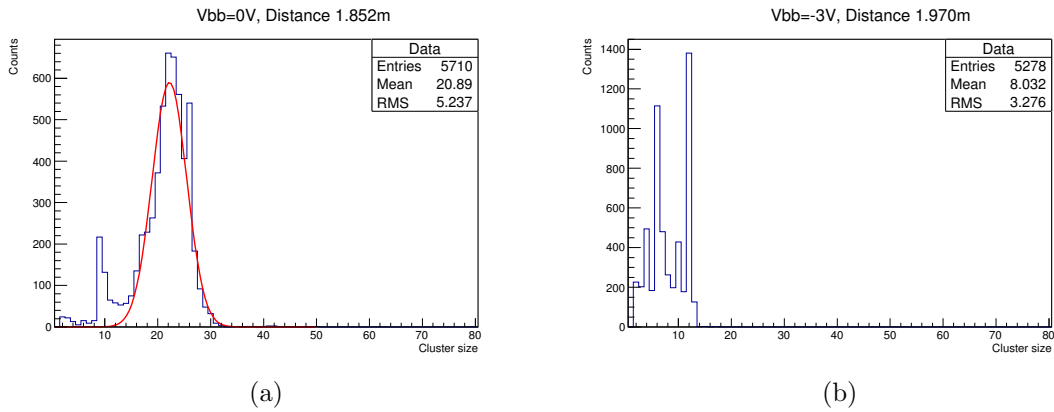
Figure 6.7: Cluster size distribution for measurements performed with reverse biases of -3V and 0V

As can be observed in Fig 6.7a and 6.7b, two distinct peaks appear. One around 10 in cluster size and the other at 22 for the 0V measurement. At a reverse bias voltage of 0V the depletion region is small compared to the pixel area, allowing a larger percentage of the charge carriers to drift in the epitaxial layer. This in turn leads to the charge being spread among several pixels. Therefore it is expected that the peak which has the larger cluster sizes has more counts than that which has the smaller ones. For the -3V measurement, the peaks shift to the left as the cluster size in general decreases when a reverse bias voltage is applied. The peak containing the smaller clusters also increases as a larger percentage of the traversing protons will have a trajectory through the depletion region.

6.3.2   Time over threshold dependence

Given the trigger ratio of the measurements, the time over threshold for protons can be estimated by:

$$\text{Time over Threshold} = \frac{\text{Consecutive events}}{\text{Consecutive events} + \text{Single events}} \times \text{Trigger period} \qquad (6.1)$$

Given a trigger period of 10 μs and $V_{clip} = 60$, then the signal produced by a proton is not able to be latched onto three different strobes. Hence only the ratio of particles latching their signal onto two different strobes or one strobe have to be accounted for.
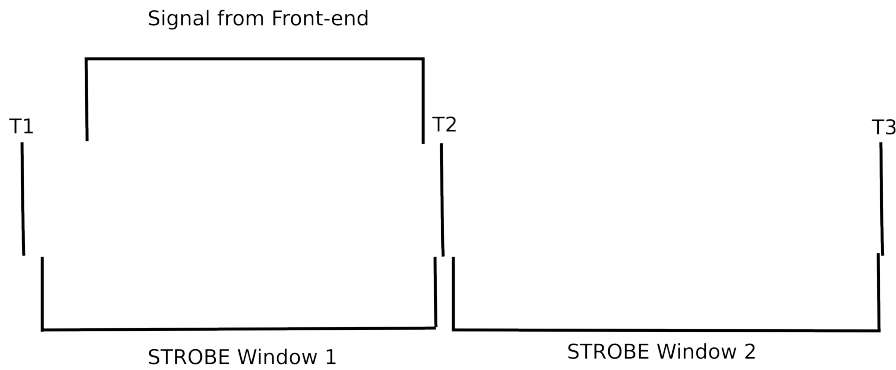
Figure 6.8: Signal from front-end discriminator being latched onto one STROBE signal
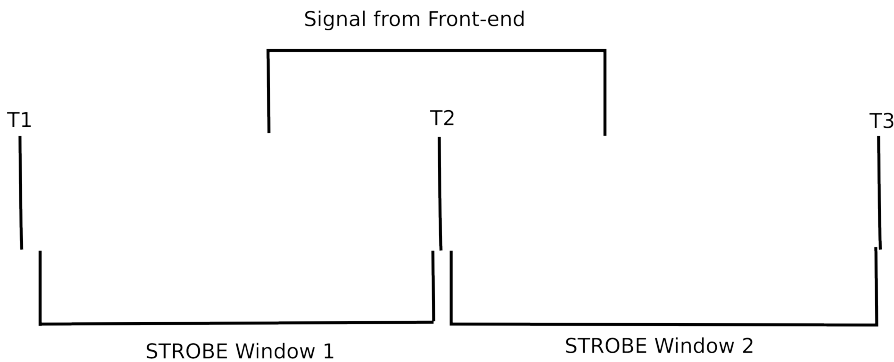
Figure 6.9: Signal from front-end discriminator being latched onto two different STROBE signals

If the time-over threshold is similar for all of the particles, then the only varying factor is the arrival time of the signal from the front-end discriminator. The ratio of events happening consecutively, i.e. the same particle firing in two STROBE windows after each other, is then an indicator of the time-over threshold for the particles, given that the particle rate is small so that two particles will not hit the detector simultaneously.
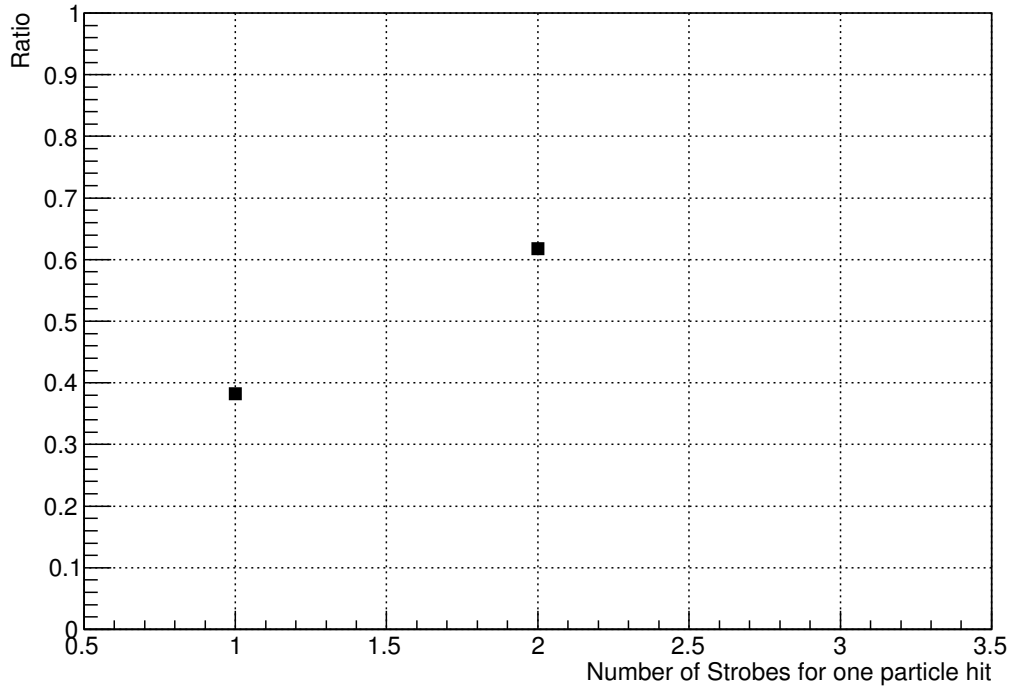
Figure 6.10: The ratio of STROBE windows which the signal is latched onto per proton. $V_{bb} = -3V$, $I_{thr} = 50$, $V_{clip} = 60$

Using 6.1 then the time-over threshold can be estimated to be 6.3 μs for protons with a reverse bias of -3 V.

6.4   Bragg curve measurements

By measuring the energy deposited by the proton beam traversing the patient, it is possible to create a 3D image of the body[25]. To do this, the ALPIDE must operate as a both a tracking detector and effectively measure $\frac{dE}{dx}$. The tracking is to be done by placing the ALPIDEs in a telescope formation, while the energy deposition is done by looking at how many layers the particle penetrates, as well as the clusters it generates in the different layers. By doing measurements at different distances from the beam entry, the LET should change as the protons traverse the ALPIDE. This will give an indication of how the pCT would work if the ALPIDE is stacked up in several layers. For these measurements, reverse biases of 0V and -3V were used.

6.4.1　0V reverse BIAS measurements

To perform the measurements the ALPIDE was placed far away from the beam entry. The 3DMIMIC detector next to it is a LET detector and could determine when the ALPIDE entered the beam. 15 measurements were carried out by moving the ALPIDE closer to the beam entry, while keeping the variation in angle as small as possible. The configuration of the ALPIDE is listed in table 6.1.

Table 6.1	ALPIDE settings during measurements
V_{bb}	0V
I_{thr}	50 DAC
V_{casn}	50 DAC
V_{cans2}	62 DAC
V_{clip}	0 DAC
V_{resetd}	147 DAC
Strobe duration	$9.75\mu s$
Trigger rate	100 kHz
Angle	19^0-28^0

6.4.2　-3V reverse BIAS measurement

The same procedure was applied for the measurements done with a reverse bias voltage of -3 V. A total of 16 measurements were carried out. The ALPIDE configurations are listed in table 6.2.

Table 6.2	ALPIDE settings during measurements
V_{bb}	-3V
I_{thr}	50 DAC
V_{casn}	105 DAC
V_{cans2}	117 DAC
V_{clip}	60 DAC
V_{resetd}	170 DAC
Strobe duration	$9.75\mu s$
Trigger rate	100 kHz
Angle	26^0-34^0

6.4.3　Data analysis

The ALPIDE provides data where one has information about the position and timing. Every hit has a time stamp from when it was read out by the priority encoder, and because of how the priority encoder works, it is also sorted in x position. A further explanation of the priority encoder and data readout can be seen in section 4.3.2. The cluster finder locates pixels which have registered a hit close to each other, if the hit appears inside the same STROBE. For events which have been latched onto two different STROBEs, the smallest cluster has been filtered out. This is possible since the time-over threshold for a signal from the front-end discriminator exceeds the drift time of the charge carriers in the epitaxial layer, ensuring that all of the pixel hits are recorded in at least one of the two STROBEs. The smallest cluster is either donut shaped, if the charge in the center has reached is maximum time-over threshold when the second STROBE arrives, or it is missing its edges if the charge carriers has not reached the outer most pixels when the first STROBE is read out. Examples can be seen in Fig 6.11.

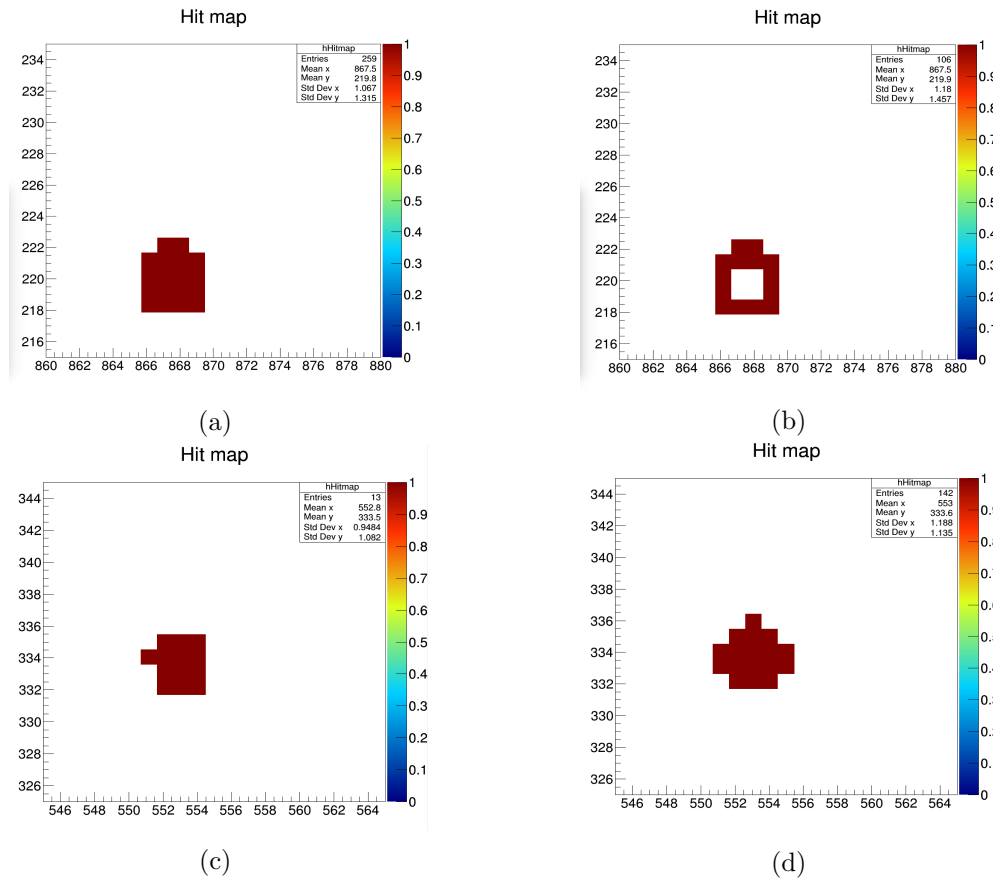Figure 6.11: Development of cluster shapes with time. Strobe duration = 9.75 μs with a trigger rate of 10 MHz. (a) & (b) is one proton latching onto two different STROBEs, where the signal from the front-end have arrived early and the center disappears for the second strobe. (c) and (d) is the same proton being latched onto two strobes, where the cluster continuous to grow between the readouts.

6.4.4 Results

0V reverse BIAS
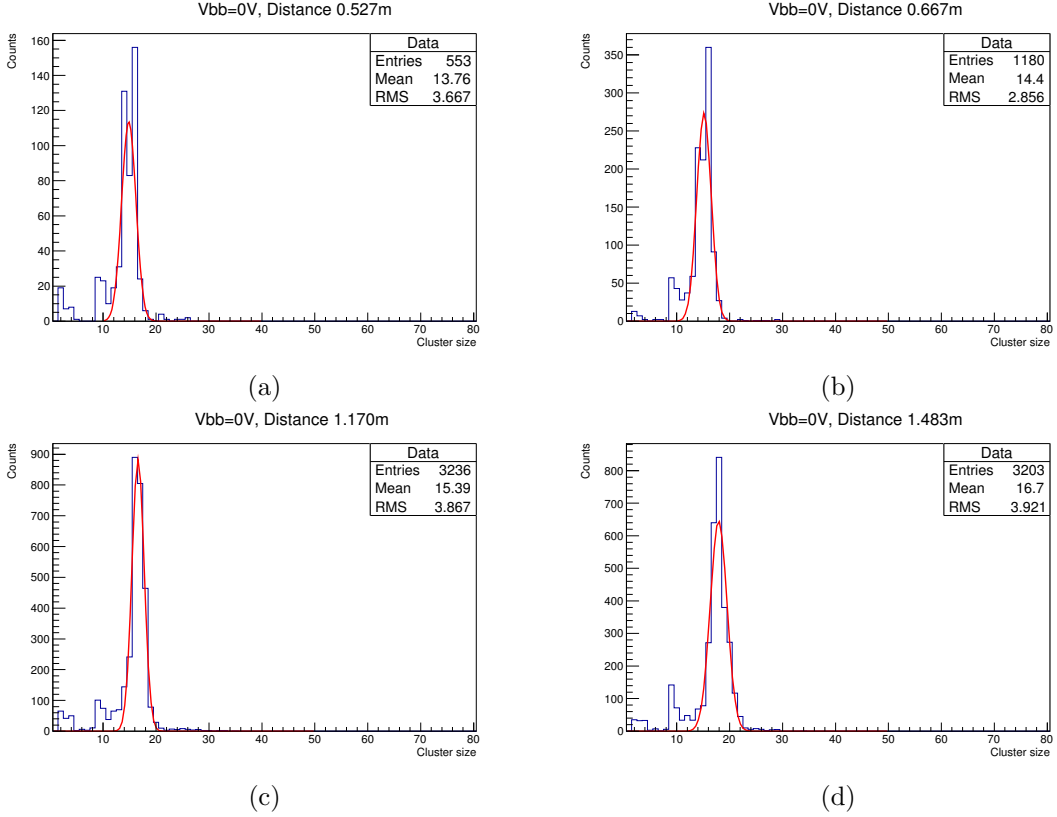
Figure 6.12: Average cluster size for four different measurements with protons, increasing in range from the beam entry.

For the measurements performed in (a) and (b) in Fig 6.12, it can be observed that the average cluster has a slight increase with the increase in distance. The spread of the cluster sizes are narrow, which indicates that the LET of the proton beam is fairly constant (see Fig 2.4). Measurement (a) has two peaks close to each other, according to [36], the ALPIDE will have some cluster formations which are more likely than others. Thus the geometry prefers clusters of size 14 and 16 rather than 15. The small rise at around 10 in cluster size stems from the position dependency of the incoming particle, which is discussed in detail in 6.3.1. The smaller cluster sizes in the range 0-5, is the size which is expected from the background as can be seen in Fig 6.22.

For the measurements performed in Fig 6.12, the average cluster size increases slightly with the distance. The spread of the peaks also widens, indicating that the LET starts to vary among the protons, due to some of the protons undergoing more interactions before the impact with the ALPIDE.

64

Figure 6.13: Average cluster size for four different measurements done at a range close to the end of the beam range.

For (a) in 6.13 the peak is at 22 in cluster size, before it drops down a bit at 23 and then rises again at 24. This indicates the preference of having clusters with even number of pixels as was observed in Fig 6.12. The peak around 10 still exists indicating that this is the cluster size most common if the particle traverses the depletion region of the pixel. Measurement (b) has a peak at 22 in cluster size and the same small peak at 10. Measurement (c) and (d) has a widened peak, indicating that the ΔLET increases. A preferred cluster size of 26 starts to appear in both.
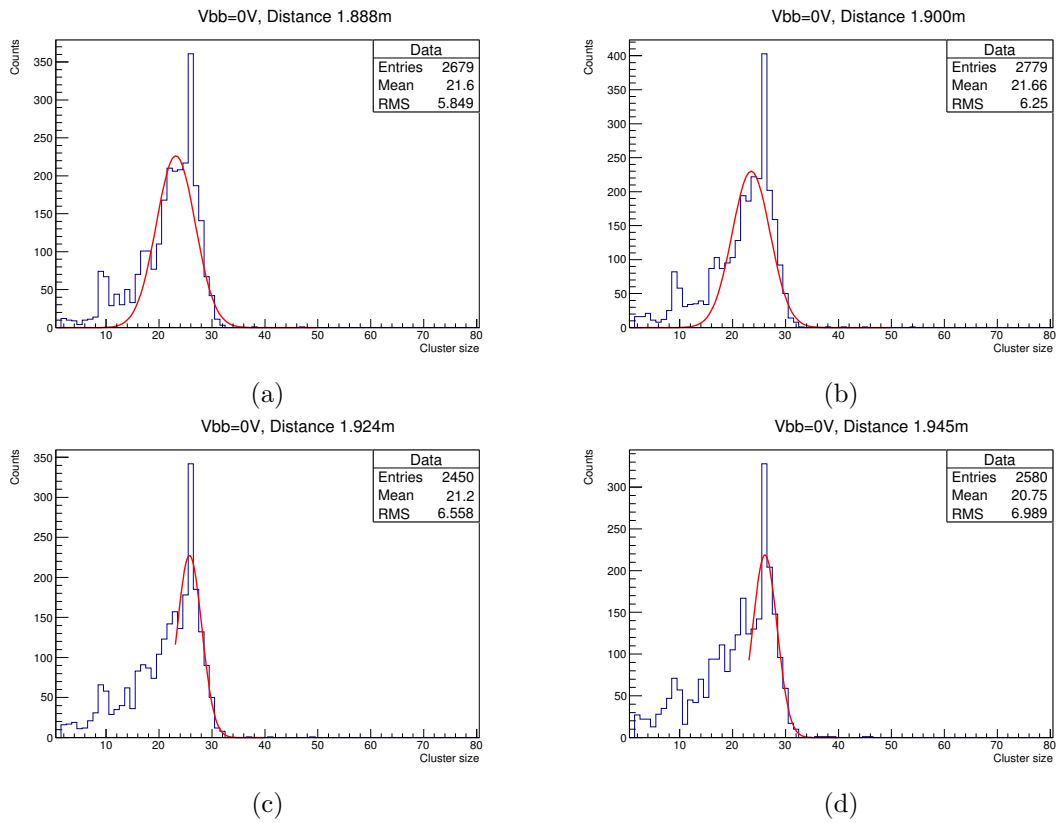
Figure 6.14: Average cluster sizes for four different measurements performed close to the end of the beam range.

For all in Fig 6.14 the cluster size of 26 is the most preferable, the same could be observed in (c) (d) in 6.13. The range of cluster sizes also increases with the distance from the beam entry.

66

(a)

(b)

(c)
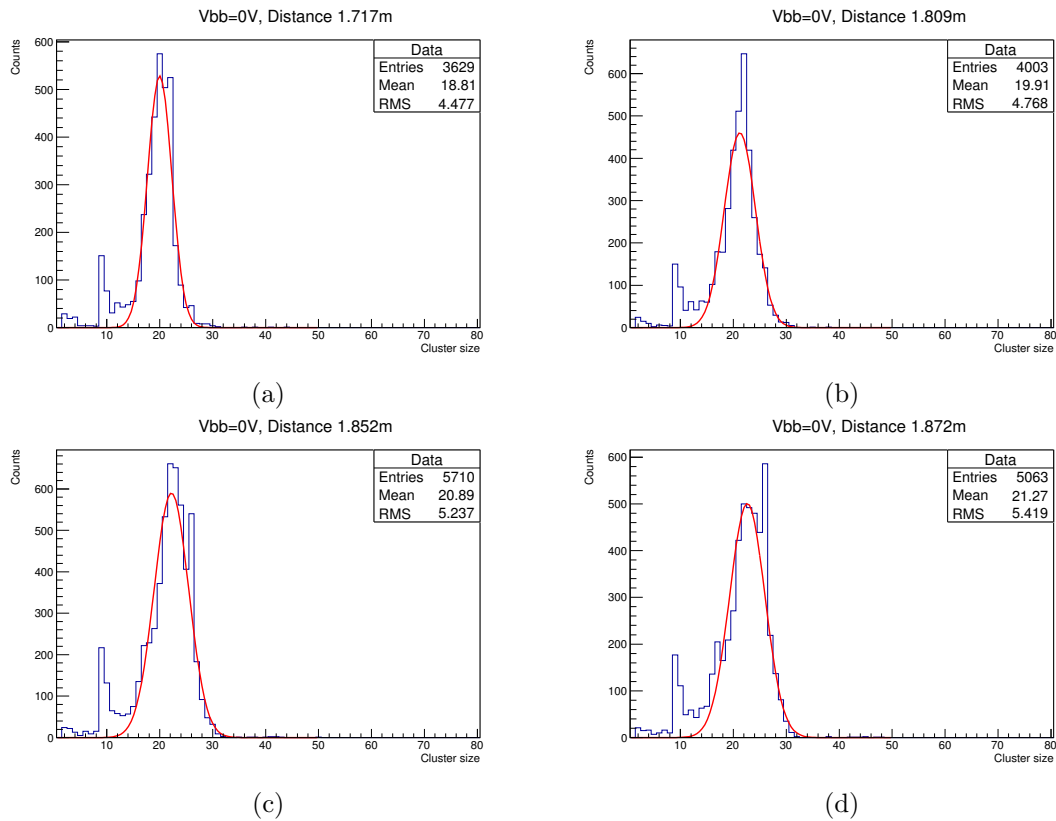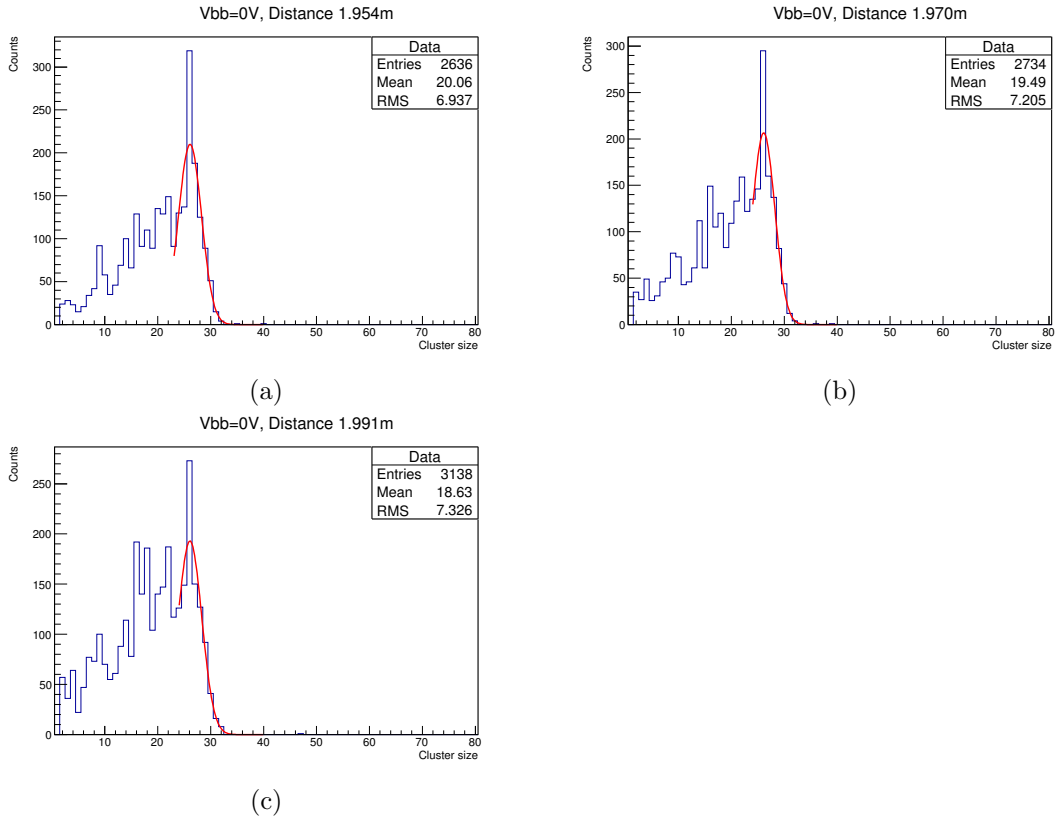
Figure 6.15: Average cluster sizes for four different measurements done close to the end of the beam range.

Again there is a preference of cluster size 26 in all of the measurements in Fig 6.15. The ΔLET increases with distance, and this indicates the end of the Bragg-peak.
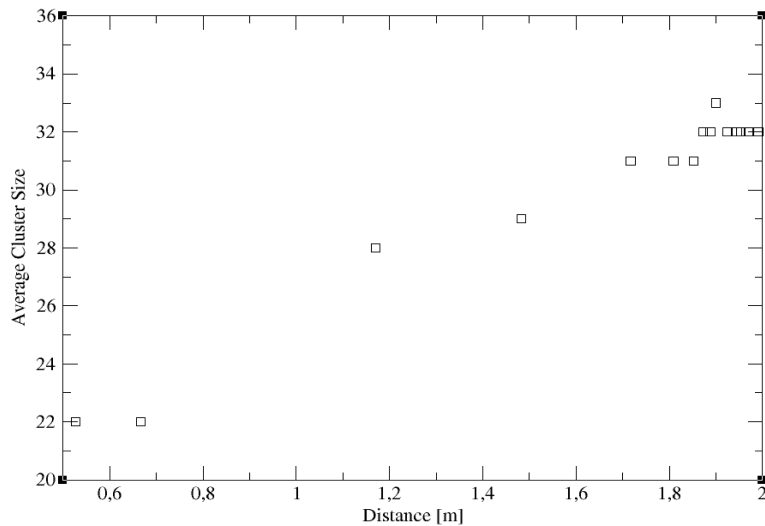
Figure 6.16: Maximum cluster size as a function of distance.

In Fig 6.16 the maximum cluster size recorded at each measurement can be observed. In the region 0.5 m to 0.8 m the maximum value sits at 22. The LET is uniform for all of the traversing particles as can be seen in Fig 6.12a and Fig 6.12b. As the ALPIDE moves

further away the maximum cluster size increases as some of the particles have slowed down enough to have a large energy deposit in the ALPIDE. This trend continuous as the distance from the beam entry increases. The maximum cluster size saturates at 32 for the measurements that were performed in the Bragg-peak region. The cluster size is dependent on the total deposited charge in the epitaxial layer. When the ALPIDE is at the end of the beam range, the LET is high, but the particles is not able to penetrate the full depth of the epitaxial layer. Because of this the total deposited charge decreases even though the LET of the particles increase.
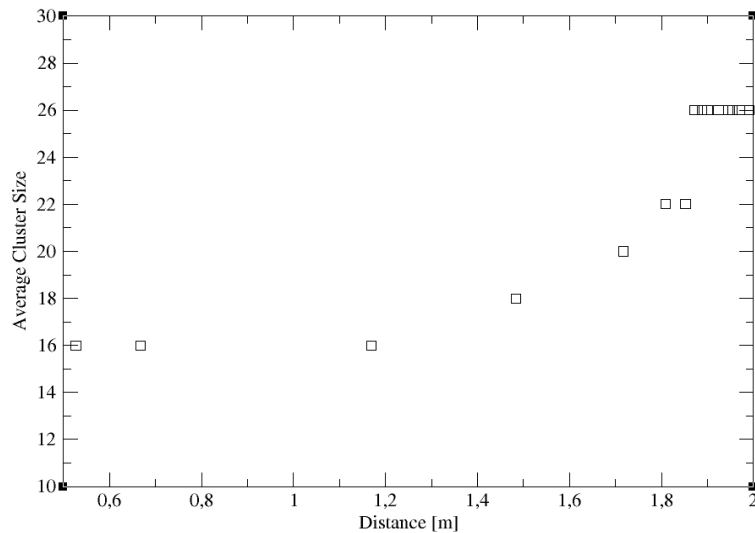
Figure 6.17: Most common cluster size as a function of distance.

In Fig 6.17 the most common cluster size at each measurement is observed. For the measurements done in the region prior to the rise of the Bragg-peak, the preferred value is 16. The cluster size of the peak then starts to increase as the ALPIDE moves closer to the end of the beam. It rises up to 18 at 1.5m and then continuous to increase in size in steps of even number until it reaches a saturation at 26. The ALPIDE clearly prefers clusters of even number due to the geometry of the pixels. The saturation region appears as the total deposited charge in the epitaxial layer saturates. Due to range straggling, the LET and penetration depth will differ among the particles, while the total deposited energy is confined. The preference in even cluster size hampers the development of the clusters, so two particles depositing different energies may create the same cluster size as long as the gap in energy deposition is not to large.
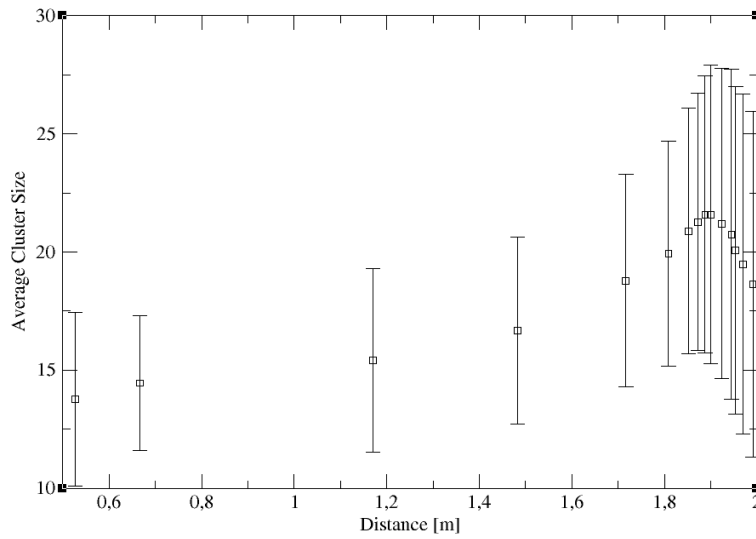
Figure 6.18: Average cluster size as a function of distance, with filtering of duplicate events.
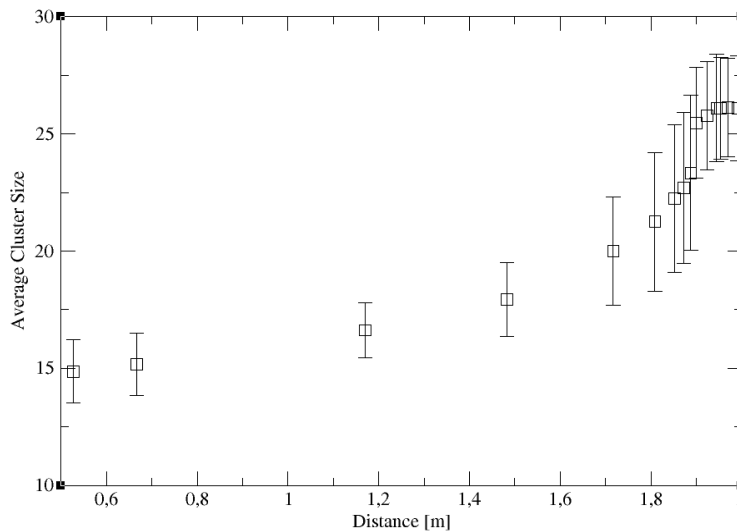
Figure 6.19: Gaussian fit as a function of distance.

The measurements of the energy deposition of protons at different distances (see Fig 6.18 and Fig 6.19) are reminiscent of the Bragg-curve. In the region between 0.5 m and 1.5 m the average cluster size stays fairly constant over a large range, which is as expected. From 1.5 m to 1.9 m the rise of the Bragg-peak can be observed as an exponential growth, replicating the behavior seen in a Bragg curve. After the maximum at 1.9 m, the cluster size shrinks. The position of the peak varies slightly between the different approaches. With the approach seen in Fig 6.18 the peak is at 1.88 m, after this point a lot of the protons are only able to create smaller clusters so the average drops. In Fig 6.19 the average value of the Gaussian distribution around the peak is observed. It has a peak in the same region as Fig 6.18 before the cluster size drops. The RMS of the measurements increases with distance. This is a result of the protons undergoing a different number of interactions, and the length traversed in the epitaxial layer will vary for the protons at

69

the end of the beam range. The measurements were also performed at an angle, so the incoming particles may have traversed different lengths through the tungsten scattering foil before they scatter. Thus the RMS increases a lot at the end.
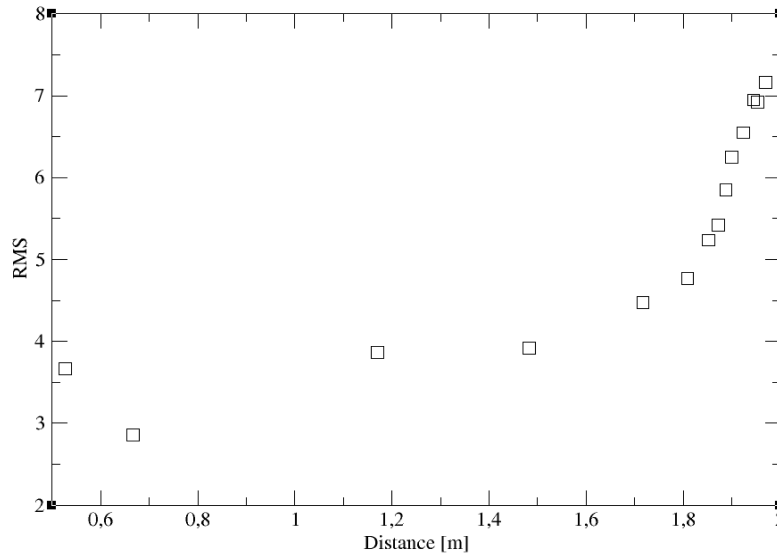
Figure 6.20: RMS as a function of of distance.

In Fig 6.20 the RMS as a function of the distance from the beam entry can be observed. The RMS is small in the region from 0.5 m to 1.5m, due to the LET of the traversing protons is fairly constant as they penetrate the ALPIDE. The incoming protons in this region have had an equal number of interactions along the way and the energy of the proton beam has not dropped sufficiently so that the protons have a large energy deposition as they traverse the ALPIDE. As the ALPIDE is moved away from the beam entry the difference in number of interactions the protons have had increases. They are then able to deposit a larger variety of energy in the ALPIDE. This leads to a higher RMS.
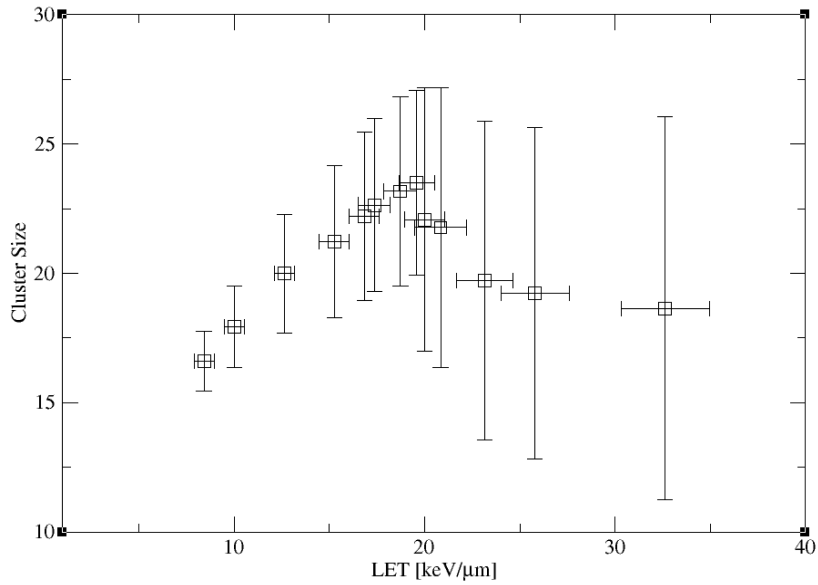
Figure 6.21: Average cluster size for measurements as a function of LET. Simulations of LET from [39]

.

The simulations were performed in GATE with 1e9 particles. The physics list in use was: QGSP_BIC_EMY.

In Fig 6.21 the relationship between the LET and the cluster size of the peaks can be observed. For cluster sizes in the region 16 to 24 the relation between them is linear, which is to be expected. When the LET reaches values of 20 [keV/μm] and above, the cluster size starts to fall of even though the LET increases. This may be due to some of the protons being unable to penetrate the full depth of the depletion layer. The number of released charge carriers drops if the proton is not able to penetrate the full depth. So even though the LET increases, the length it is able to penetrate decreases, resulting in a decrease in the cluster size.

-3V reverse BIAS
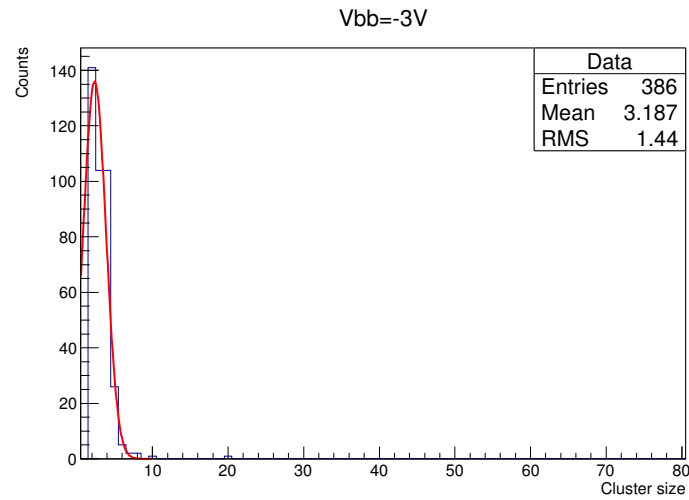
Figure 6.22: Measurement of background in experimental hall.

In Fig 6.22, the background in the experimental hall can be observed. The measurement was taken out of the range of the beam while the beam was on.

(a)

(b)

(c)

(d)
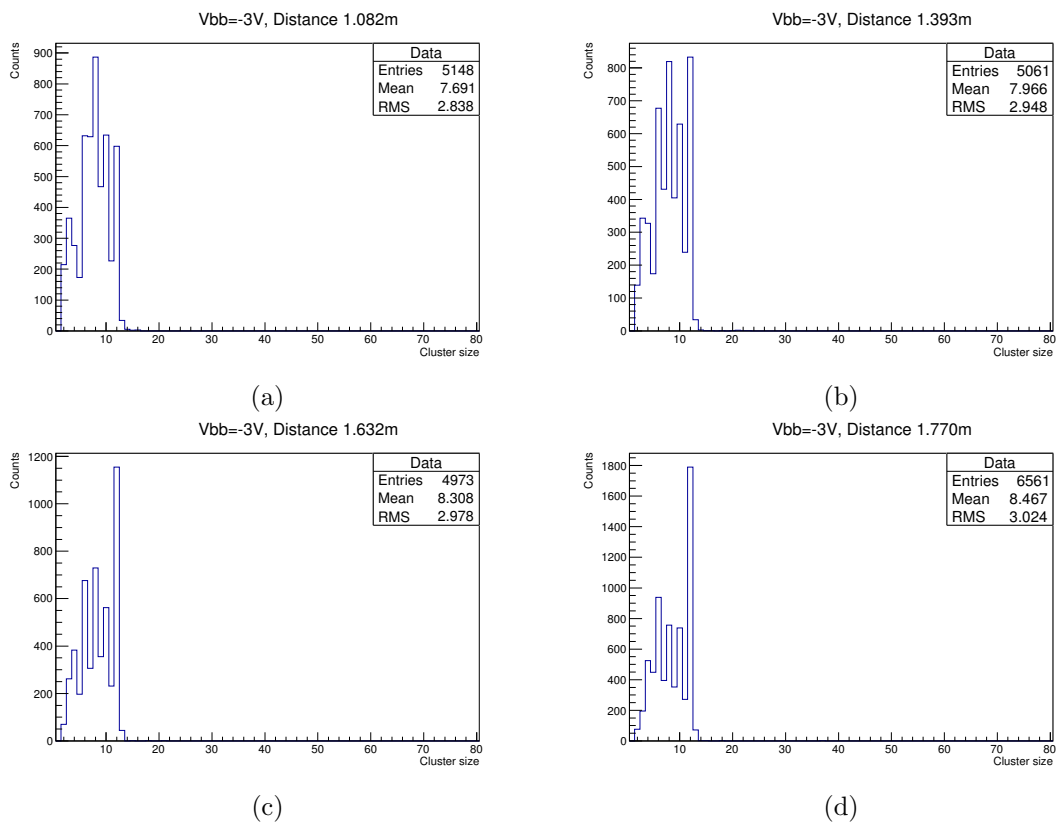
Figure 6.23: Measurements taken in region before Bragg peak, with a small rise in LET between measurements.

Fig 6.23a shows a fairly uniform cluster size, with a peak at 8 in cluster size. The LET of the protons is still constant for most of the protons. The small peak at 2 in cluster size is due to the background (see Fig 6.22). For the measurements 6.23b, 6.23c and 6.23d a preference of cluster sizes with even number of pixels firing is observed. This is the same which has been observed in previous experiments with MIP particles [36][38]. The peak is at 12 in cluster size for all measurements, even though the LET increases as the ALPIDE moves into the Bragg-peak. This is an indication that 12 in cluster size is the most preferable large size for the beam and ALPIDE settings used during the measurements.
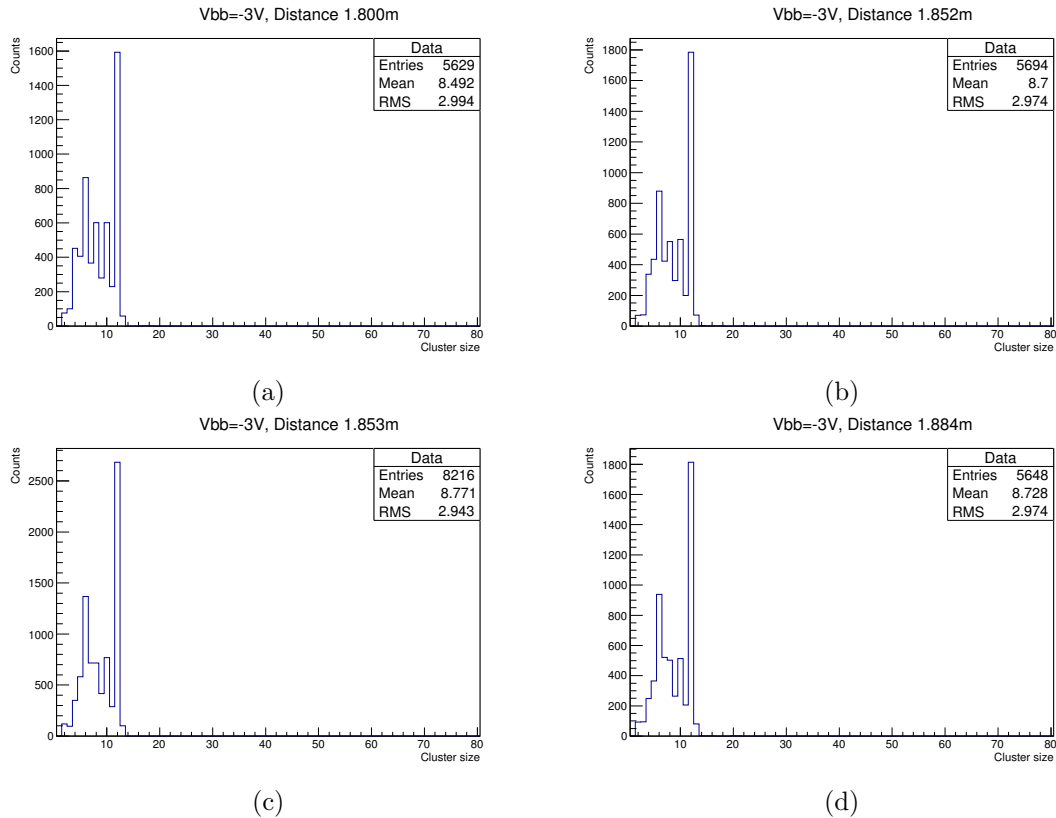
Figure 6.24: Average cluster sizes of four different measurements done in the region leading up to the maximum energy deposition of the traversing protons.

The preference in cluster size continuous to be that of an even value. The peak stays at 12 in cluster size when the ALPIDE is moved into the Bragg-peak for 6.24b, 6.24c and 6.24d. For 6.24c and 6.24d the peak around 6 in cluster size also starts to arise, while the cluster sizes in between 6 and 12 drop.
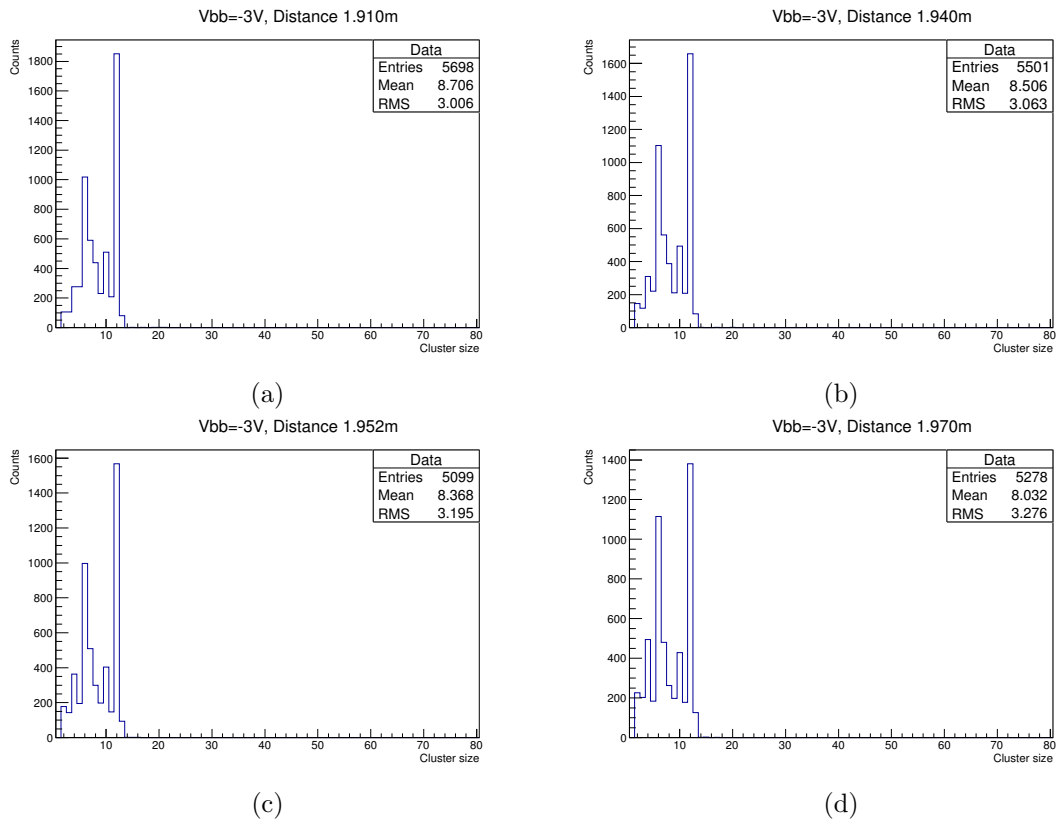
Figure 6.25: Average cluster sizes for four different measurements done in the region where the traversing protons have the maximum energy deposition.

The figures in 6.25 are at the fall off after the Bragg-peak. The most dominant cluster size is 12 and even cluster size is preferable. There is a growth in the cluster size 6 as the ALPIDE moves further away from the beam entry.
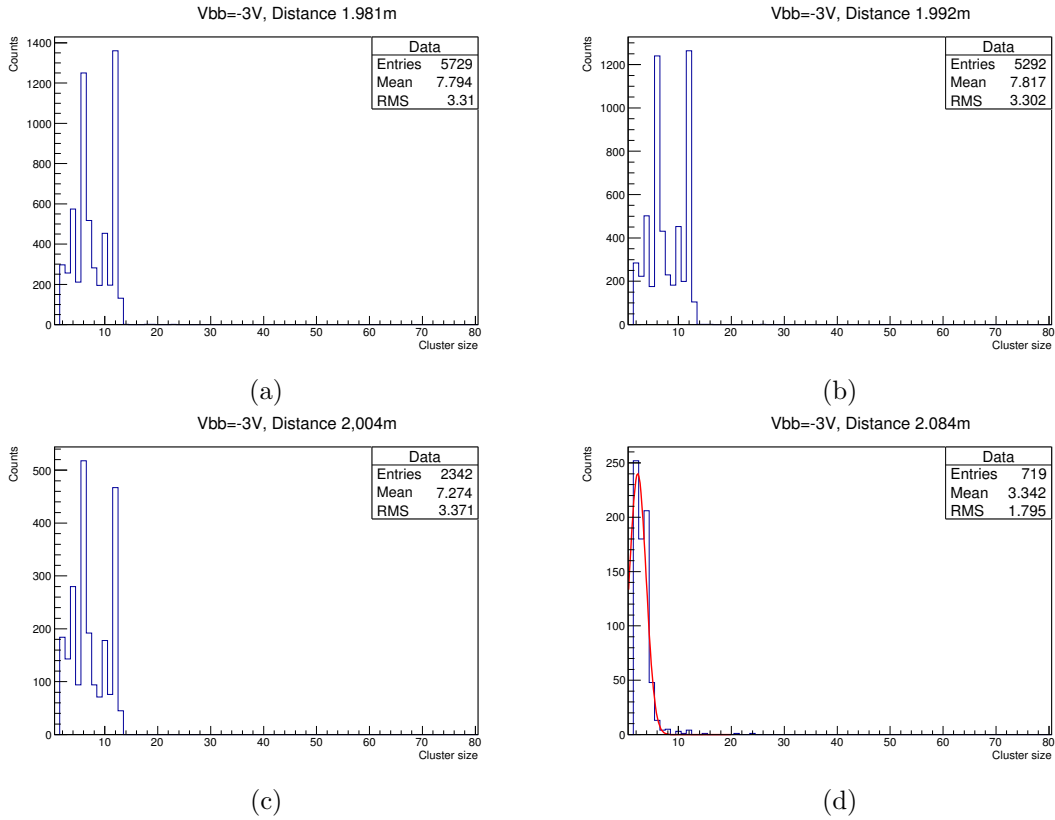
Figure 6.26: Average cluster sizes for four different measurements done in the region where the traversing protons have the maximum energy deposition.

The same characteristics can be seen for the figures 6.26a, 6.26b, and 6.26c as in 6.24 and 6.25. Fig 6.26d is at the very end of the Bragg curve and shows the background during the measurements.
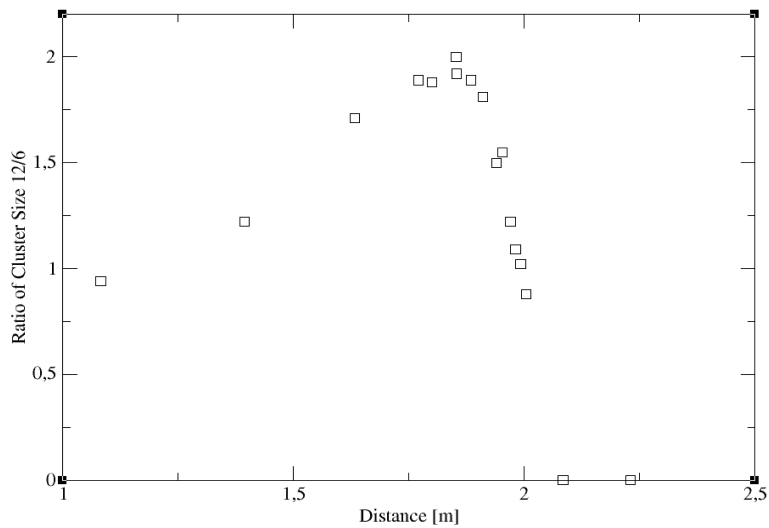
Figure 6.27: Ratio of Clusters with size 12 and 6 as a function of distance.

In Fig 6.27 the ratio between clusters with the size of 12 and 6 have been plotted. The shape of the curve is reminiscent of a Bragg-curve. The ALPIDE starts up close to the

beam, where the ratio is approximately 1. At this point the energy loss of the protons traversing the ALPIDE is fairly constant, so the difference in cluster size is down to the area of the depletion region. Given a ratio of 1 this indicates that the depletion region covers somewhere around 50% of the area of the pixel. As the ALPIDE moves further away from the beam entry the ratio goes up, since the LET of the different interactions increases. The proton fluence is still high in the beam, allowing for interactions where the proton deposits a lot of energy. This increase in ratio continuous as the ALPIDE moves into the Bragg-peak. After the Bragg-peak is reached, there is a fall off in the ratio. More of the traversing protons produces cluster of size 6. This is due to some of the protons not being able to penetrate through the entire ALPIDE. A variation in range between the protons is expected as the number of interactions they have had before they reach the ALPIDE differs. Some of the protons however, have avoided interactions along the way, and are still able to produce large clusters of size 12 if they hit outside the depletion region, and 6 if they hit it. Since the interactions of the protons as they traverse the air is governed by their respective cross-sections, it is expected that a percentage of them have not had to many interactions. As the ALPIDE moves away from the beam entry, it increases the probability for the protons to interact. After 2m the beam has reached is range and the ratio falls down to 0.
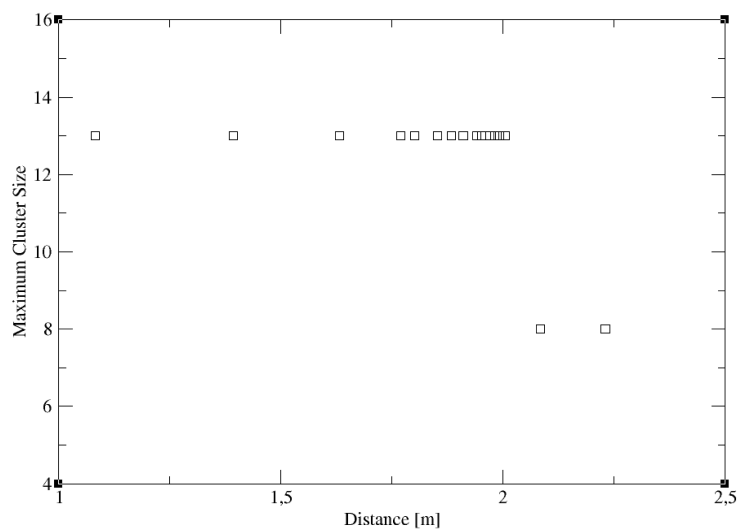
Figure 6.28: Maximum cluster size as a function of distance.

The maximum cluster size in each of the measurements can be observed in Fig 6.28. In the range of the beam the maximum cluster size is constant for all of the measurements, indicating that a beam with the properties of that which that was used, have a capped cluster size. Even though the ALPIDE is thin compared to the range of the beam, some of the protons are still able to deposit their maximum energy in the interaction with the ALPIDE. After the beam stops the background present in the hall produce some clusters of size 8.
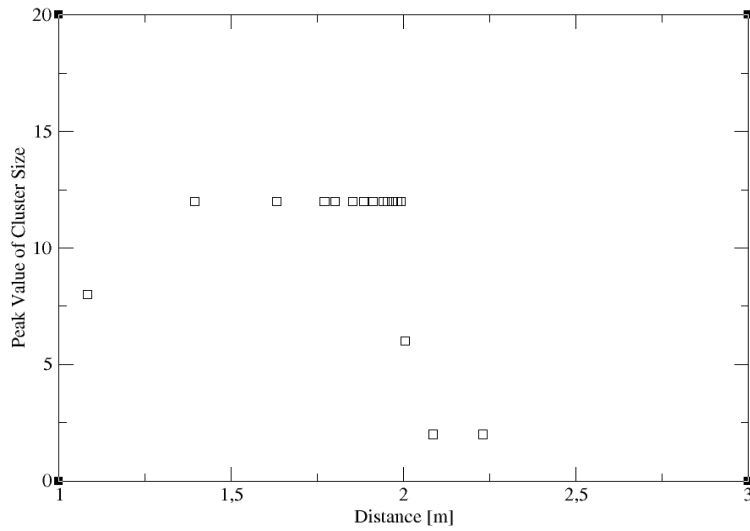
Figure 6.29: Most common cluster size as a function of distance.

The most common cluster size for a reverse bias voltage of -3 V can be observed in Fig 6.29. It starts out with a preferred cluster size of 8 before it saturates at 12 in cluster size. This is likely due to the geometry of the ALPIDE and the extension of the depletion region compared to the pixel area. It can be observed that clusters which has an even number of pixels firing, is the preferred size for a reverse bias voltage of -3V. The same was observed for 0V (see Fig 6.17).
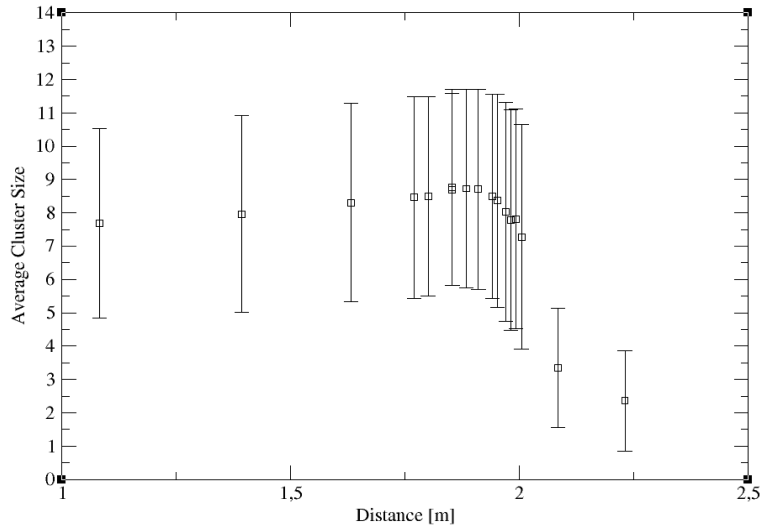
Figure 6.30: Average cluster size as a function of distance, with filtering of duplicate events.

The measurements of the energy deposition of protons at different distances (see Fig 6.30) are reminiscent of the Bragg-curve. Between 1 m and 1.75 m, the average cluster size is fairly constant, rising from 7.7 to 8.4. In the region between 1.75 m and 1.90 m the average cluster size grows up to 8.8 which corresponds to the top of the Bragg peak. The Bragg peak will be smeared out as the measurements were done individually. Given that the ionization potential is different in air and silicon, this will affect the range of the beam during the measurements. In the region after 1.90 m the average cluster size falls off before reaching an average cluster size of 2.2. This is the average cluster size created by the background radiation present in the experimental hall.
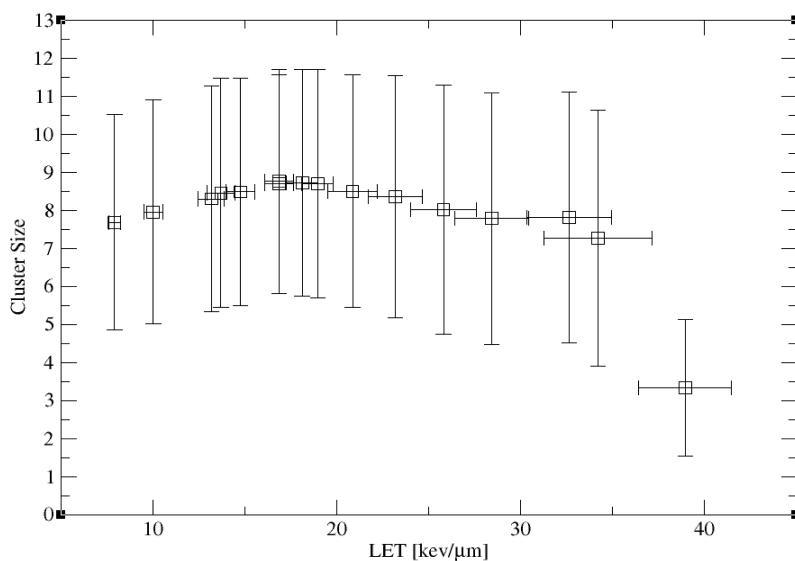
Figure 6.31: Average cluster size for measurement as a function of LET. Simulations of the LET from [39]

.

The simulations were performed in GATE with 1e9 particles. The physics list in use was: QGSP_BIC_EMY.

The relation between LET and cluster sizes can be observed in Fig 6.31. A linear relation is observed when the LET is in the range $5 - 18$ [keV/μm]. The rise is small due to small variations in the cluster size in this range (see Fig 6.30). Because of the reverse bias voltage being applied to the ALPIDE, the electric field inside is so high that the charges are not able to drift so that the clusters may increase in size. Thus the cluster size would not be a good indication of the LET if the ALPIDE is run with a reverse bias of -3V.

6.5   Simulations of beam parameters

Based on the measurements of the location of the Bragg peak, it is possible to estimate the energy of the beam during measurements. The simulations were performed in GATE. The tungsten scattering filter has been included in the simulations, and the results can be seen in Fig 6.32.
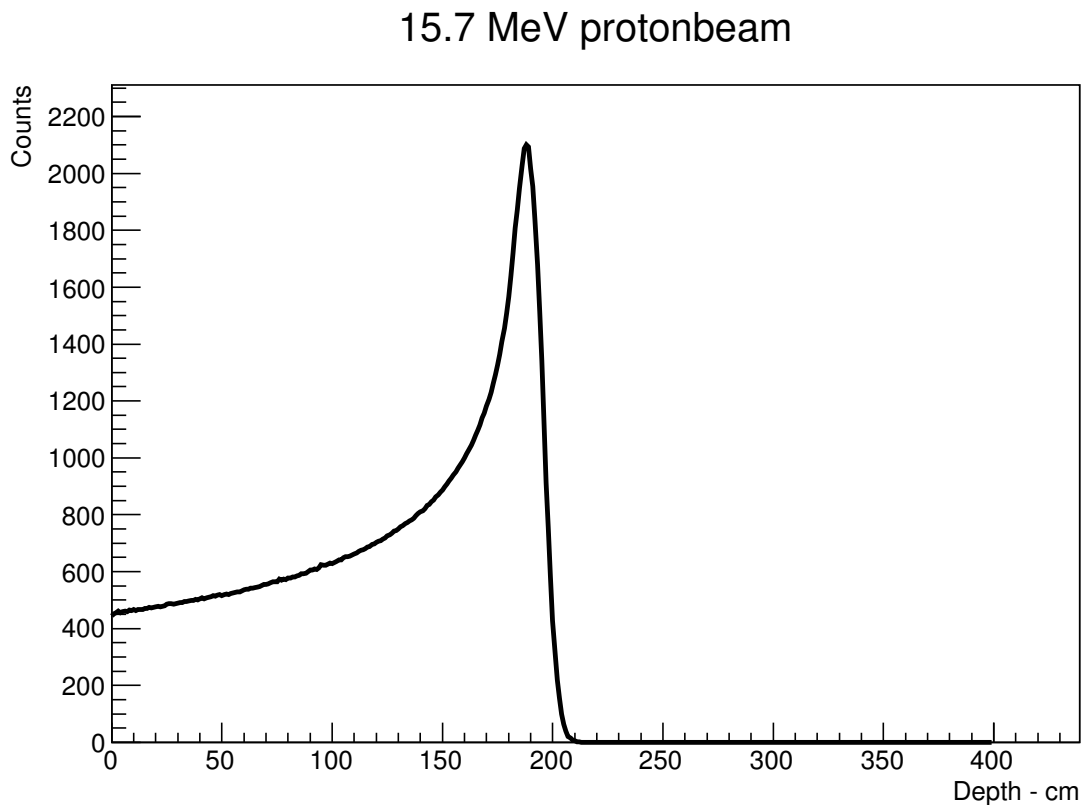
Figure 6.32: Simulated distance of 15.7 MeV proton beam

The range of the 15.7 MeV proton beam matches up with the estimated peak position of the Bragg peak for measurements performed with a reverse bias setting of 0 V and -3 V, as can be observed in section 6.4.4.

The following beam intensity was simulated for a beam energy of 15.7 MeV and the intensity was recorded at 188 cm distance from the beam entry.

Angular Distribution
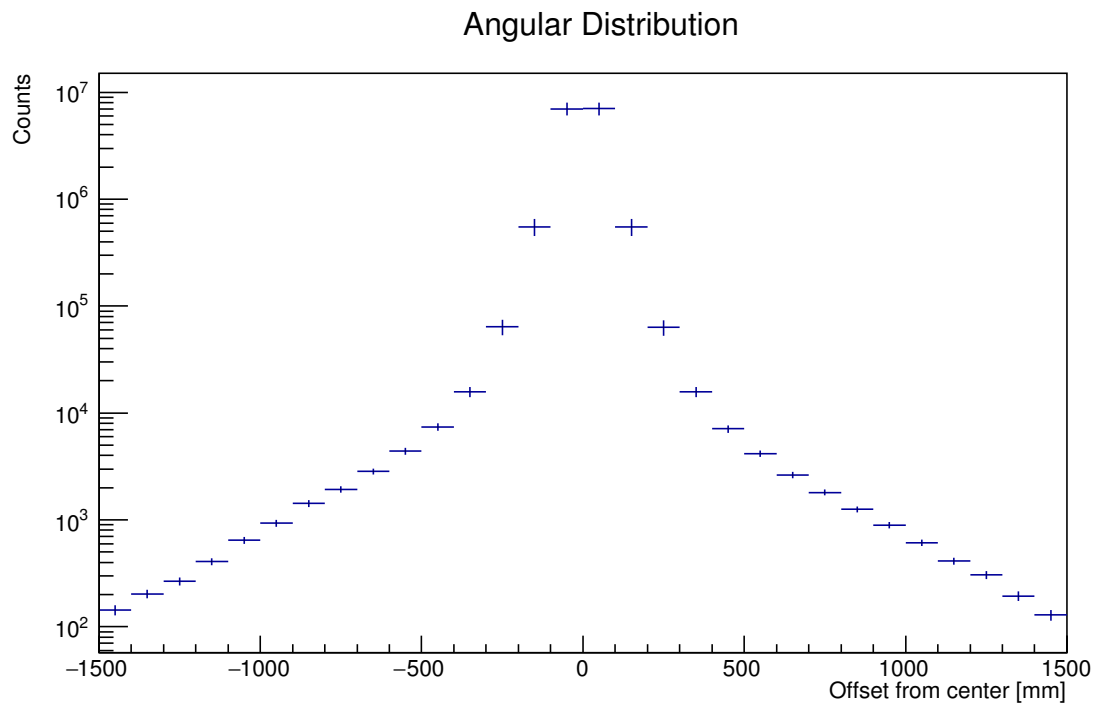
Figure 6.33: Simulation of angular distribution of proton beam at 188 cm distance with 10^7 particles

6.6 Flux measurements

For the flux measurements the distance from the beam entry was kept constant, while the offset from the center of the beam was increased, ranging from in the beam center out to an offset of 1500 mm. Calculations of the flux were done by taking the number of recorded hits in a measurement, removing the duplicate events and dividing by the runtime of that measurement and the area of the ALPIDE.
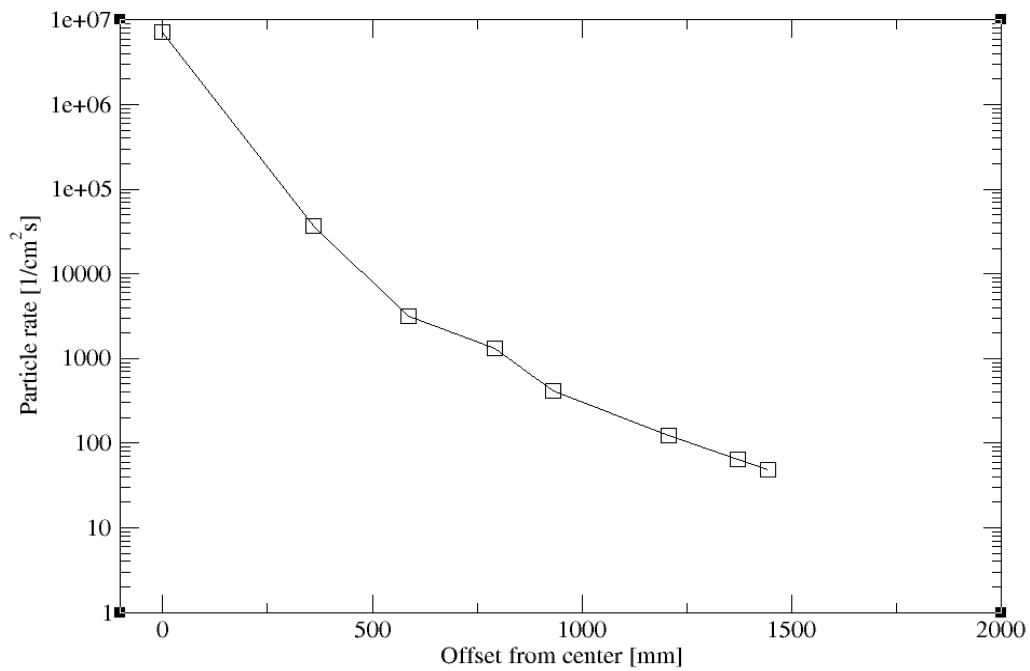
Figure 6.34: Measured particle flux with the ALPIDE as a function of offset from center of the beam
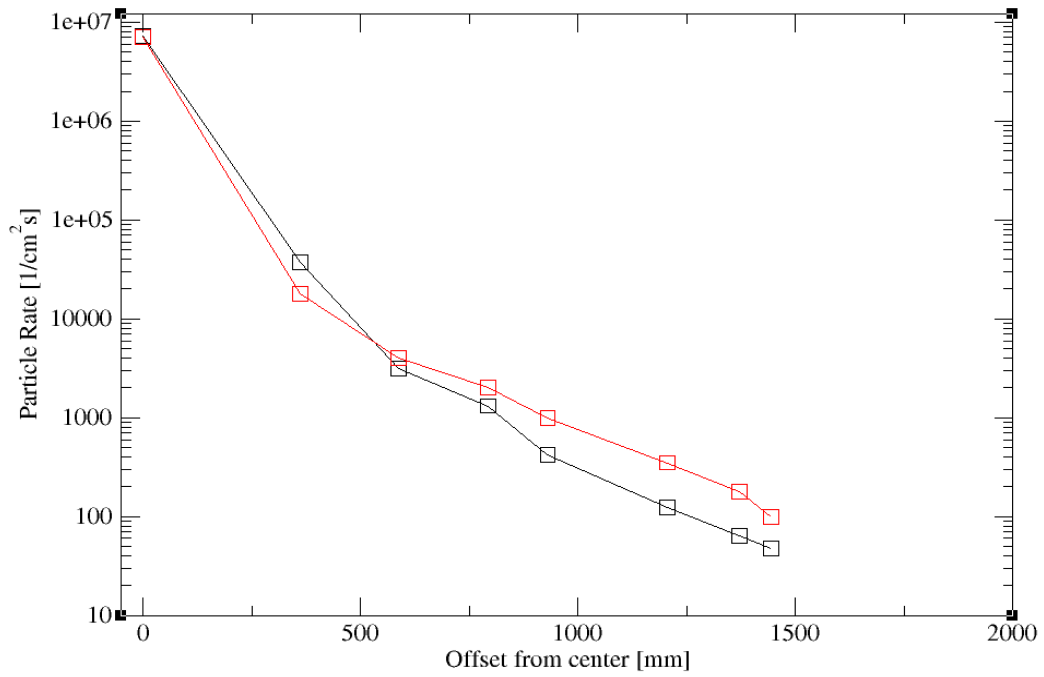
Figure 6.35: Comparison of simulated particle rate with measured particle rate. The red line represents the simulated values and the black line represents the measured values.

A comparison of the measured and simulated particle rate can be observed in Fig 6.35. The particle rate has an exponential fall off with the increasing angle, which is to be expected. Simulations and measured particle rate fits nicely at small angles, but there is a slight difference in particle rate at higher angles, where the measured particle rate sits lower than the simulated rate. This could be from fluctuation in the particle rate between measurements or that MEBs of the ALPIDE are not able to handle the high particle rate in the center of the beam, and thus the data points may be wrong at small angles.

Chapter 7

Discussion and conclusion

The main objective of this thesis has been to evaluate how well the ALPIDE detector performs the measuring of the energy loss of the traversing particles, in order to implement it in the pCT being developed at the University of Bergen. This was studied with radioactive sources and with a proton beam test.

The motivation to develop a pCT scanner by using only one detector is to have one system running the whole setup. For the ALPIDE to operate efficiently in the pCT it must have excellent tracking capabilities as well being able to define the energy loss of the particles while they traverse the patient. Thus the energy resolution must be good. These studies show that the ALPIDE has preferred cluster formations. The penetration depth through the layers as well as the cluster size and shape, is what determines the energy. For two energy depositions $\frac{dE_1}{dx} < \frac{dE_2}{dx}$ where dx is the depth of the epitaxial layer, from the same particle, it is not given that $\frac{dE_2}{dx}$ will create a larger cluster than $\frac{dE_1}{dx}$ since the trajectory of the particle may vary slightly between the layers, such that for $\frac{dE_2}{dx}$ the particle traverses the depletion, while $\frac{dE_1}{dx}$ slightly misses it. Thus it may prove difficult to determine the energy loss of an individual particle at the end of its range based on cluster size. This being said, for a larger sample of particles the ALPIDE has proven capable to distinguish between energy depositions at different distances. If the ALPIDE is placed in front of the patient it may identify particles before they penetrate the patient. The relation between cluster size and LET is linear at this distance, so it will also be able to provide dose verification. With the reverse bias set at 0V, the ALPIDE performed well, as can be seen in Fig 6.17. By setting the reverse bias at -3V the energy resolution went a bit down, but the expected Bragg-curve is still visible (see Fig 6.29). For the pCT it will be desirable to have a good energy resolution as well as good tracking. The bias voltage which is applied will effect both, and further studies are needed to optimize this relation.

The energy of a particle may also be found from the time-over threshold if the energy deposition is in a certain range. This is done by manipulating the V_{clip} setting for the ALPIDE. Based on the studies in section 5.3.4, this could work well for certain energy depositions of the particle in question. However, there will be a problem if the particle rate is high enough. Thus for the pCT, which has a high particle rate, this would be a problem. Another problem arises as the ALPIDE has a maximum limit for the V_{clip} to set in, this is set at 1.8V to protect the electronics. The protons, however, will produce a voltage larger than this. Based on this the V_{clip} should be set at the minimum value to shorten the signal as much as possible, and thus avoid multiple particles firing the same pixel simultaneously. The only requirement would be to ensure that the time-over threshold for that energy deposition allows for the charge to diffuse to the surrounding

pixels before the arrival of a new strobe signal.

The ALPIDE also shows promising signs in terms of beam monitoring of the flux. When it is in Inner Barrel Mode it is able to handle large amounts of data. If the time over threshold for the signal from the front-end is known for the particle used in the beam, then software may be developed for on sight analysis. This way the particle rate can be known.

Future outlook

Subsequent experiments with the ALPIDE detector for applications in pCT should take the following into consideration:

- The ALPIDE should be configured for heavier particles which will be used during pCT. This includes particles such as protons, alphas and carbons. The ALPIDE currently only has optimized setting for the detection of MIPs.

- Beam tests with the ALPIDE as a telescope should be performed to optimize the settings such that the ALPIDE may perform well as both a tracking detector and as measurement device for energy loss of the protons in the pCT.

- Beam test with therapeutic proton beam energies, and energies used in imaging would give insight into how the ALPIDE would perform under clinical conditions.

- For the ALPIDE to be used in a pCT scanner it is a requirement that the radiation hardness is sufficient to handle the particle rate. Studies of the performance of the ALPIDE after radiation should be performed to evaluate how long the ALPIDE can be used in a clinical situation before the performance drop to a level such that the chips needs to be changed.

Bibliography

[1] H. Lynnebakken. *Jubler for partikkelterapi* 2012. [Online]. Available at :http://www.mn.uio.no/fysikk/forskning/aktuelt/aktuelle-saker/2012/ jubler-for-partikkelterapi.html

[2] Norwegian Government *Etablering av protonsentre i Bergen og Oslo* 2017. [Online]. Available at: https://www.regjeringen.no/no/aktuelt/etablering-av-protonsentre-i-bergen-og-oslo/id2579970/

[3] F.M. Khan *Physics or Radiation Therapy* ,3rd ed. Philadelphia, PA: Lippincott Williams & Wilkins, 2003.

[4] W. R. Leo. *Techniques for Nuclear and Particle Physics Experiments, A How-to Approach.* Springer-Verlag, 1987

[5] C. Amsler et al. *Passage of Particles Through Matter* http://pdg.lbl.gov/2009/reviews/rpp2009-rev-passage-particles-matter.pdf 2010 [Online: accessed 22. May-2018.]

[6] E.B. Podgorsak. *Radiation Physics for Medical Physicists* Springer, 2009.

[7] C. Grupen and B. Shwartz. *Particle Detectors.* Cambridge University Press, 2008

[8] C. Leroy, and P.G. Ranciota. *Principles of radiation interaction in matter and detection, vol 2.* World Scientific, 2009.

[9] T.F. Thorsteinsen. *Kompendium i strålingsfysikk, Phys231.* Fysisk Institutt, Universitetet i Bergen, 1995.

[10] H. Paganetti. *Proton Beam Therapy* IOP Publishing Ltd, 2017.

[11] D. Groom and S. Klein. *Passage of particles through matter* The European Physical Journal C-Particles and Fields, vol 15. no. 1-4, pp. 163-173, 2000.

[12] T. Kanai, Y. Furusawa, K. Fukutsu, H. Itsukaichi, K. Eguchi-Kasai and H. Ohara. *Irradiation of Mixed Beam and Design of Spread-Out Bragg Peak for Heavy-Ion Radiotherapy.* Radiation Research 147,78-85. 1997.

[13] A.V. Solov'yov *Nanoscale Insights into Ion-Beam Cancer Therapy* Springer 2017.

[14] F. Sauli. *Interaction of photons and neutrons with matter. In Gaseous Radiation Detectors: Fundamentals and Applications* Cambridge University Press, 2014. doi:10.1017/CBO9781107337701.005

[15] ICRU Report. *Fundamental Quantities and Units for Ionizing Radiation (Revised)* Oxford University Press, 2011

[16] C. Bopp. *The Proton as a dosimetric and diagnostic probe.* Université de Strasbourg, 2014.

[17] P. Mayles, A. Nahum and J.C. Rosenwald. *Handbook of Radiotherapy Physics, Theory and Practice.* Taylor and Francis Group, 2007

[18] T. Beyer, D.W. Townsend, T. Brun, P.E. Kinahan, & al,e. *A combined PET/CT scanner for clinical oncology.* The Journal of Nuclear Medicine, 41(8), 1369-79. 2000 Retrieved from https://search.proquest.com/docview/219252987?accountid=8579

[19] W. A. Kalender. *Computed tomography: fundamentals, system technology, image quality, applications.* John Wiley & Sons, 2011.

[20] E.J. Hall *Intensity-Modulated Radiation Therapy, Protons, And the Risk of Second Cancers* Intt. J. Radiation Oncology Biol. Phys. Vol. 65. No.1 pp. 1-7. 2006.

[21] M. Jermann *Particle Therapy Statistics in 2014* International Journal of Particle Therapy, Vol.2, No.1,pp.50-54. 2015.

[22] S. Girdhani, R. Sachs and L. Hlatky. *Biological Effects of Proton Radiation: What we know and Don't Know.* Radiation Research Society, 2013.

[23] V.A. Bashkirov, R.P. Johnson, H.F.W. Sadrozinski and R.W. Schulte *Development of proton computed tomography detectors for applications in hadron therapy* Nuclear Instruments and Methods in Physics Research Section A: Accelerators, Spectrometers, Detectors and Associated Equipment , vol. 809, pp. 120–129, 2016.

[24] G. Polundniowski, N.M. Allison and P.M. Evans *Proton Radiography and tomography with applictaion to proton therapy* British Institute of Radiology, 2015.

[25] T. Li, Z. Liang, J.V. Singanallur, T.J. Satogata, D.C. Williams and R.W. Schulte *Reconstruction for proton computed tomography by tracing proton trajectories-A Monte Carlo study.* Medical physics. 2006;33(3):699-706.

[26] W. Pauli. *Über den Zusammenhang des Abschlusses der Elektronengruppen im Atom mit der Komplexstruktur der Spektren* Zeitschrift für Physik, 1925.

[27] G.F.Knoll. *Radiation Detection and Measurement* John Wiley & Sons Inc. 3rd, edition 2000

[28] L. Rossi, P. Fischer, T. Rohe and N. Wermes *Pixel Detectors: From Fundamentals to Applications* Springer, 2005.

[29] L. Musa. *Upgrade of the ALICE Inner Tracking System.* ALICE ITS upgrade, 2015.

[30] L. Maczewski *Measurements and simulation of MAPS (monolithic active pixel sensors) response to charged particles - a study towards a vertex detector at the ILC* Warsaw University, 2010. https://arxiv.org/pdf/1005.3710.pdf

[31] The ALICE Collaboration *The ALICE experiment at CERN LHC* Journal of instrumentation, vol 3 no. 08, 2008.

[32] R. Lemmon *The ALICE Inner Tracking System Upgrade* Nuclear Physics A, vol. 904-905, 2013.

[33] ALICE ITS ALPIDE development team *ALPIDE Operations Manual* Version 0.3, July 2016.

[34] ALICE ITS Upgrade Team *The ALICE ITS Upgrade: Readout Electronics-WP10* CERN, Tech. Rep., 2016.

[35] D. Kim et al. *Front end optimization for the monolithic active pixel sensor of the*

ALICE Inner Tracking System upgrade Topical Workshop on Electronics for Particle Physics Septenber 28-October 2. 2015.

[36] Mónika Varga-Köfaragó *Anomalous Broadening of Jet-Peak Shapes in Pb-Pb Collisions and Characterization of Monolithic Active Pixel Sensors for the ALICE Inner Tracking System Upgrade.* Utrecht University, 2018.

[37] E.Belau, R. Klanner, G. Lutz, E. Neugebauer, HJ. Seebrunner, A. Wylie, T. Böhringer, L- Hubbeling, P. Weilhammer, J. Kemmer, U. Kötz and M. Riebesell. *Charge Collection in Silicon Strip Detectors* Nuclear Instruments and Methods 214, pp. 253-260. 1983

[38] S. Kushpil *Characterization of the ALPIDE monolithic active pixel sensor for the upgrade of the ALICE Inner Tracking System (ITS) using the PS facility at CERN* IEEE Nuclear Science Symposium and Medical Imaging Conference, 2017.

[39] A. T. Samnøy *Personal conversation*

Appendix A

Acronyms

ALICE A Large Ion Collider Experiment

ALPIDE ALice PIxel DEtector

CERN Conseil Europeen pour la Recherche Nucleaire

CFRT ConFormal RadioTherapy

CMOS Complementary Metal-Oxide-Semiconductor

CT Computed Tomography

DAC Digital Analog Converter

DAQ Data AcQuisition

DNA DeoxyriboNucleic Acid

DTC Digital Tracking Calorimeter

IMRT Image Modulated RadioTherapy

ITS Inner Tracking System

LET Linear Energy Transfer

LHC Large Hadron Collider

MAPS Monolithic active pixel sensor

MEB Multi Event Buffer

MIP Minimum Ionizing Particle

MRI Magnetic Resonance Imaging

MV Mega Volt

OCL Oslo Cyclotron Lab

pCT Proton Computed Tomography

PET Positron Emission Tomography

RBE Relative Biological Effect

RMS Root Mean Squared

ROI Region Of Interest

RRU Regional Readout Unit

SOBP Spread Out Bragg Peak

TOT Time Over Threshold

TRU Top Readout Unit

Appendix B

OCL testing

For the OCL test beam experiment, a shielding of the ALPIDE and electronics were necessary. Since the experiment were to be conducted with a low energy proton beam, only a thin shielding was a requirement. The material chosen for shielding were aluminum. According to the PSTAR database this has a range of 0.3862 [g/cm^2]. Given the density of aluminum being 2.70 [g/cm^3], the thickness of the shielding was calculated to be 0.14 cm. From this the thickness of the shielding plate was chosen to be 0.2 cm. The design schematic can be seen in Fig B.1. The drawing is not to scale. While the finished design can be seen in Fig B.2.
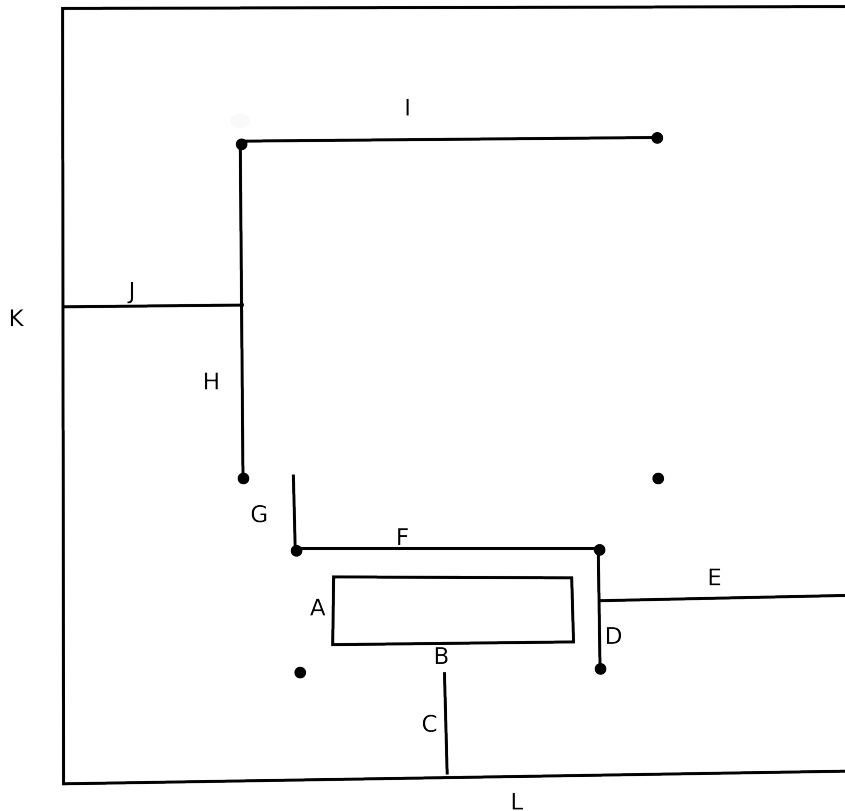

Figure B.1: The points represents the holes where the ALPIDE and DAQ board where attached. The letters represents the distances of the line it is attached to. All distances are represented in cm. A: 1.5, B: 3, C: 10.1, D: 6, E:4, F:6, G: 2.7, H: 10.1, I: 10.1, J:2.2, K:37, L: 14.

Figure B.2: The finished design of the shielding device used at OCL.

Settings for the different measurements are listed below.

	Bragg curve measurements with fixed reverse bias, -3 V	
Reverse bias voltage	Distance [m]	Angle in degrees
-3V	2.230	26.06
-3V	2.084	26.62
-3V	2.004	26.56
-3V	1.992	26.70
-3V	1.981	27.05
-3V	1.970	27.31
-3V	1.952	27.09
-3V	1.940	27.54
-3V	1.910	27.94
-3V	1.884	28.43
-3V	1.853	27.81
-3V	1.852	28.79
-3V	1.800	29.08
-3V	1.770	29.48
-3V	1.632	28.95
-3V	1.393	32.87
-3V	1.082	33.68

	Bragg curve measurements with fixed reverse bias, 0 V	
Reverse bias voltage	Distance [m]	Angle in degrees
0V	1.991	19.3
0V	1.970	19.9
0V	1.954	19.9
0V	1.945	20.2
0V	1.924	20.2
0V	1.900	20.7
0V	1.888	20.8
0V	1.872	21.1
0V	1.852	21.4
0V	1.809	21.4
0V	1.717	25
0V	1.483	28.4
0V	1.170	30.6
0V	0.667	20.6
0V	0.527	26.6

	Flux measurements	
Reverse bias voltage	Distance [m]	Angle in degrees
-3V	1.518	0
-3V	1.704	12.2
-3V	1.707	20.2
-3V	1.666	27.8
-3V	1.730	33.2
-3V	1.666	45.2
-3V	1.637	53.8
-3V	1.650	58.1